LA-12979-MS

Finite Element Analysis of the I-40 Bridge Over the Rio Grande

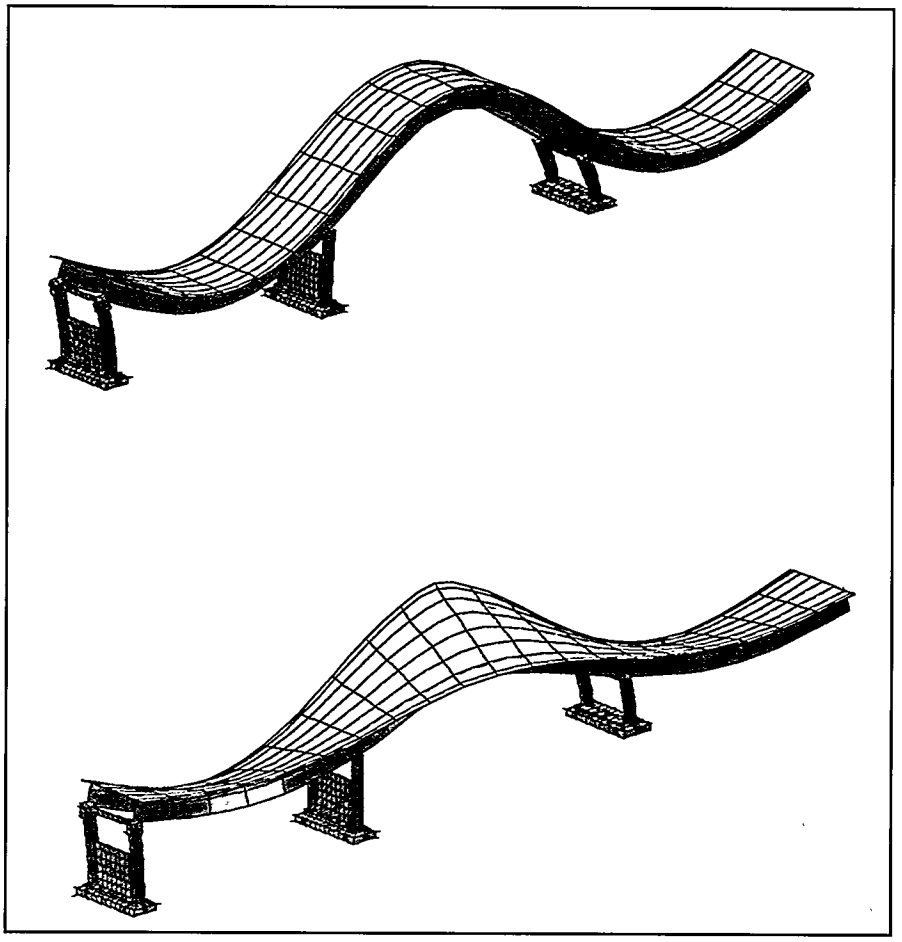

Los Alamos
NATIONAL LABORATORY

Los Alamos National Laboratory is operated by the University of California for the United States Department of Energy under contract W-7405-ENG-36.

Edited by Ann Mauzy, Group CIC-1
Photocomposition by Joyce A. Martinez, Group CIC-1

Cover photo: *The first bending modes calculated for the eastern three spans of the I-40 Bridge. The top figure corresponds to a numerical simulation of the undamaged bridge, and the bottom figure corresponds to a numerical simulation of the final stage of damage.*

LA-12979-MS

UC-000
Issued: January 1996

Finite Element Analysis of the I-40 Bridge Over the Rio Grande

C. R. Farrar
T. A. Duffey
P. A. Goldman
D. V. Jauregui
J. S. Vigil

Los Alamos
NATIONAL LABORATORY
Los Alamos, New Mexico 87545

TABLE OF CONTENTS

LIST OF FIGURES

LIST OF TABLES

FINITE ELEMENT ANALYSIS OF THE I-40 BRIDGE OVER THE RIO GRANDE

by

C. R. Farrar, T. A. Duffey, P. A. Goldman, D. V. Jauregui, and J. S. Vigil

ABSTRACT

In the 1960s and 1970s numerous bridges were built in the U.S. with a design similar to those on Interstate 40 (I-40) over the Rio Grande in Albuquerque, New Mexico. These bridges were built without structural redundancy and typically have only two plate girders carrying the entire dead and live loads. Failure of either girder is assumed to produce catastrophic failure of the bridge; hence, these bridges are referred to as fracture-critical bridges. The Federal Highway Administration (FHWA) and the National Science Foundation (NSF) have provided funds to New Mexico State University (NMSU) through the New Mexico State Highway and Transportation Department (NMSH&TD) and The Alliance For Transportation Research (ATR) for evaluation and testing of the existing fracture-critical bridges over the Rio Grande.

Because the I-40 Bridges over the Rio Grande were to be razed during the summer of 1993, the investigators were able to introduce damage into the structure in order to test various damage identification methods and to observe the changes in load paths through the structure caused by the cracking. To support this research effort, NMSU contracted Los Alamos National Laboratory (LANL) to perform experimental modal analyses, and to develop experimentally verified numerical models of the bridge. A previous report (LA-12767-MS) summarizes the results of the experimental modal analyses. This report summarizes the numerical analyses of the bridges and compares the results of these analyses to the experimental results.

Finite element models were developed with varying levels of sophistication. The most refined model, which discretized the individual longitudinal and vertical stiffeners on the plate girders, used a mesh with approximately 35,160 degrees of freedom (DOF) to model the structure exclusive of the piers. Additional elements were subsequently added to model the concrete piers. A second model of intermediate refinement that neglected the stiffeners and modeled the plate girders with fewer elements used 7032 DOF to model the structure above the piers. Mode shapes and resonant frequencies identified with these models were identical. After adjusting the kinematic constraints that tie the bottom flange of the plate girder to the piers, the results from the 7032 DOF model were shown to be in agreement with the dynamic properties measured on the bridge (less than 5% error in resonant frequencies). Systematic model updating procedures were not employed when attempting to correlate the finite element results with experimental results.

These numerical models simulate composite action between the concrete deck and the supporting steel girders. The agreement with measured data indicates that the bridge was exhibiting composite action even though shear studs were not present. The 7032 DOF

model also predicted the measured changes in the dynamic properties that resulted from the damage. To obtain this correspondence with measured data, only the geometry of the model was changed to reflect the damage. The implication is that from a structural dynamics viewpoint the actual damage did not introduce a discernible nonlinearity into the structure.

The major portion of this study focused on the development of a 1687 DOF model that uses individual beam elements to model the entire bridge cross section. This model required the development of a method to determine the torsional properties (torsional constant, warping constant, sectorial moment, shear center, and mass moment of inertia) of an open, thin-walled cross section of two materials. Because the finite element code used does not allow the polar area moment of inertia to be specified explicitly, a method of calculating an equivalent mass density and cross-sectional area had to be developed to accurately model both the flexural response and the torsional response. The dynamic mode shapes predicted by this simple model were consistent with those measured on the bridge, but the resonant frequencies showed some error. Because of the limited numbers of DOF, this type of model can be exercised extensively on a PC (typical of the computing environment at most smaller consulting engineering firms) to study the response of the bridge to time-varying inputs such as seismic or wind loading.

Now that the 7032 DOF model has been benchmarked against experimental data in both the undamaged and damaged condition, it will be used to compare different damage identification algorithms that have been reported in the technical literature. The results of this comparison will be summarized in a subsequent report.

I. INTRODUCTION

In the 1960s and 1970s numerous bridges were built in the U.S. with a design similar to those on Interstate 40 (I-40) over the Rio Grande in Albuquerque, New Mexico, Fig. 1. These bridges were built without structural redundancy and typically have only two plate girders carrying the entire dead and live loads. Failure of either girder is assumed to produce catastrophic failure of the bridge. Because of this lack of redundancy, the bridges, which have been found to exhibit fatigue cracking from out-of-plane bending, are referred to as fracture-critical bridges. The Federal Highway Administration (FHWA) and the National Science Foundation (NSF) have provided funds to New Mexico State University (NMSU) through the New Mexico State Highway and Transportation Department (NMSH&TD) and The Alliance For Transportation Research (ATR) for evaluation and testing of the existing fracture-critical bridges over the Rio Grande. The project is intended to develop and field test new nondestructive testing technology and to create a detailed bridge management data base for this class of bridges. The NSF is providing funds to investigate the seismic capacity of bridges such as these that were built before the adoption of modern seismic design standards.

1. I-40 Bridges over the Rio Grande in Albuquerque, New Mexico.

Because the bridges over the Rio Grande were to be razed during the summer of 1993, the investigators were able to introduce simulated fatigue cracks, similar to those observed in the field, into the structure in order to test various damage-identification methods and to observe the changes in load paths through the structure caused by the cracking. To support this research effort, NMSU contracted Los Alamos National Laboratory (LANL) to perform experimental modal analyses, and to develop experimentally verified numerical models of the bridge. Scientists from the LANL's Condensed Matter and Thermal Physics Group (MST-10) applied state-of-the-art sensors and data acquisition software for the modal tests. Engineers from the LANL's Engineering Analysis Group (ESA-EA) conducted ambient and forced vibration tests to verify detailed and simplified finite element models of the bridge. Forced vibration testing was done in conjunction with engineers from Sandia National Laboratory (SNL) who provided and operated a hydraulic shaker.

This report summarizes the numerical models of the bridge and compares results obtained with these models to the measured dynamic properties of the bridge. The numerical models were developed for three purposes. First, they were used to study instrumentation options for the experimental portion of this study. Second, a study was made to see if a very simple beam element model could be developed that would accurately predict the global dynamic response of the bridge. Such models will be very useful for designers because they provide a computational tool with which to examine the dynamic response of the bridges to a wide variety of load conditions that can be analyzed efficiently in a PC computing environment. Finally, the benchmarked finite element models can be used to make an extensive comparison of various damage-identification algorithms.

II. DESCRIPTION OF THE I-40 BRIDGES

The existing I-40 Bridge over the Rio Grande consists of twin spans (there are separate bridges for each traffic direction) made up of a concrete deck supported by two welded-steel plate girders and three steel stringers. Although plans for the bridge show studs welded to the flanges of the outer stringers, studs were not found when the concrete deck was removed. Loads from the stringers are transferred to the plate girders by floor beams located at 20-ft intervals. Cross-bracing is provided between the floor beams. Figure 2 shows an elevation view of the portion of the bridge that was tested. The cross-section geometry of each bridge is shown in Fig. 3, and Fig. 4 shows the actual substructure of the bridge. It should be noted that the actual bridges have concrete crash barriers on either side of the concrete slab. These crash barriers were not shown in the original drawings for the bridge.

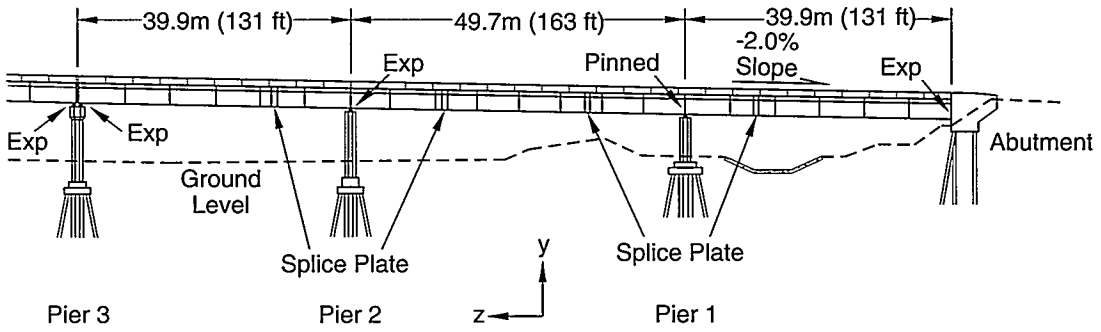

Fig. 2. Elevation view of the portion of the eastbound bridge that was tested.

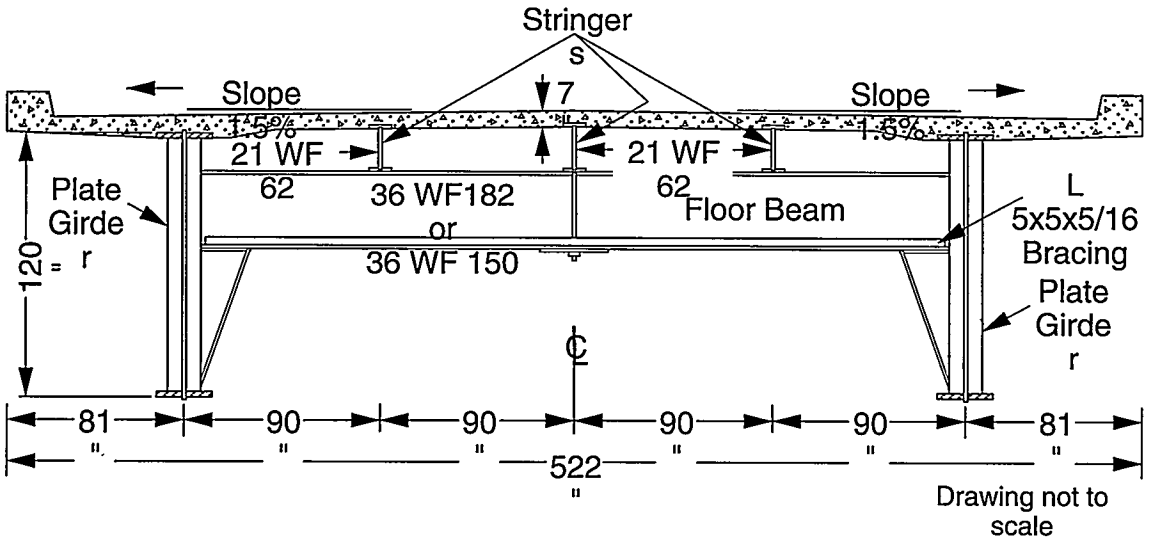

Fig. 3. Typical cross-section geometry of the bridge.

Fig. 4. Bridge substructure.

All subsequent discussions of the bridge will refer to the bridge carrying eastbound traffic, particularly the three eastern spans, which were the only ones tested.

III. SUMMARY OF EXPERIMENTAL RESULTS

This section provides a brief summary of the experimental results that were obtained from both ambient and forced vibration tests performed on the I-40 Bridge. Forced vibration tests were performed when the bridge was in an undamaged state and after each of four incremental levels of damage had been introduced. A detailed summary of these tests and the results that were obtained are given by Farrar, et al., (1994).

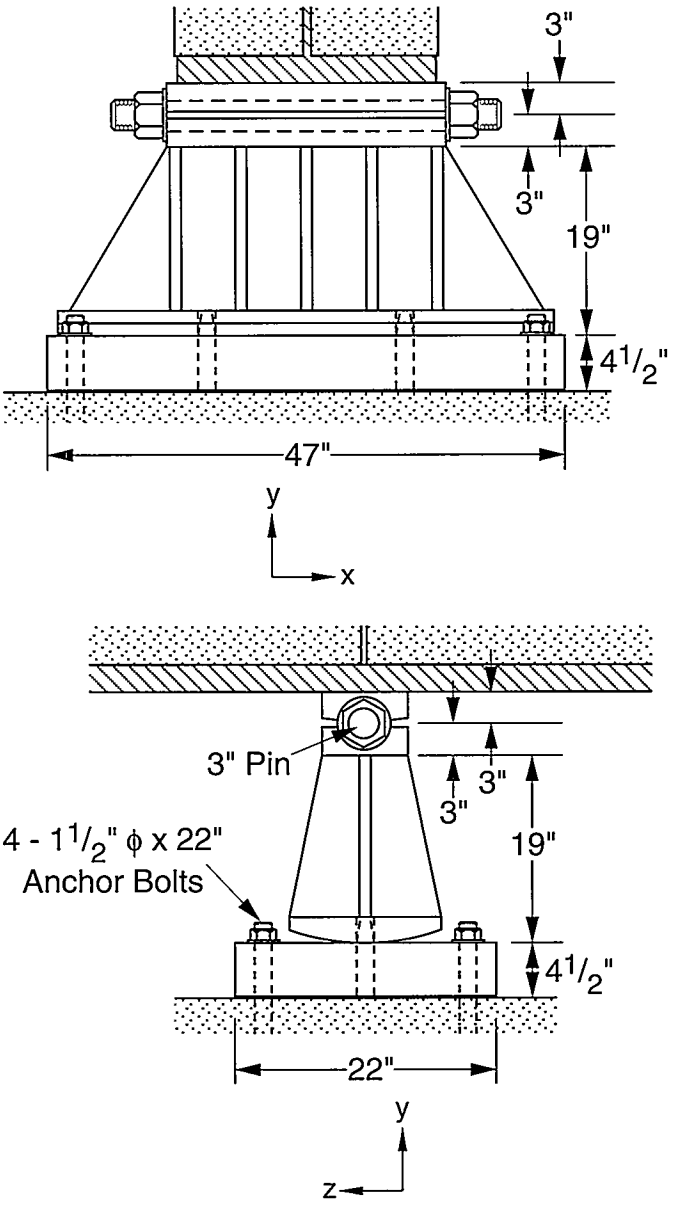

Fig. 5. Connection detail found at the abutment and Pier 3 that allows longitudinal displacement.

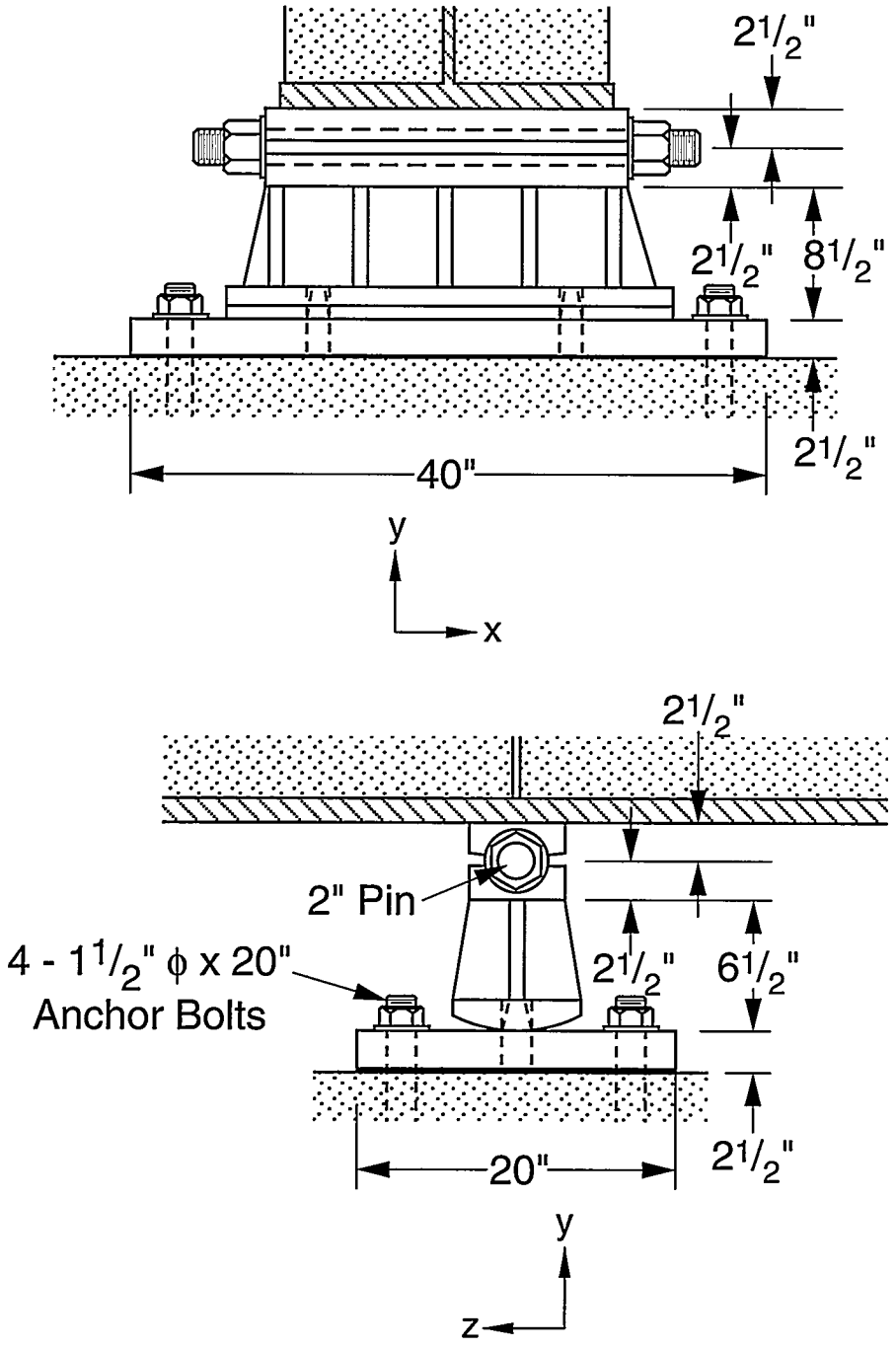

Fig. 6. Connection detail found at Pier 2 that allows longitudinal displacement.

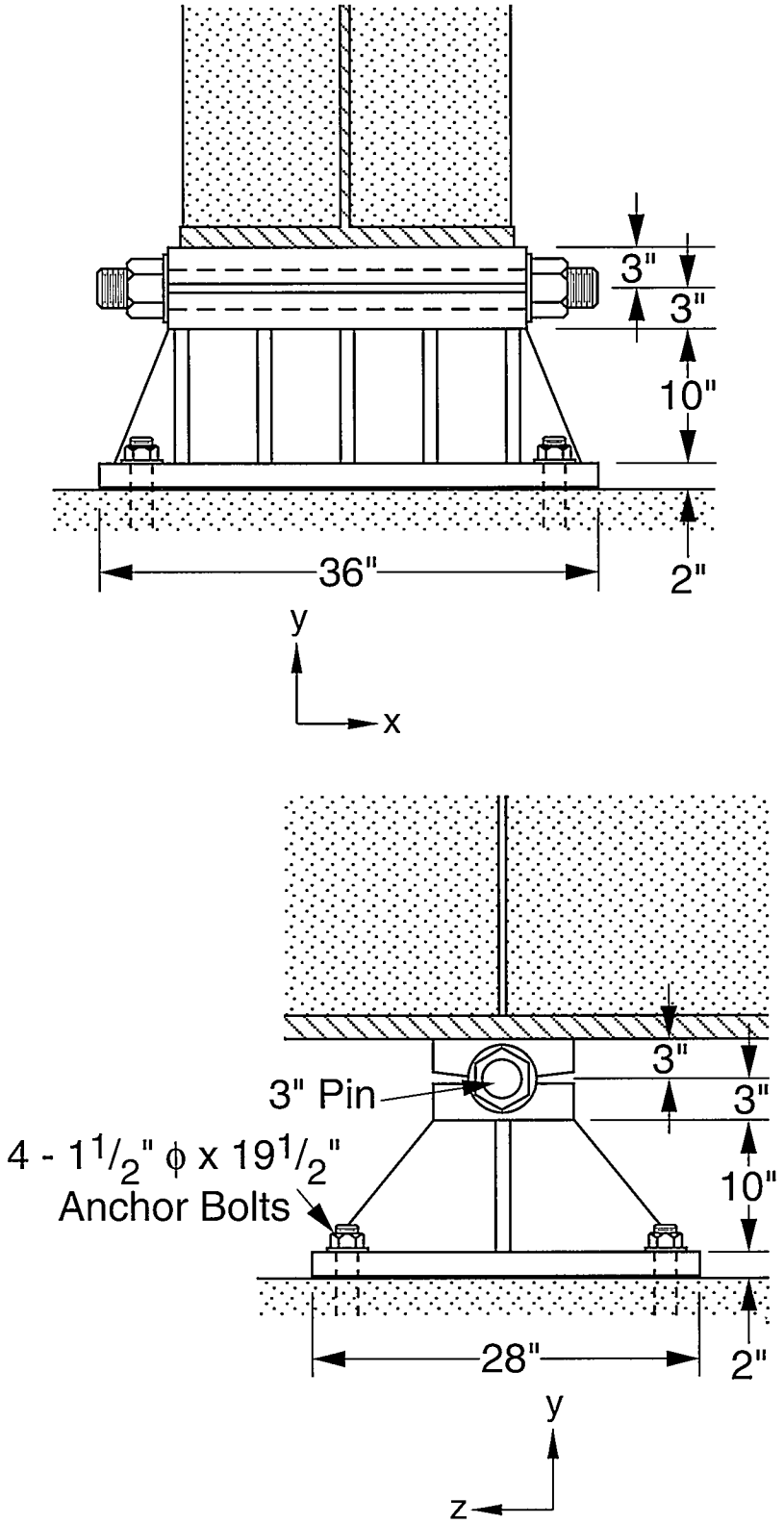

Fig. 7. Connection detail found at Pier 1 that constrains longitudinal displacement.

III. A. Ambient Vibration Testing

Following the preliminary measurements made in March 1993, ambient (traffic) vibration tests were conducted on June 28 and 29, July 7 through 9, and August 31, 1993. These tests were intended to identify the structure's resonant frequencies, modal damping, and the corresponding mode shapes. Wind was light during all ambient vibration tests and was not considered a significant input source.

Traffic had been funneled onto the two northern lanes during these tests. Significantly different traffic flow could be observed at various times when data were being acquired. During morning and afternoon rush hours the traffic would slow down considerably thus producing lower-level excitations in the bridge. At midday the trucks crossing the bridge at high speeds would cause high-level excitations that would often over range some of the data acquisition channels. The ambient vibration test conducted on August 31 was done just before the forced vibration tests when all traffic had been removed from the eastbound bridge. For this test the ambient vibration source was provided by the traffic on the adjacent new eastbound bridge and the existing westbound bridge. This vibration was transmitted through the ground to the piers and abutment. During all ambient tests, no attempt was made to characterize the input to the bridge.

The data acquisition system used in these tests, Fig. 8, consisted of a computer workstation which controlled 29 input modules and a signal processing module. The workstation was also the platform for a commercial data-acquisition/signal-analysis/modal-analysis software package. The input modules provided power to the accelerometers and performed analog-to-digital conversion of the accelerometer voltage-time histories. The signal-processing module performed the needed fast Fourier transform calculations. A 3500-watt AC generator was used to power this system in the field. Integrated-circuit, piezoelectric accelerometers were used for the vibration measurements. Twenty-six one-inch square aluminum mounting blocks were dental-cemented to the inside web of the plate girder at mid-height and at the axial locations shown in Fig. 9. Within a span the three blocks were equally spaced in the axial direction. Accelerometers were mounted on the blocks with a 10-32 stud, in the global Y direction as shown in Fig. 9. These accelerometers had a nominal sensitivity of 1 V/g, a specified frequency range of 1–2000 Hz, and an amplitude range of 4 g's. Two conductor, PVC-jacketed 20-gauge cables ranging from 70 ft to 291 ft connected the accelerometers to the input modules. The cables were supported by the catwalks located along each plate girder, tied off, and dropped down under the bridge to the van that housed the data acquisition system.

To circumvent the drawbacks of the methods used in previous ambient vibration tests reported by Abdel-Ghaffar and Housner (1978), an ambient vibration system identification method developed at SNL was applied to the measured response data obtained on the I-40 Bridge. James, Carne, and Lauffer (1993), have shown that for an input, which is not measured but assumed to be white noise, the cross-correlation function between two response measurements (the inverse Fourier transform of the cross-power spectra (CPS)) is the sum of decaying sinusoids, and these decaying sinusoids have the same damped

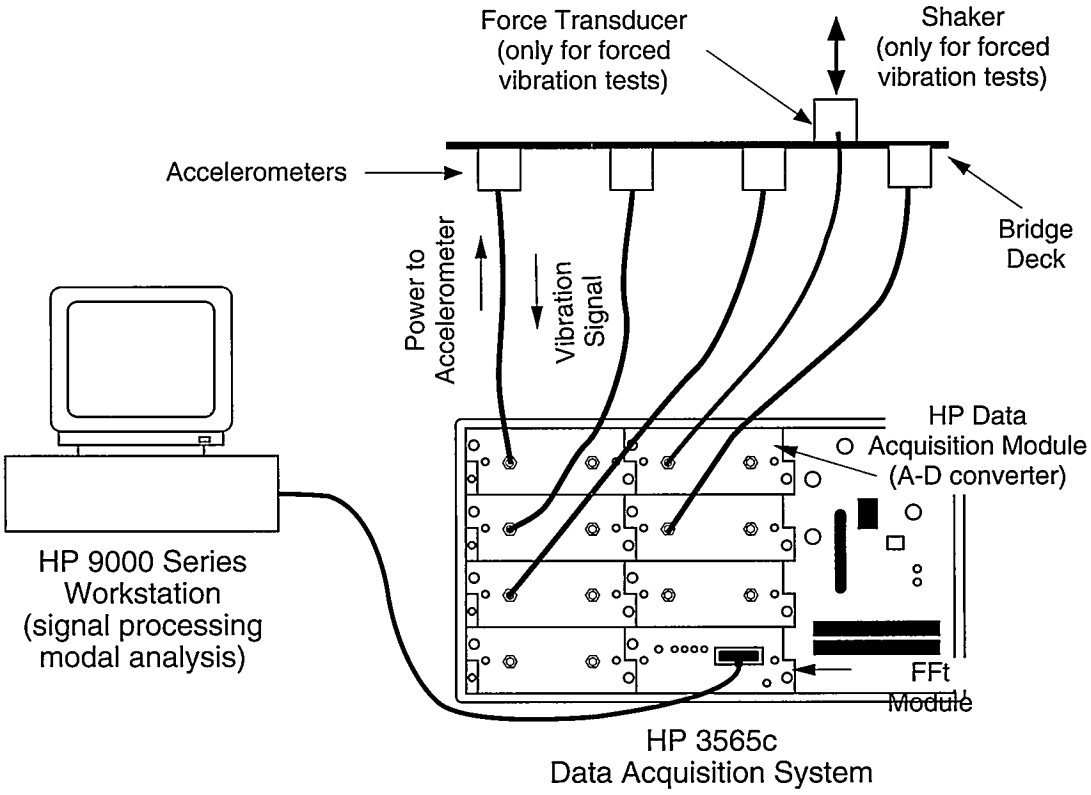

Fig. 8. Data acquisition system.

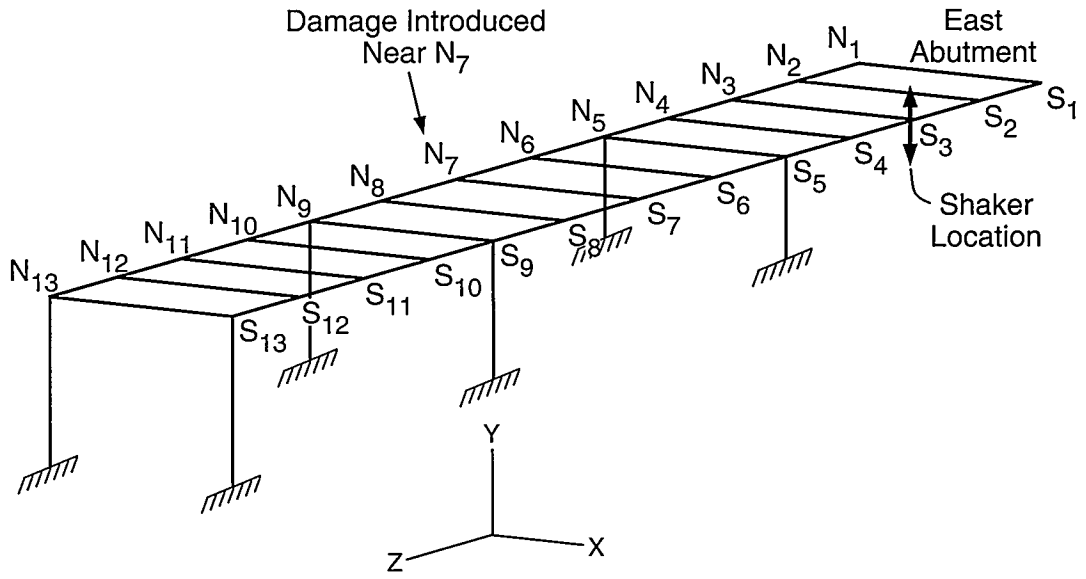

Fig. 9. Accelerometer locations.

resonant frequencies and damping ratios as the modes of the system. Therefore, the cross-correlation functions will have the same form as the system's impulse response function, and, hence, time-domain, curve-fitting algorithms such as the polyreference method (Vold and Rocklin, 1982) or complex exponential method (Ewins, 1985) can be applied to these functions to obtain the resonant frequencies and modal damping exhibited by the structure. These curve-fitting methods have the ability to identify closely spaced modes and, in general, provide a more accurate method for estimating damping than the half-power bandwidth method. Mode shapes are determined from magnitudes and phases in the CPS at the identified resonant frequencies relative to a specified reference channel.

Sampling parameters were specified that calculated the CPS from 64-s, 32-s, or 16-s time windows discretized with 1024 samples. Therefore, the CPS were calculated for frequency ranges of 0-–6.25 Hz, 0–12.5 Hz, and 0–25 Hz. Typically, 100 averages were used to calculate the 0–6.25 Hz CPS, 30 averages were used to calculate the 0–12.5 Hz CPS, and 75 averages were used to calculate the 0–25 Hz CPS. Frequency resolutions of 0.015625 Hz, 0.03125 Hz, and 0.0625 Hz were obtained for the 0–6.25 Hz CPS, the 0–12.5 Hz CPS, and the 0–25 Hz CPS, respectively. Hanning windows were applied to the time signals to minimize leakage, and AC coupling was specified to minimize DC offsets.

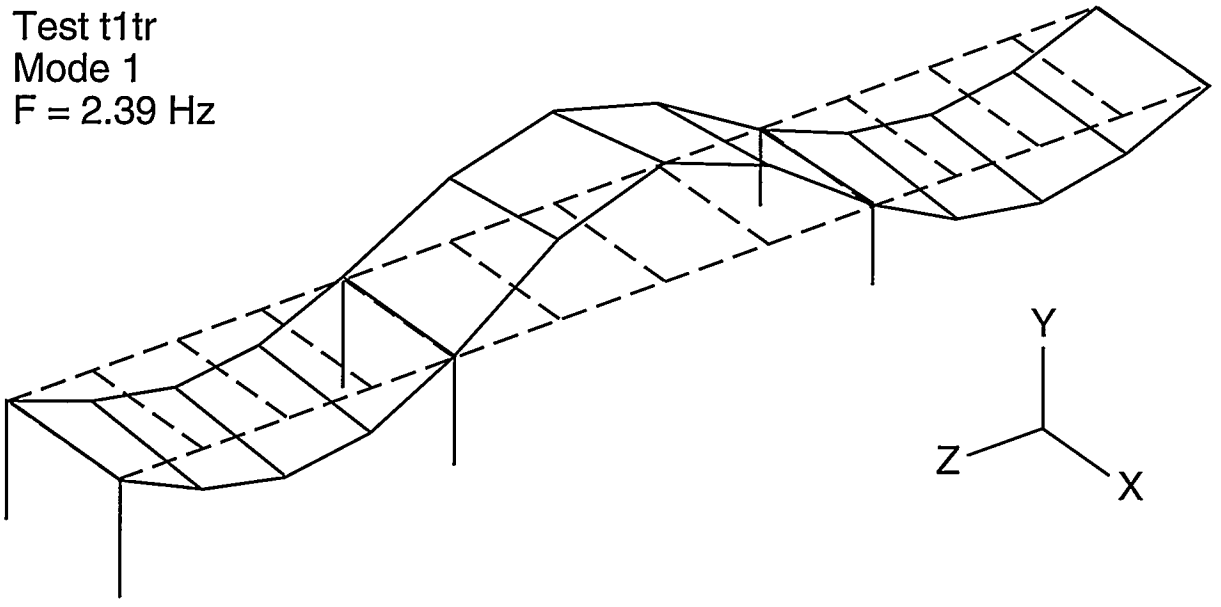

Fig. 10. First flexural mode identified from ambient vibration data, test t1tr.

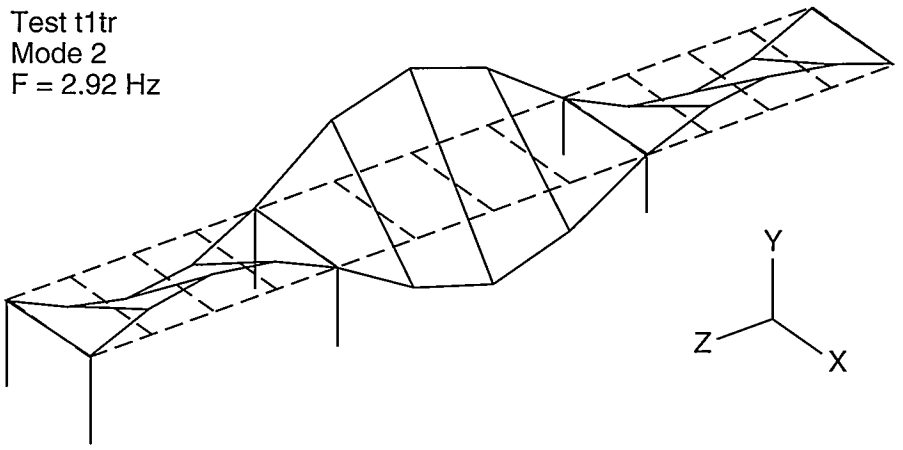

Fig. 11. First torsional mode identified from ambient vibration data, test t1tr.

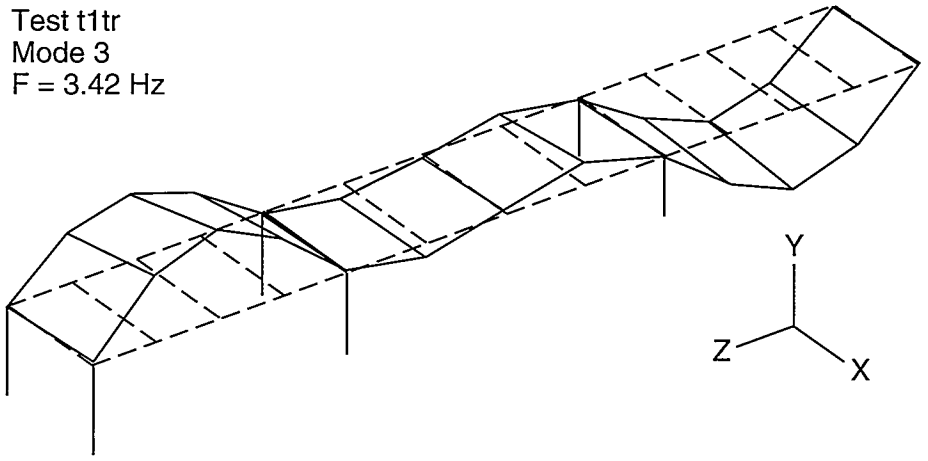

Fig. 12. Second flexural mode identified from ambient vibration data, test t1tr.

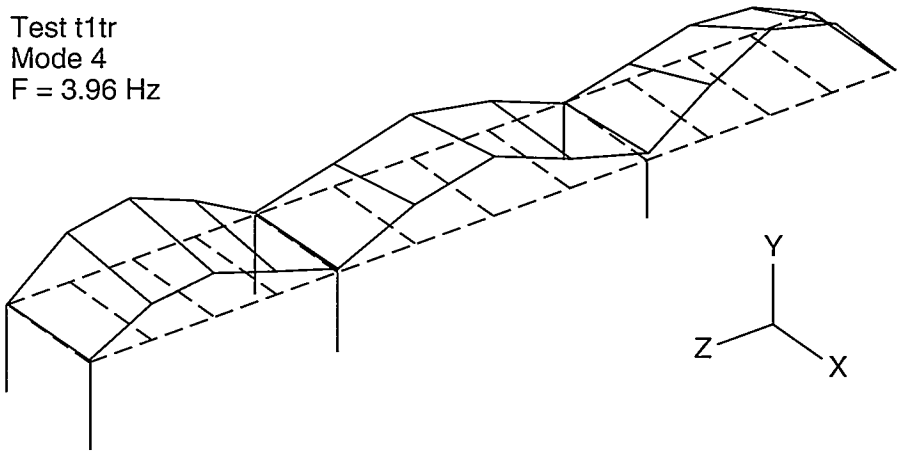

Fig. 13. Third flexural mode identified from ambient vibration data, test t1tr.

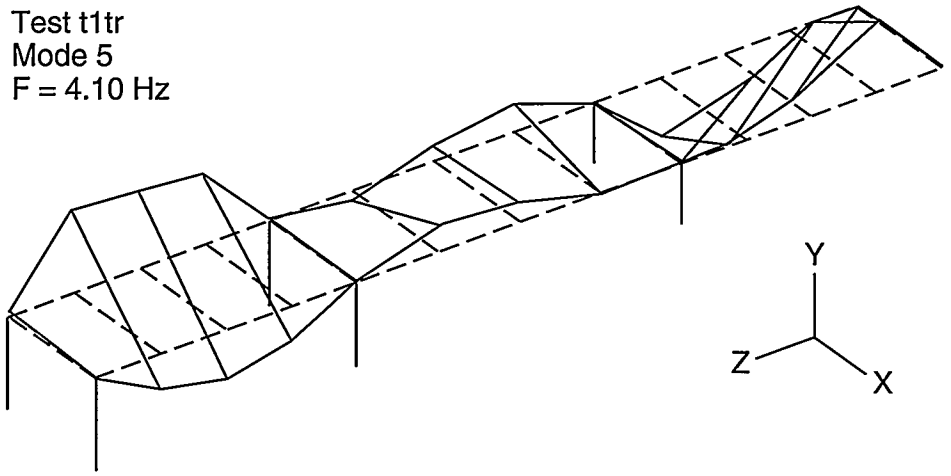

Fig. 14. Second torsional mode identified from ambient vibration data, test t1tr.

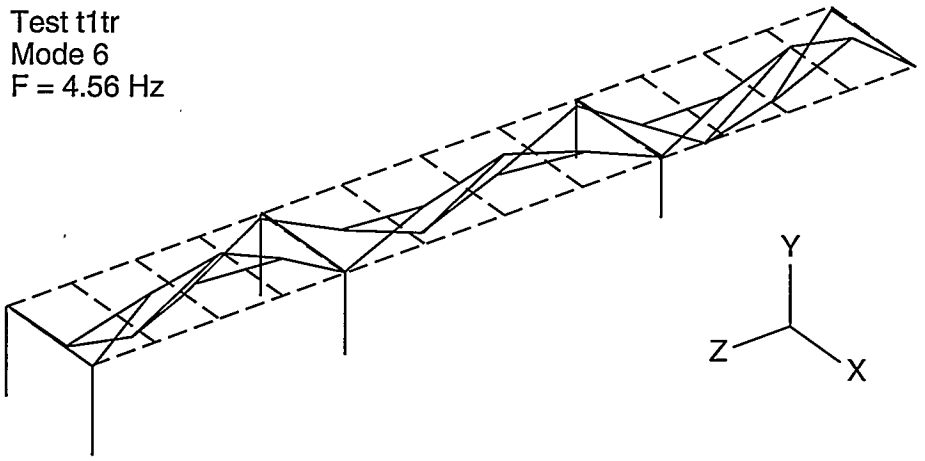

Fig. 15. Third torsional mode identified from ambient vibration data, test t1tr.

The mode shapes for the first six modes identified from test t1tr are shown in Figs 10 through 15. Table I summarizes the resonant frequencies and modal damping values calculated from the different tests where the global Y direction response was measured. Both parameters were calculated in a global manner using a complex exponential curve-fitting method, that is, each measured CPS was used to estimate the parameter, and the mean value from the 26 measurements was then calculated. These mean values appear in Table I.

TABLE I

Resonant Frequencies and Modal Damping Values Identified from Ambient Vibration Response in the Global Y-Direction

Test*	Mode 1 Freq. (Hz)/ Damp. (%)	Mode 2 Freq. (Hz)/ Damp. (%)	Mode 3 Freq. (Hz)/ Damp. (%)	Mode 4 Freq. (Hz)/ Damp. (%)	Mode 5 Freq. (Hz)/ Damp. (%)	Mode 6 Freq. (Hz)/ Damp. (%)
t1tr 0–6.25 Hz 100 Ave. S-2 Ref.	2.39/ 1.28	2.92/ 1.18	3.42/ 1.00	3.96/ 0.94	4.10/ 1.58	4.56/ 1.56
t2tr 0–25 Hz 75 Ave. S-2 Ref.	2.43/ 2.39	2.98/ 2.52	3.51/ 1.06	3.97/ 1.20	4.17/ 1.79	4.64/ 1.29
t10tr 0–6.25 Hz 100 Ave. S-6 Ref.	2.42/ 1.15	2.93/ 1.18	3.46/ 0.85	3.99/ 0.70	4.12/ 0.59	4.61/ 0.97
t11tr 0–25 Hz 75 Ave. S-6 Ref.	2.42/ 2.15	2.99/ 1.78	3.51/ 1.37	4.03/ 1.74	4.18/ 1.52	4.70/ 1.18
t15tr 0–12.5 Hz 30 Ave. S-2 Ref.	2.52/ 1.28	3.04/ 0.38	3.53/ 0.89	4.10/ 1.08	4.17/ 0.92	4.71/ 0.60

* The test designation is followed by the frequency range of the CPS, the number of averages used to estimate the CPS, and the reference channel location that is shown in Fig. 9.

These results showed that ambient vibration from traffic provided an adequate source of input for identifying the dynamic properties of the bridge. The results obtained with SNL's ambient vibration system identification method were repeatable (resonant frequency values measured with traffic on the bridge did not vary more than 3%) and were independent of the selected reference measurement. This method allowed closely spaced modes such as Modes 4 and 5 to be identified, and this method identified the associated modal damping values. During test t15tr, when traffic was not on the bridge, generally higher frequencies were measured for each mode as compared to the results from tests when traffic was on the bridge. These higher frequencies are attributed to the reduced mass of the system that resulted from removing the traffic from the bridge.

Other observations made during these tests are that doubling the frequency resolution had little effect on the identified resonant frequencies. However, the increased frequency resolution did improve the ability to identify the closely spaced modes. Damping values were particularly sensitive to the increased frequency resolution, and these values

appeared to decrease with the increased frequency resolution. The modes were lightly damped with modal damping values ranging from 0.4% to 2.59%, and can be accurately approximated as real modes. Phase angles were typically close to either 0 or 180 degrees. Background sources of ambient vibration from traffic on the adjacent bridges were of sufficient magnitude that the dynamic properties of the structure could be determined by measuring the response to this excitation source as was done in test t15tr.

III. B. Forced Vibration Testing, Undamaged

From August 31st through September 2nd, 1993, a series of forced vibration tests were conducted on the undamaged bridge. Eastbound traffic had been transferred to a new bridge just south of the one being tested. The westbound traffic continued on the original westbound bridge. SNL provided a hydraulic shaker that generated the measured force input. Excitation from traffic on the adjacent bridges could be felt when the shaker was not running. Wind, although not measured, was not considered significant during these tests.

The Sandia shaker consists of a 21,700-lb. reaction mass supported by three air springs resting on top of 55-gallon drums filled with sand. A 2200-lb. hydraulic actuator bolted under the center of the mass and anchored to the top of the bridge deck provided the input force to the bridge. A schematic of the shaker is shown in Fig. 16, and Fig. 17 shows the shaker in place on the bridge. A random-signal generator was used to produce a uniform random signal that was band-passed between 2 Hz and 12 Hz before inputting the signal to an amplifier. The amplifier gain was controlled manually to provide an approximately 2000-lb. peak, random force input. An accelerometer mounted on the reaction mass was used to measure the force input to the bridge. This indirect force measurement gives the total force transferred to the bridge through the 55-gallon drums as well as the actuator. The shaker was located over the south plate girder directly above point S-3 in Fig. 9. The accelerometer used to measure force was oriented such that a positive force corresponded to the positive global Y direction shown in Fig. 9. The level of excitation during the forced test was less than the levels produced by the large trucks passing the bridge, but it was higher than the level of excitation produced by cars.

Forced vibration tests were conducted using a random input so that ESA-EA personnel could perform experimental modal analyses of the bridge. In this context experimental modal analysis refers to the procedure whereby a measured excitation (random, sine, or impact force) is applied to a structure, and the structure's response (acceleration, velocity, or displacement) is measured at discrete locations that are representative of the structure's motion. Both the excitation and the response time histories are transformed into the frequency domain in the form of frequency response functions (FRF, the Fourier transform of the response normalized by the Fourier transform of the input). Modal parameters (resonant frequencies, mode shapes, modal damping) can be determined by curve-fitting a Laplace domain representation of the equations of motion to the measured frequency domain data (Ewins, 1985).

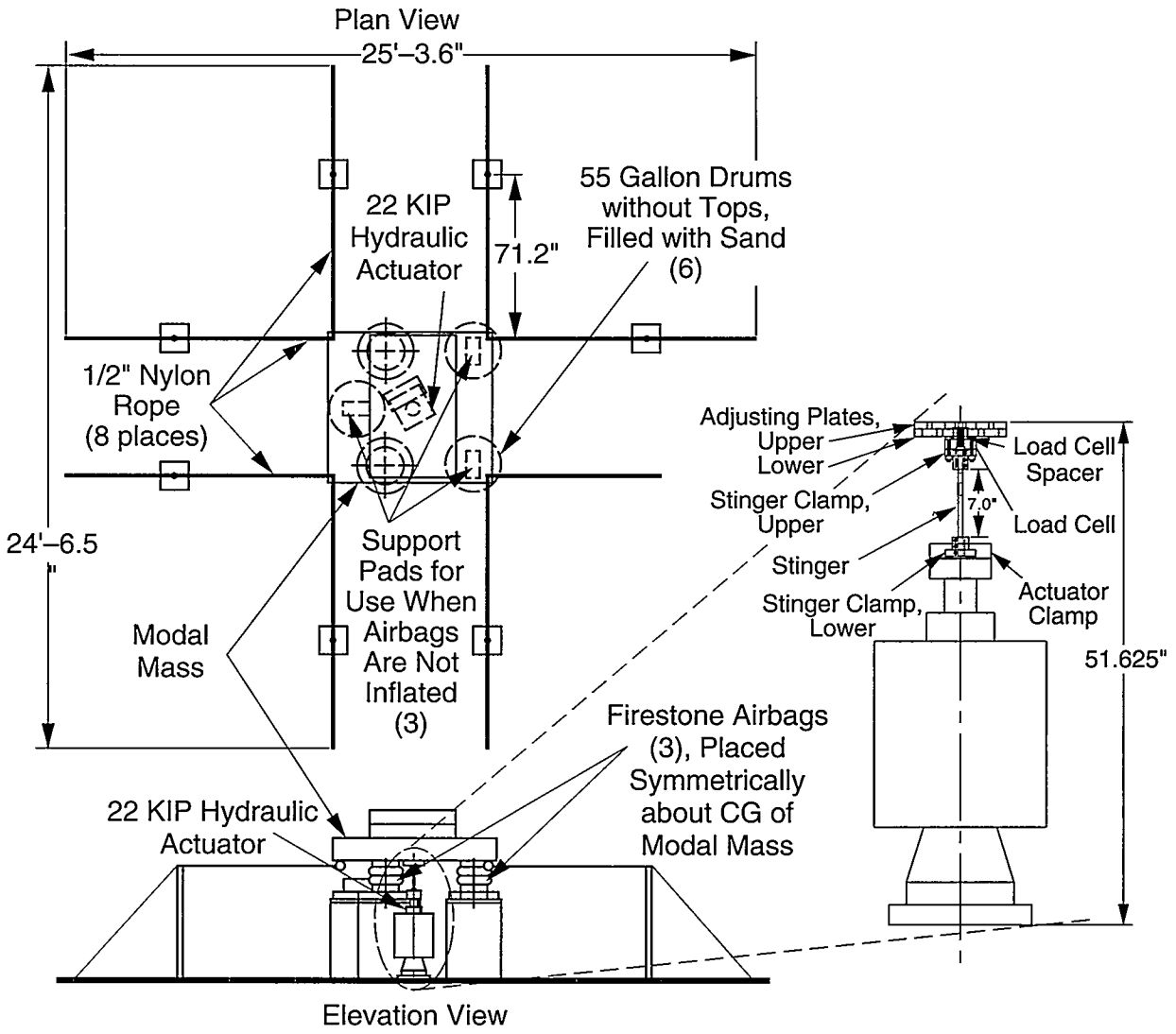

Fig. 16. Schematic depiction of the Sandia shaker.

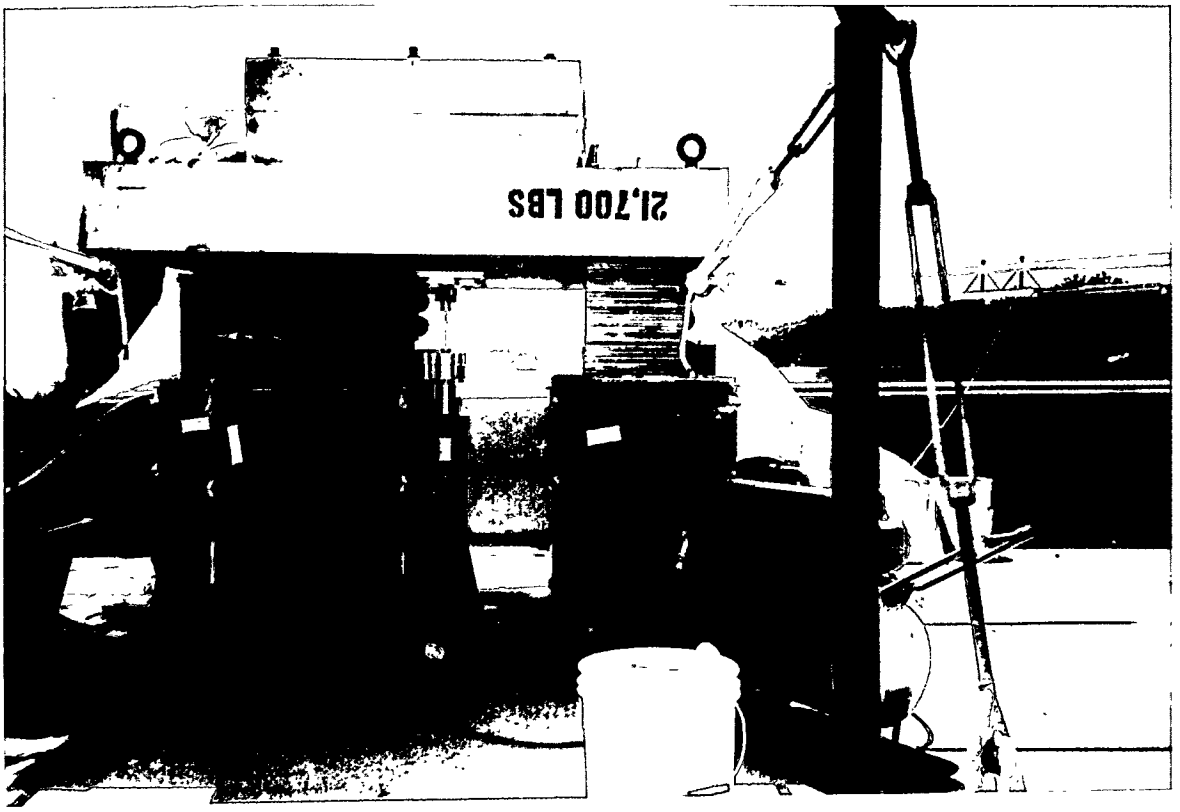

Fig. 17. The Sandia shaker in place on the I-40 Bridge.

The data acquisition system, mounting blocks, cabling, accelerometers, and generator used for the forced vibration tests were identical to those used for the ambient vibration tests. An additional input module was used to monitor the accelerometer located on the reaction mass. Sampling parameters were specified so that responses with frequency content in the range of 0–12.5 Hz could be measured. All computed frequency domain quantities were based on 30 averages with no overlap. A Hanning window was applied to all time samples used in these calculations.

A rational-fraction, polynomial, global, curve-fitting algorithm in a commercial modal analysis software package (Structural Measurements Systems, 1987) was used to fit the analytical models to the measured FRF data and to extract resonant frequencies, mode shapes, and modal damping values. Figures 18 through 23 show the first six modes of the undamaged bridge identified from these data. A comparison of these figures with Figs 10 through 15 reveal that the dynamic properties identified from the forced vibration tests are similar to those identified by the ambient vibration tests.

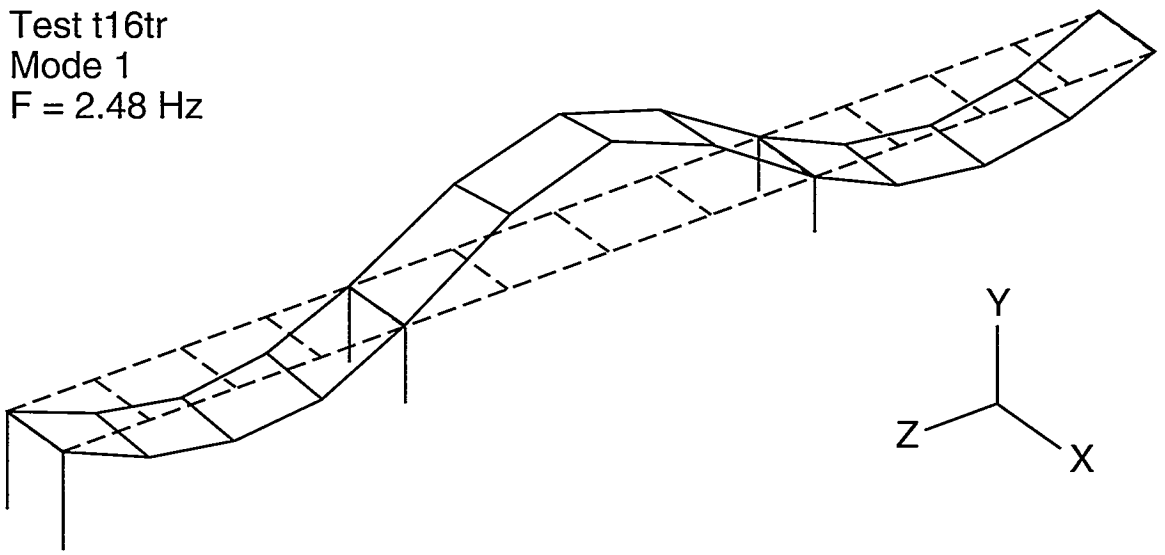

Fig. 18. First flexural mode identified from undamaged forced vibration data, test t16tr.

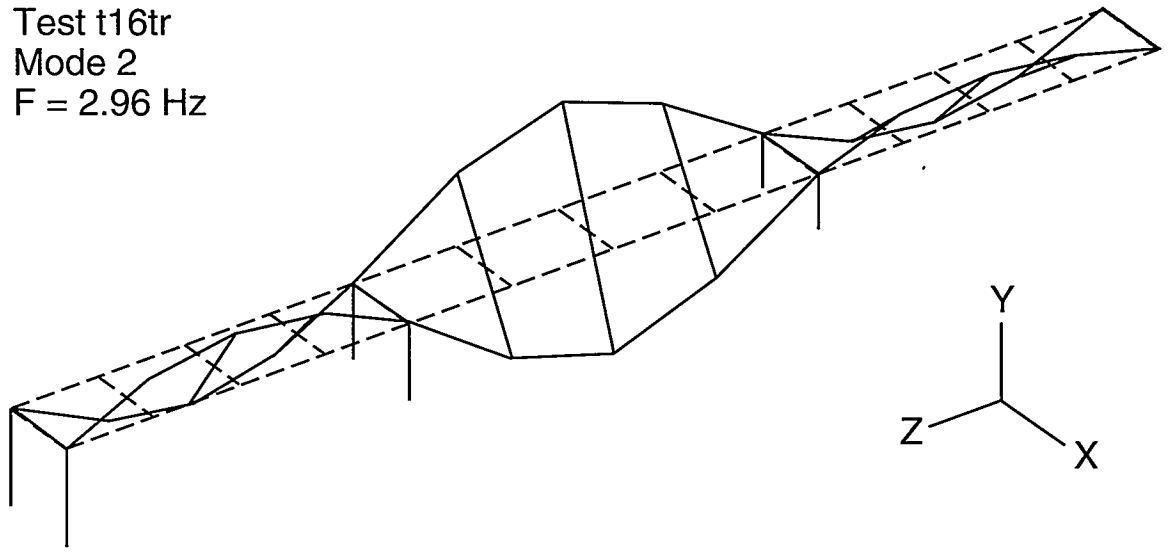

Fig. 19. First torsional mode identified from undamaged forced vibration data, test t16tr.

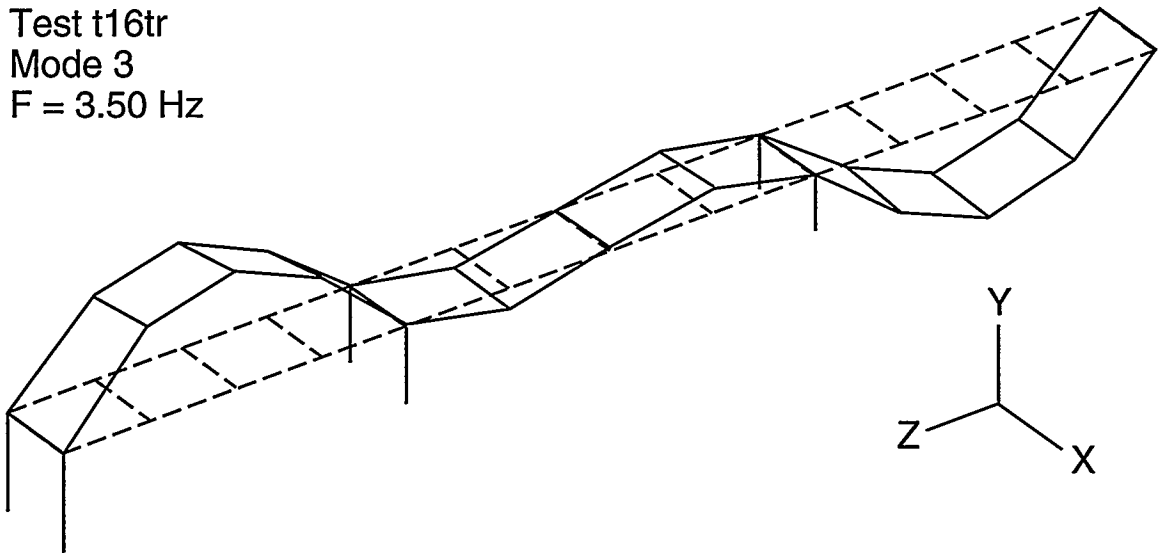

Fig. 20. Second flexural mode identified from undamaged forced vibration data, test t16tr.

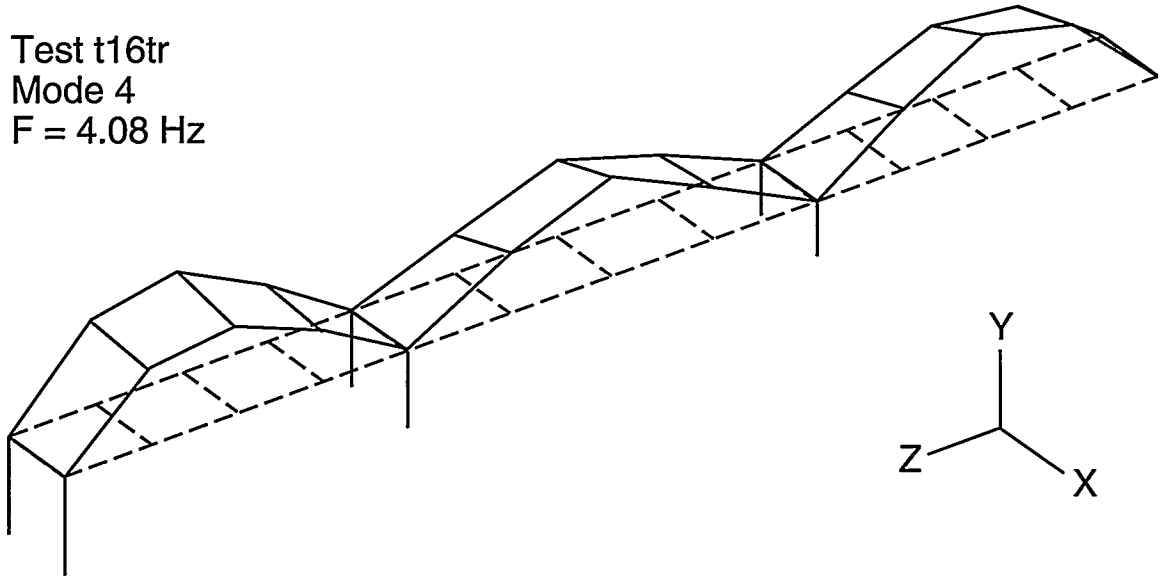

Fig. 21. Third flexural mode identified from undamaged forced vibration data, test t16tr.

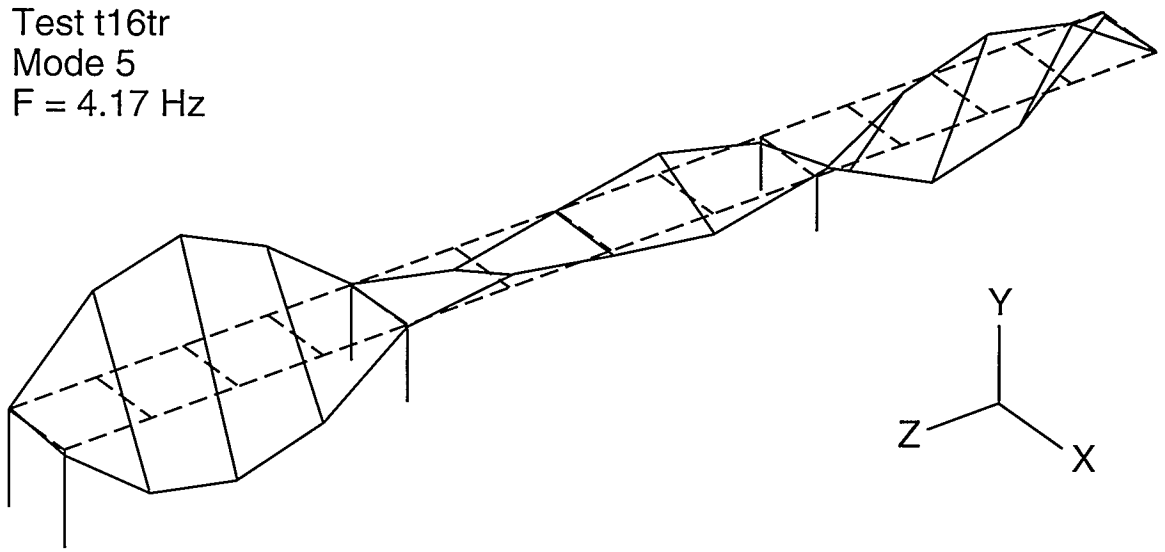

Fig. 22. Second torsional mode identified from undamaged forced vibration data, test t16tr.

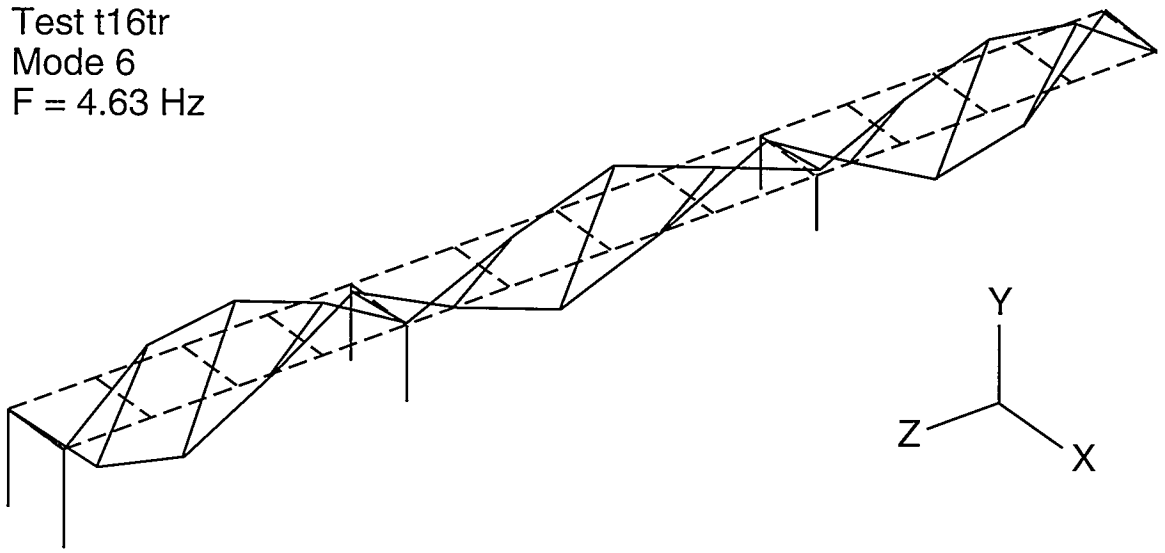

Fig. 23. Third torsional mode identified from undamaged forced vibration data, test t16tr.

Table II compares the resonant frequencies and modal damping values determined from the ambient vibration tests with those determined during the forced vibration tests. The forced vibration test is designated t16tr in this table. From this table it is evident that the dynamic properties measured during the forced vibration test fall within the range of those measured during the various ambient vibration tests. The dynamic properties measured during the forced vibration tests are nearly identical to those measured during ambient vibration test t15tr that was conducted immediately before the forced vibration test. Although the damping values show considerable scatter in terms of percent differences for particular modes, the average modal damping values for tests t15tr and t16tr, 0.86% and 1.13%, respectively, are consistent. Typically, engineers will assume the same damping value, specified to one significant digit because of uncertainties associated with this parameter, for all modes when performing a dynamic analysis. This practical consideration again shows that the damping values identified are consistent within the accuracy that damping is usually specified.

TABLE II

Resonant Frequencies and Modal Damping Values Identified from Ambient Vibration Response Compared with Similar Quantities Identified from Forced Vibration Tests

	Mode 1	Mode 2	Mode 3	Mode 4	Mode 5	Mode 6
Test	Freq. (Hz)/ Damp. (%)	Freq. (Hz)/ Damp. (%)	Freq. (Hz)/ Damp. (%)	Freq. (Hz)/ Damp. (%)	Freq. (Hz)/ Damp. (%)	Freq. (Hz)/ Damp. (%)
t1tr (ambient)	2.39/ 1.3	2.92/ 1.2	3.42/ 1.0	3.96/ 0.94	4.10/ 1.6	4.56/ 1.6
t2tr (ambient)	2.43/ 2.4	2.98/ 2.5	3.51/ 1.1	3.97/ 1.2	4.17/ 1.8	4.64/ 1.3
t10tr (ambient)	2.42/ 1.2	2.93/ 1.2	3.46/ 0.85	3.99/ 0.70	4.12/ 0.59	4.61/ 0.97
t11tr (ambient)	2.42/ 2.2	2.99/ 1.8	3.51/ 1.4	4.03/ 1.7	4.18/ 1.5	4.70/ 1.2
t15tr (ambient)	2.52/ 1.3	3.04/ 0.38	3.53/ 0.89	4.10/ 1.1	4.17/ 0.92	4.71/ 0.60
t16tr (forced)	2.48/ 1.1	2.96/ 1.3	3.50/ 1.5	4.08/ 1.1	4.17/ 0.86	4.63/ 0.92

A modal assurance criterion (MAC), sometimes referred to as a modal correlation coefficient (Ewins, 1985) was calculated to quantify the correlation between mode shapes measured during different tests. The MAC makes use of the orthogonality of the mode shapes to compare either two modes from the same test or two modes from different tests. If the modes are identical, a scalar value of one is calculated by the MAC. If the modes are orthogonal and dissimilar, a value of zero is calculated. The MAC that compares mode i and j has the form

$$MAC(i,j) = \frac{\left|\sum_{k=1}^{n} (\phi_j)_k (\phi_i)^*_k\right|^2}{\left(\sum_{k=1}^{n} (\phi_j)_k (\phi_j)^*_k\right)\left(\sum_{k=1}^{n} (\phi_i)_k (\phi_i)^*_k\right)} \quad (1)$$

where $(\phi)_k$ is an element of the mode-shape vector and the asterisk denotes complex conjugate. The value of the MAC does not actually quantify the correlation between modes. Ewins points out that, in practice, correlated modes will yield a value greater than 0.9, and uncorrelated modes will yield a value less than 0.05. The MAC is not affected by a scalar multiple.

The MAC can be applied to compare the mode shapes from the forced vibration tests with the modes determined during the ambient vibration testing. Table III shows such a comparison with the ambient-vibration, mode-shape data obtained during test t1tr. Table III shows that similar mode shapes are being identified in each case. Modes 4 and 5, which are closely spaced and which were difficult to identify during several ambient vibration tests did not always show good correlation with the modes determined during the forced vibration tests.

TABLE III

Modal Assurance Criteria:
Mode Shapes Identified from Ambient Vibration Test t1tr Compared with Mode Shapes Identified from Forced Vibration Tests on the Undamaged Structure, Test t16tr

Mode/test	1/t16tr	2/t16tr	3/t16tr	4/t16tr	5/t16tr	6/t16tr
1/t1tr	0.989	0.008	0.000	0.004	0.002	0.001
2/t1tr	0.004	0.985	0.000	0.001	0.001	0.004
3/t1tr	0.002	0.003	0.984	0.000	0.009	0.001
4/t1tr	0.005	0.002	0.001	0.901	0.102	0.009
5/t1tr	0.000	0.001	0.005	0.066	0.917	0.005
6/t1tr	0.001	0.003	0.002	0.004	0.004	0.984

III. C. Forced Vibration Testing, Damaged

From September 3rd through 11th, 1993, four different levels of damage were introduced into the middle span of north plate girder. Forced vibration tests similar to those done on the undamaged structure were repeated after each level of damage had been introduced. Weather conditions during these tests were similar to those reported for the forced vibration tests. Background sources of vibration were also similar.

III. C. 1. Damage Description

The damage that was introduced was intended to simulate fatigue cracking that has been observed in plate-girder bridges. This type of cracking results from out-of-plane bending of the web and usually begins at welded attachments to the web such as the seats supporting the floor beams. Four levels of damage were introduced to the middle span of the north plate girder close to the seat supporting the floor beam at midspan. Damage was introduced by making various torch cuts in the web and flange of the girder. The first level of damage consisted of a two-foot-long cut through the web approximately 3/8-in-wide centered at midheight of the web. Next, this cut was continued to the bottom of the web. During this cut the web, on either side of the cut, bent out of plane approximately 1 in. The flange was then cut halfway in from either side directly below cut in the web. Finally, the flange was cut completely through leaving the top 4 ft of the web and the top flange to carry the load at this location. The various levels of damage are shown in Figs. 24 through 27.

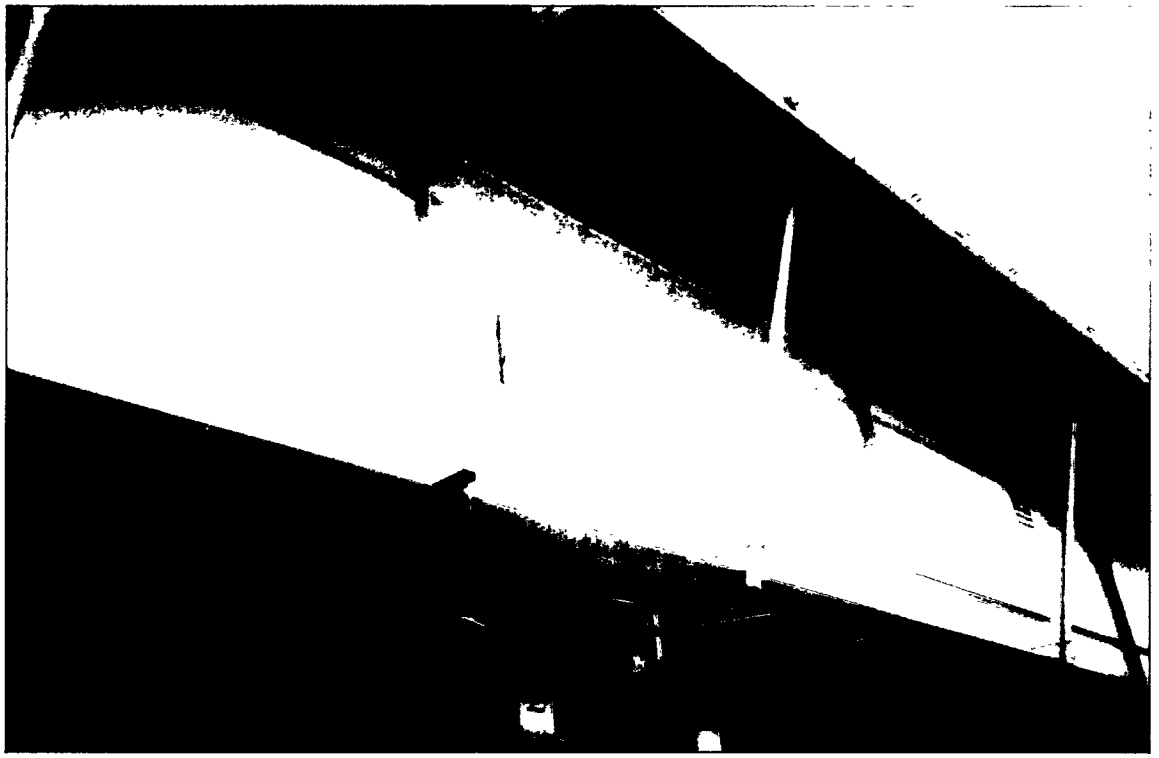

Fig. 24. First stage of damage: two-foot cut at the center of the web.

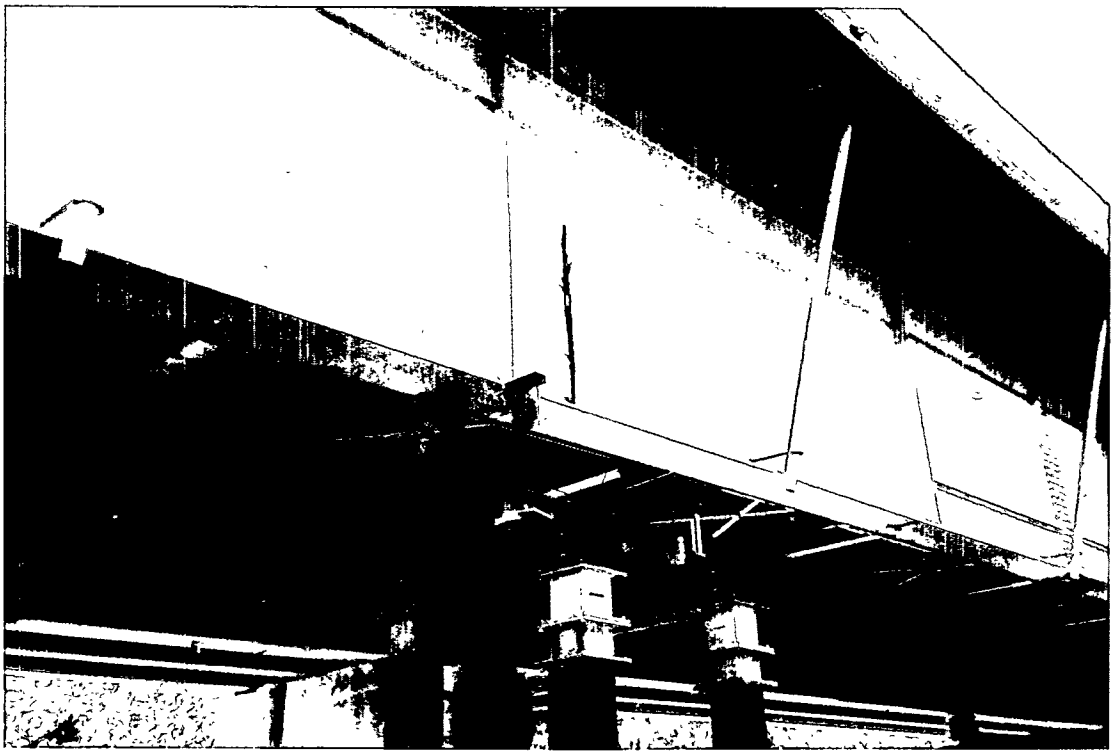

Fig. 25. Second stage of damage: six-foot cut from the center of the web to the bottom flange.

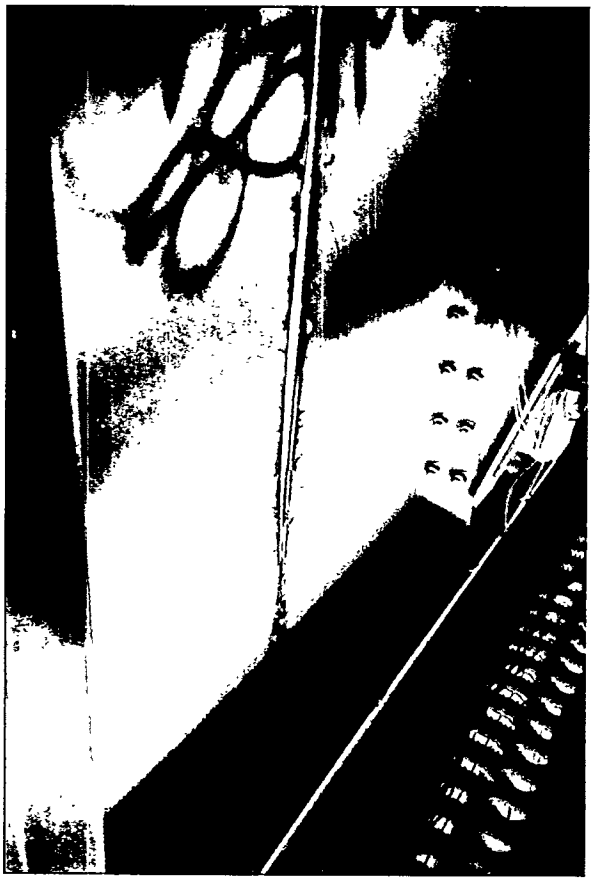

Fig. 26. Third stage of damage: six-foot cut in the web and cuts through half the bottom flange on either side of the web.

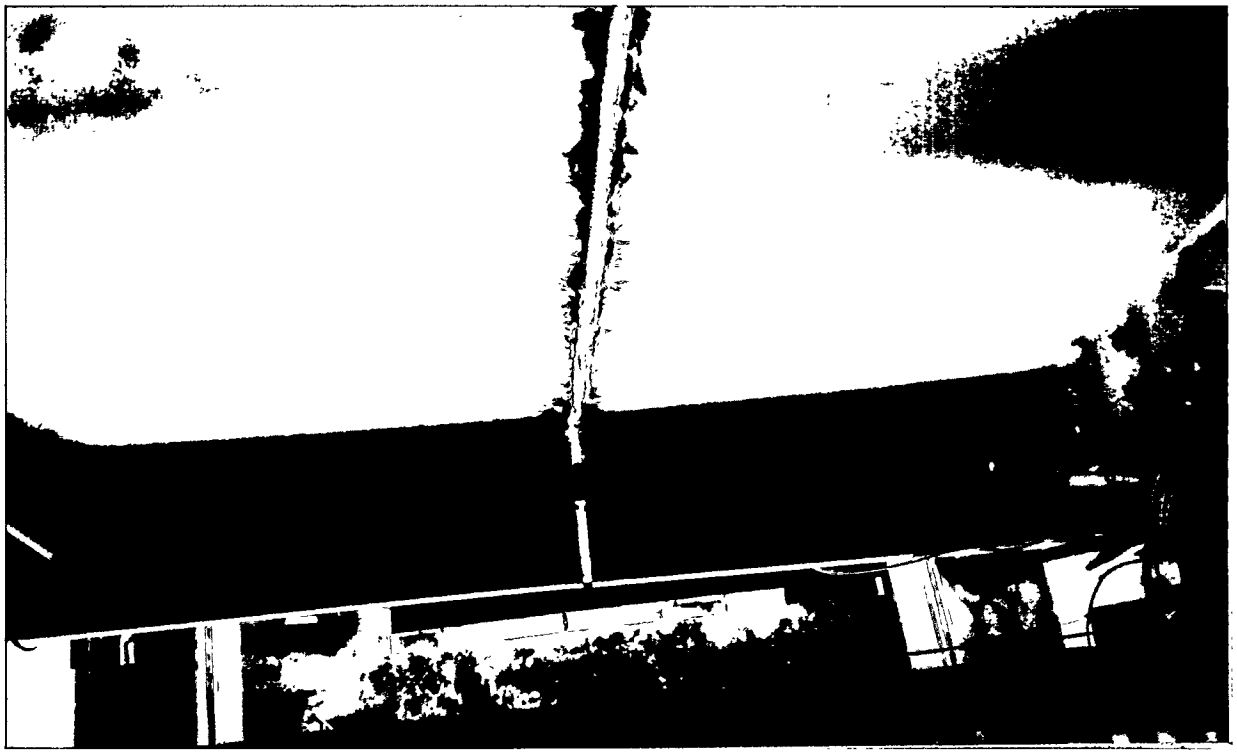

Fig. 27. Fourth stage of damage: six-foot cut in the web and cut through the entire bottom flange.

III. C. 2. Experimental Procedure and Results

Experimental modal analyses were repeated after each level of damage had been introduced. The experimental procedures and data acquisition equipment used were identical to those used for the undamaged forced vibration tests summarized in Section III. B. Table IV summarizes the forced vibration tests that were performed.

FRF magnitudes for locations S-3 and N-7 are plotted for each level of damaged and compared to the similar FRFs measured on the undamaged structure in Figures 28 and 29, respectively. The figures show that little change in the resonant frequencies and widths of the resonance (damping) occur until the final stage of damage is introduced.

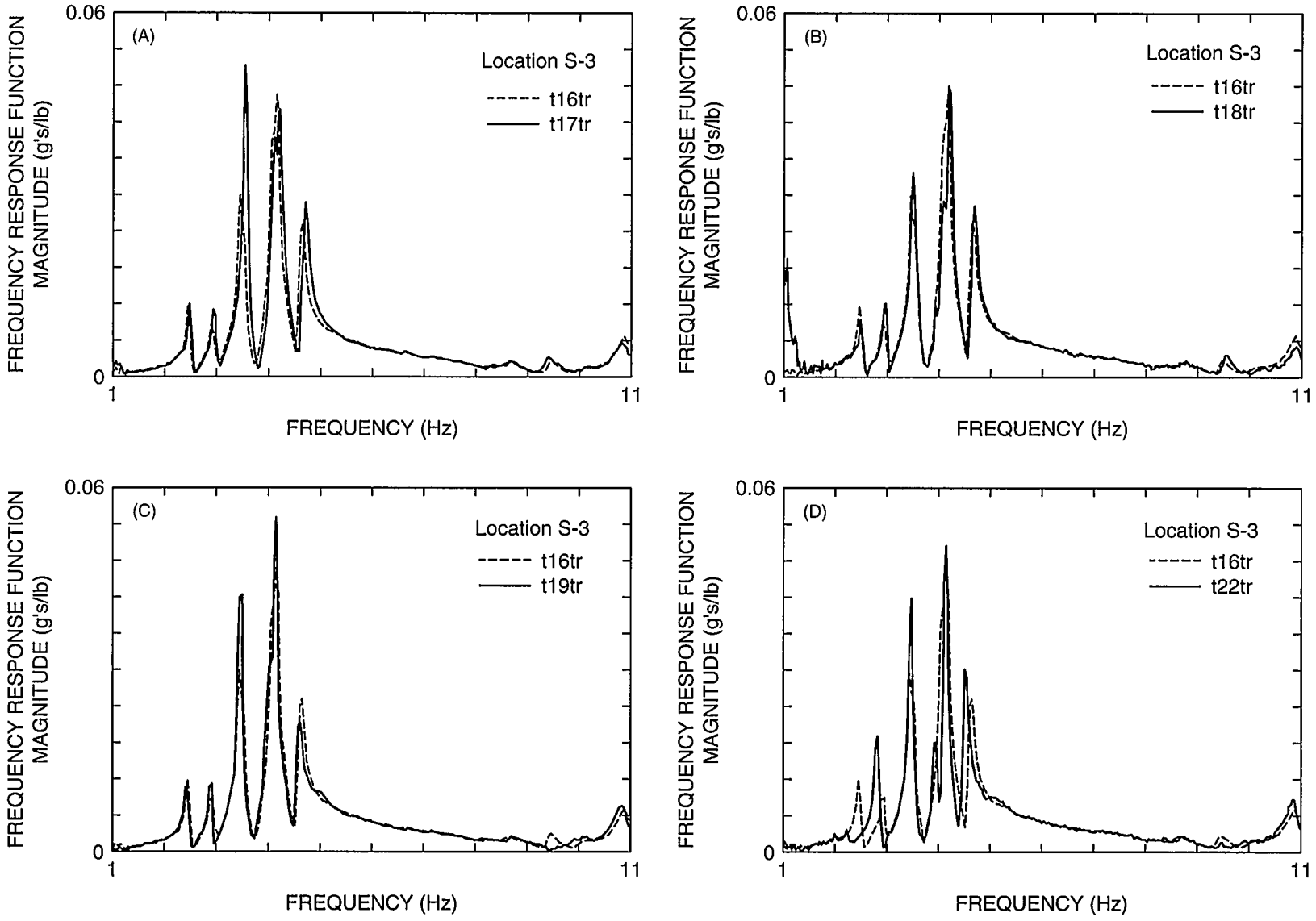

Fig. 28. FRF magnitude measured at location S-3 during each of the damaged forced vibration tests compared with the FRF measured at location S-3 during the undamaged forced vibration test (test t16tr).

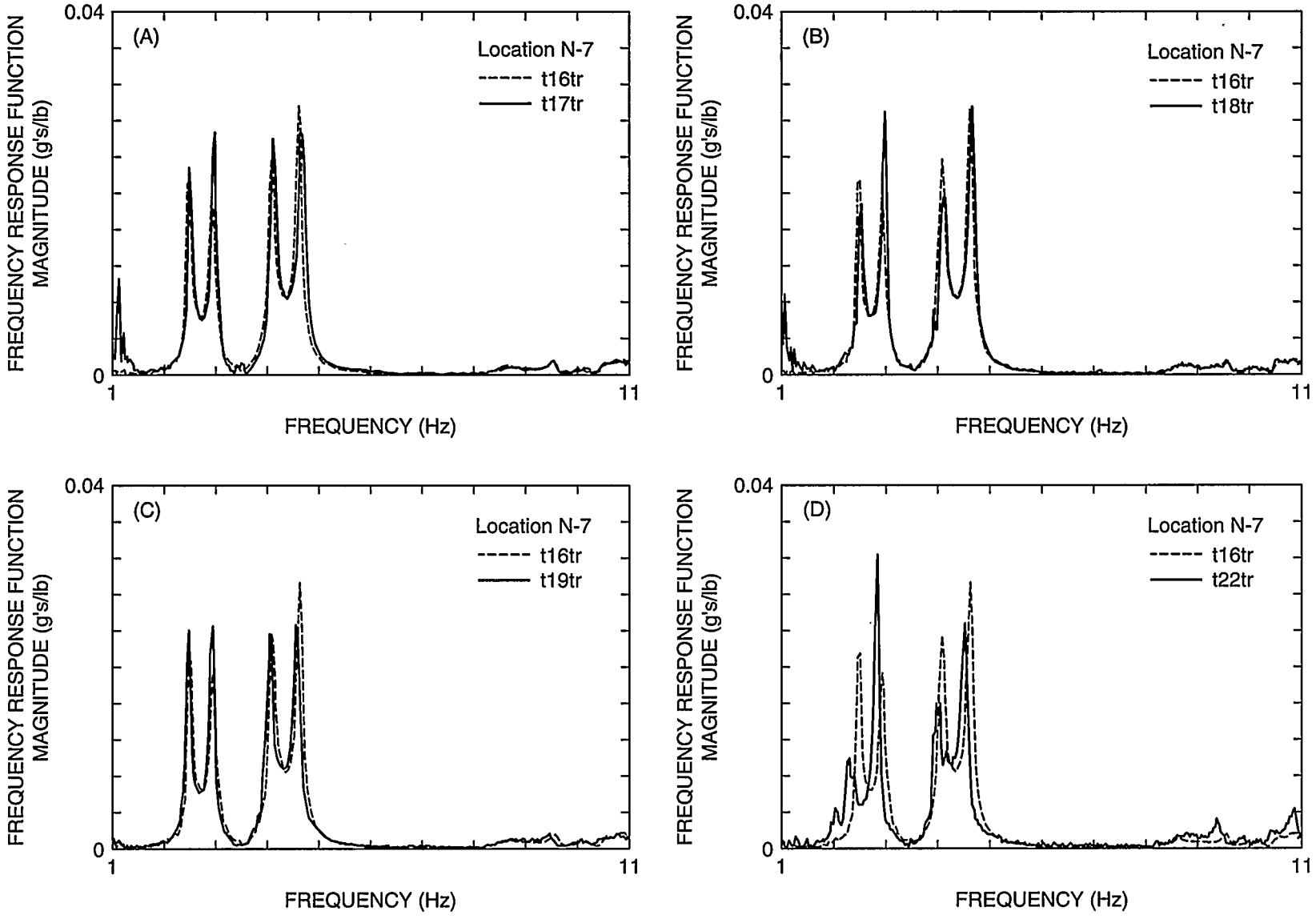

Fig. 29. FRF magnitude measured at location N-7 during each of the damaged forced vibration tests compared with the FRF measured at location N-7 during the undamaged forced vibration test (test t16tr).

TABLE IV

Summary of Forced Vibration Tests

Test Designation	Frequency Range (Hz)	No. of Averages	Date/Time	Dynamic Range Accelerometers / Force Transducer	Damage Description
t16tr	0–2.5	30	Sept. 2, 11:08–11:33 AM	1 Vp, 3.16 Vp	undamaged
t17tr	0–12.5	30	Sept. 2, 2:25–2:40 PM	1 Vp, 3.16 Vp	2 ft cut at the center of the web
t18tr	0–12.5	30	Sept. 3, 12:00–12:46 PM	2 Vp, 6.31 Vp	6 ft cut in the web to the bottom flange
t19tr	0–12.5	30	Sept. 7, 9:32–9:55 AM	2 Vp, 6.31 Vp	bottom 6 ft of the web and half of the flange cut
t22tr	0–12.5	30	Sept. 8, 9:52–10:17 AM	3.98 Vp, 6.31 Vp	bottom 6 ft of the web and entire flange cut

Table V summarizes the resonant frequency and modal damping data obtained during each modal test of the damaged bridge. Also shown in Table V are similar results from the ambient vibration tests and the undamaged forced vibration test. No change in the dynamic properties can be observed until the final level of damage is introduced. At the final level, test t22tr, the resonant frequencies for the first two modes have dropped to values 7.6 and 4.4 percent less, respectively, than those measured during the undamaged tests. It is of interest to note that changes of similar magnitude are observed between the two ambient vibration tests performed on the undamaged structure at different times. For modes where the damage was introduced near a stress node for that mode (Modes 3 and 5) no significant changes in resonant frequencies can be observed.

TABLE V

Resonant Frequencies and Modal Damping Values Identified from Ambient Vibration Response Compared with Similar Quantities Identified from Undamaged and Damaged Forced Vibration Tests

	Mode 1	Mode 2	Mode 3	Mode 4	Mode 5	Mode 6
Test	Freq. (Hz)/ Damp. (%)	Freq. (Hz)/ Damp. (%)	Freq. (Hz)/ Damp. (%)	Freq. (Hz)/ Damp. (%)	Freq. (Hz)/ Damp. (%)	Freq. (Hz)/ Damp. (%)
t1tr (ambient)	2.39/ 1.28	2.92/ 1.18	3.42/ 1.00	3.96/ 0.94	4.10/ 1.58	4.56/ 1.56
t15tr (ambient)	2.52/ 1.28	3.04/ 0.38	3.53/ 0.89	4.10/ 1.08	4.17/ 0.92	4.71/ 0.60
t16tr (forced, undamaged)	2.48/ 1.06	2.96/ 1.29	3.50/ 1.52	4.08/ 1.10	4.17/ 0.86	4.63/ 0.92
t17tr (forced, after 1st cut)	2.52/ 1.20	3.00/ 0.80	3.57/ 0.87	4.12/ 1.00	4.21/ 1.04	4.69/ 0.90
t18tr (forced, after 2nd cut)	2.52/ 1.33	2.99/ 0.82	3.52/ 0.95	4.09/ 0.85	4.19/ 0.65	4.66/ 0.84
t19tr (forced, after 3rd cut)	2.46/ 0.82	2.95/ 0.89	3.48/ 0.92	4.04/ 0.81	4.14/ 0.62	4.58/ 1.06
t22tr (forced, after final cut)	2.30/ 1.60	2.84/ 0.66	3.49/ 0.80	3.99/ 0.80	4.15/ 0.71	4.52/ 1.06

Table VI shows the MAC values that are calculated when mode shapes from tests t17tr, t18tr, t19tr, and t22tr are compared to the modes calculated from the undamaged forced vibration test, t16tr. The MAC values show no change in the mode shapes for the first three stages of damage. When the final level of damage is introduced, significant drops in the MAC values for modes 1 and 2 are noticed. These two modes are shown in Figs. 30 and 31 and can be compared to similar modes identified for the undamaged bridge in Figs. 18 and 19. When the modes have a node near the damage location (Modes 3 and 5), no significant reduction in the MAC values are observed, even for the final stage of damage, and a plot of this mode shape from test t22tr, Fig. 32, shows no change from the corresponding undamaged mode, Fig. 20. Examination of mode shapes from tests t17tr, t18tr, and t19tr reveal no change from the undamaged mode shapes shown in Figs. 18 through 23, as would be indicated from the MAC values shown in Table VI.

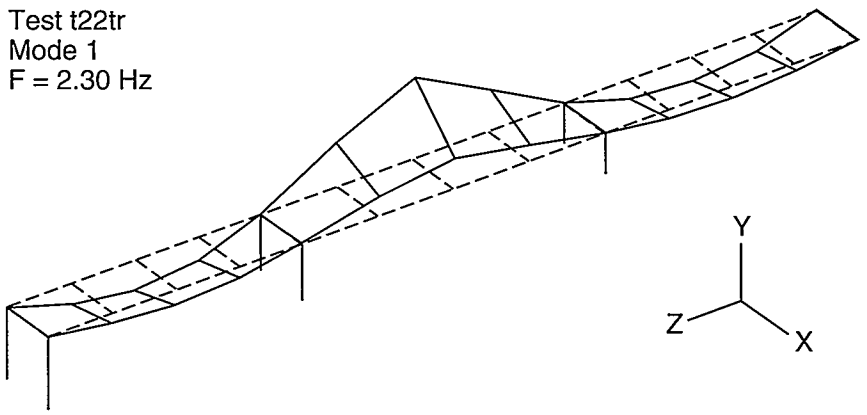

Fig. 30. The first flexural mode measured after the final damage stage, test t22tr.

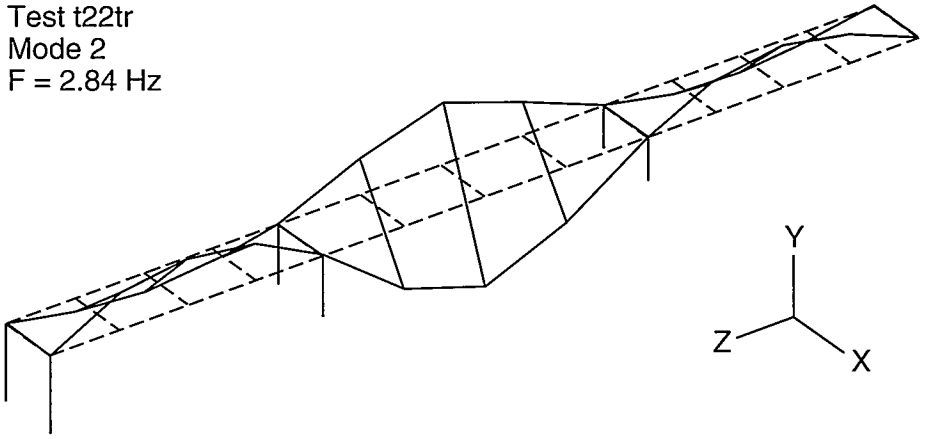

Fig. 31. The first torsional mode measured after the final damage stage, test t22tr.

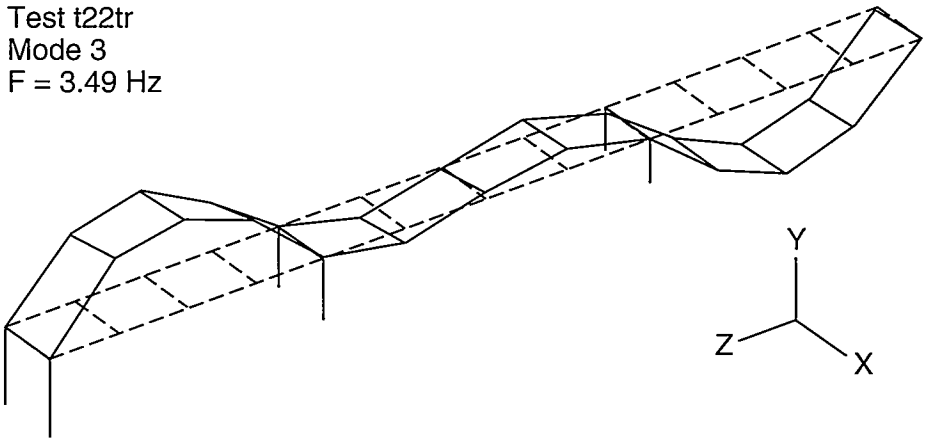

Fig. 32. The second flexural mode measured after the final damage stage, test t22tr.

TABLE VI

Modal Assurance Criteria:
Undamaged and Damaged Forced Vibration Tests

Modal Assurance Criteria		t16tr X t17tr				
Mode	1	2	3	4	5	6
1	0.996	0.006	0.000	0.003	0.001	0.003
2	0.000	0.997	0.000	0.005	0.004	0.003
3	0.000	0.000	0.997	0.003	0.008	0.001
4	0.004	0.003	0.006	0.984	0.026	0.011
5	0.001	0.008	0.003	0.048	0.991	0.001
6	0.001	0.006	0.000	0.005	0.005	0.996

Modal Assurance Criteria		t16tr X t18tr				
Mode	1	2	3	4	5	6
1	0.995	0.004	0.000	0.004	0.001	0.002
2	0.000	0.996	0.000	0.003	0.002	0.002
3	0.000	0.000	0.999	0.006	0.004	0.000
4	0.003	0.006	0.005	0.992	0.032	0.011
5	0.001	0.006	0.008	0.061	0.997	0.004
6	0.002	0.004	0.000	0.005	0.005	0.997

Modal Assurance Criteria		t16tr X t19tr				
Mode	1	2	3	4	5	6
1	0.997	0.002	0.000	0.005	0.001	0.001
2	0.000	0.996	0.001	0.003	0.002	0.002
3	0.000	0.000	0.999	0.006	0.006	0.000
4	0.003	0.005	0.004	0.981	0.032	0.011
5	0.001	0.006	0.004	0.064	0.995	0.003
6	0.002	0.002	0.000	0.004	0.009	0.995

Modal Assurance Criteria		t16tr X t22tr				
Mode	1	2	3	4	5	6
1	0.821	0.168	0.002	0.001	0.000	0.001
2	0.083	0.884	0.001	0.004	0.001	0.002
3	0.000	0.000	0.997	0.005	0.007	0.001
4	0.011	0.022	0.006	0.917	0.001	0.048
5	0.001	0.006	0.003	0.046	0.988	0.002
6	0.005	0.005	0.000	0.004	0.009	0.965

IV. DETAILED FINITE ELEMENT ANALYSIS

Detailed finite element analyses were performed before the experimental modal analyses to aid in the selection of instrumentation locations and to give indications of the frequencies associated with the lower modes of the structure. All calculations were performed with the ABAQUS finite element code (ABAQUS User Manual (1994)) on a CRAY Y-MP computer. Mesh generation and post-processing were done with PATRAN (P3/PATRAN User Manual (1992)) on a Silicon Graphics workstation. In addition to providing information that would aid in the selection of instrumentation options, these models can be used in conjunction with experimental modal data to obtain an indirect indication of the composite action exhibited by the bridge. Another use of these models was to ascertain the degree of nonlinearity that the structure exhibited after each stage of damage. Finally, these detailed finite element analyses were subsequently compared to results obtained with simple beam models of the bridge to assess the accuracy of the beam models.

IV. A. Preliminary Calculations

Before analyzing the bridge structure, the ABAQUS finite element code was exercised on a beam problem to verify that, for a well-defined problem, the dynamic properties predicted by ABAQUS agreed with closed-form solutions. A W40x328 beam 600-in. long was modeled five ways :

1. Using the 3-node general beam section elements, where the analyst must enter all relevant cross-section properties. These properties were obtained from an American Institute of Steel Construction Manual (AISC (1989)).

2. Using the 3-node I-section beam elements, where the cross-section dimensions are specified and ABAQUS calculates the cross-sectional properties.

3. Using 8-node shell elements to model the web and flange. The mesh for this model is shown in Fig. 33 along with the first bending (strong and weak axis) modes and the first torsional mode.

4. Using 8-node shell elements to model the web and beam elements to model the flange. Nodes for the beam elements are located at the centroid of the flange and constrained to the corresponding nodes representing the top and bottom edge of the web.

5. Using 8-node shell elements to model the web and beam elements to model the flange. Nodes that form the top and bottom edge of the web are used to define the flange as well, and the centroid option is used to define the location of the centroid of the flange.

In all cases, the beam was modeled with ten elements along its length. Generic steel material properties of E_{steel} = 29,000,000 psi, ν_{steel} = 0.3, μ_{steel} = 0.284 lbm/in^3, were specified in these analyses. Free boundary conditions were specified at each end of the beam.

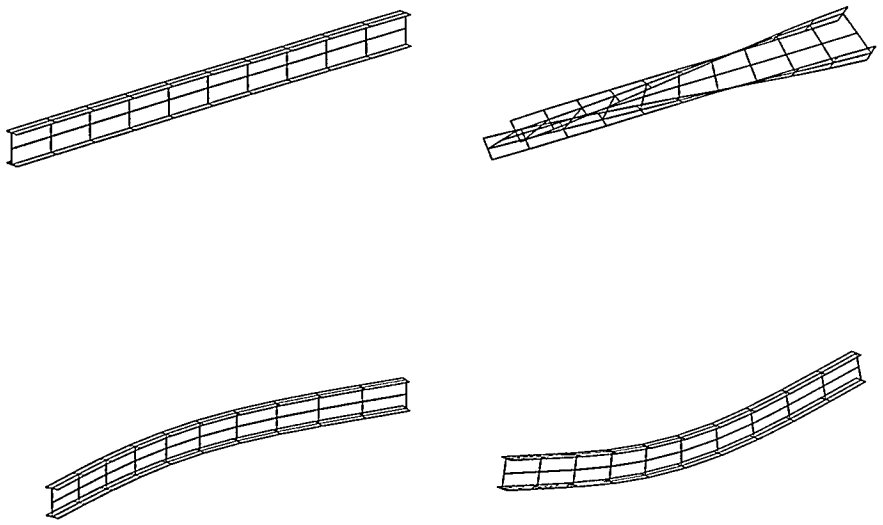

Fig. 33. Shell element model of the W40X328 beam, first bending modes, and first torsional mode.

Results from modal analyses were compared with closed-form solutions given by Blevins (1979) to verify that ABAQUS was accurately calculating the dynamic properties of this beam. The closed-form solution for the resonant frequencies associated with free boundary conditions are

$$f_b = \frac{(\lambda_i)^2}{2\pi L^2}\sqrt{\frac{EI}{\mu A}}, \text{ and} \tag{2}$$

$$f_t = \frac{1}{2L}\sqrt{\frac{JG}{\mu I_p}}, \tag{3}$$

where f_b = the bending mode frequency in Hz,
$(\lambda_i)^2$ =22.4 for Mode 1 (a factor to account for boundary conditions, see Blevins (1979)),
L = the length of the beam,
E = the modulus of elasticity,
I = the cross-sectional area moment of inertia,
A = cross-sectional area,
f_t = the torsional mode frequency in Hz,
J = the torsional constant for the cross section,
G = the shear modulus,
μ = the mass density, and
I_p = Polar moment of inertia about the center of mass.

It should be noted that the expression for the torsional frequency is only exact for circular cross-sections.

Table VII summarizes the results obtained. From these results it is evident that all methods of discretizing the beam give comparable results for the calculated dynamic properties of the beam.

TABLE VII

Comparison of Beam Dynamic Properties Calculated by ABAQUS with Closed-Form Solutions: Free Boundary Conditions

	Resonant Frequency (Hz)					
MODE	closed form	model 1*	model 2	model 3	model 4	model 5
1st Torsion	5.08	5.07	5.31	5.03	5.40	5.43
1st weak axis bending	8.10	8.09	8.37	8.06	8.12	8.12
1st strong axis bending	32.5	31.6	32.1	30.2	29.9	30.0

* Model refers to the elements and options used to discretize the beam as discussed in Sec. IV A.

IV. B. Undamaged Structure

As shown in Fig. 34, the cross section of the I-40 Bridge shown in Fig. 3 has been idealized as consisting of the following components:

1. A concrete slab of constant thickness with a cross-sectional area equivalent to that of the actual slab shown in Fig. 3.
2. Two steel plate girders.
3. Three steel stringers.
4. Steel floor beams (not shown in Fig. 34)

After the beam study was complete, detailed, finite element models of the bridge were developed. The first model uses 8-node shell elements to model the web of the plate girder and the concrete deck shown in Fig. 34. Three-node beam elements were used to model the stringers, floor beam, and flanges of the plate girder. Twenty-node continuum elements were used to model the concrete piers. Horizontal and vertical stiffeners on the plate girder, the diagonal bracing, and the concrete rebar were not incorporated in this model. Generic material properties were used. The steel material properties used in the preliminary beam study (see Sec. IV. A) were also used in this model. The concrete properties used were

$f'_c = 4000$ psi,

$E_c = 57000\sqrt{f'_c} = 3{,}600{,}000$ psi,

$\nu_c = 0.2$, and

$\mu_c = 145 \text{lbm/ft}^3$.

This model had 7032 DOF describing the bridge structure above the pier. Fixed boundary conditions were specified at the base of the piers. No attempt was made to model the soil medium underneath these piers. The mesh for this model is shown in Fig. 35.

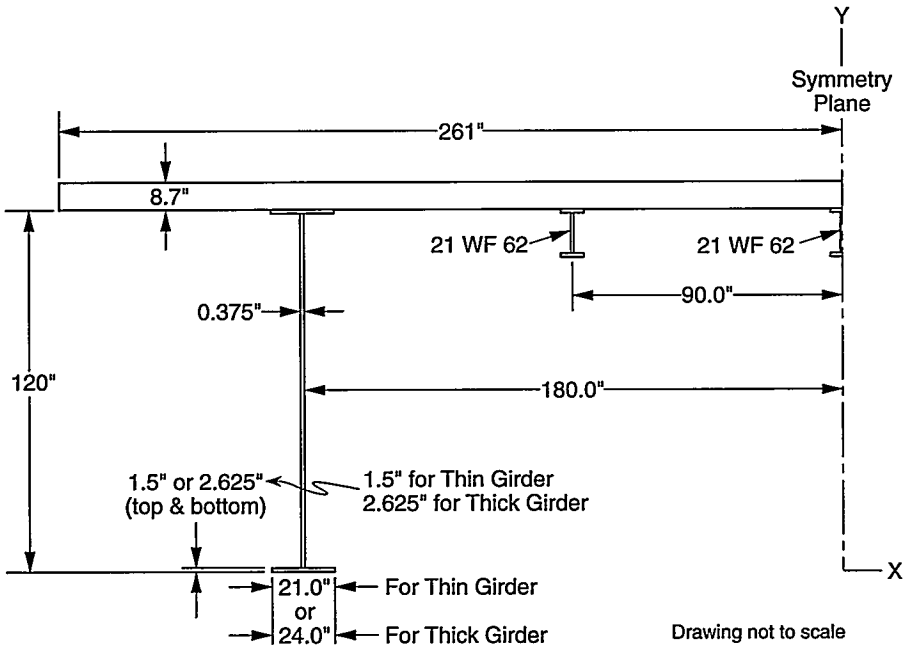

Fig. 34. Idealized bridge cross-section geometry.

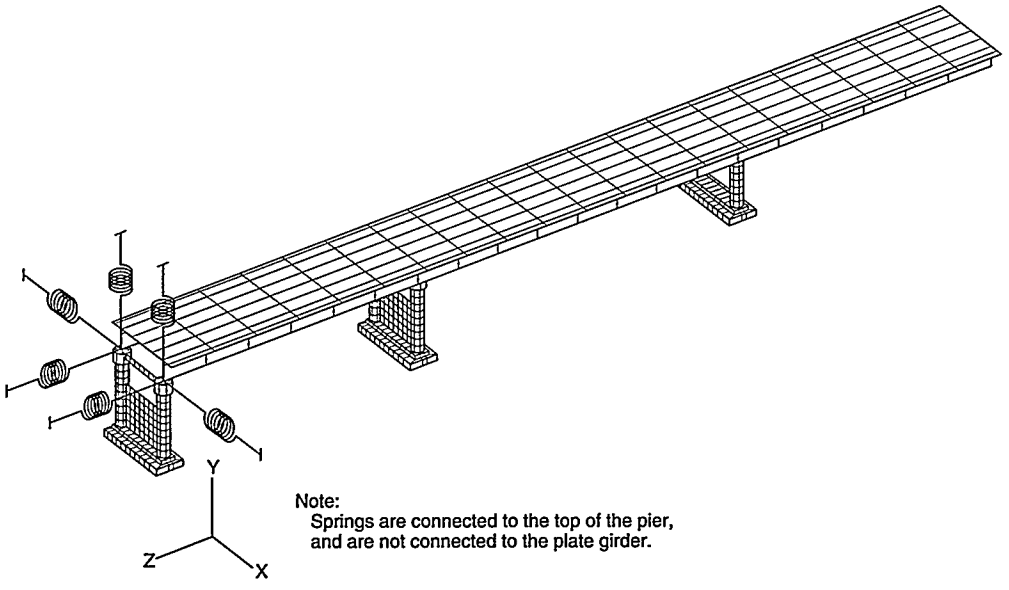

Fig. 35. 7032 DOF model of the I-40 Bridge.

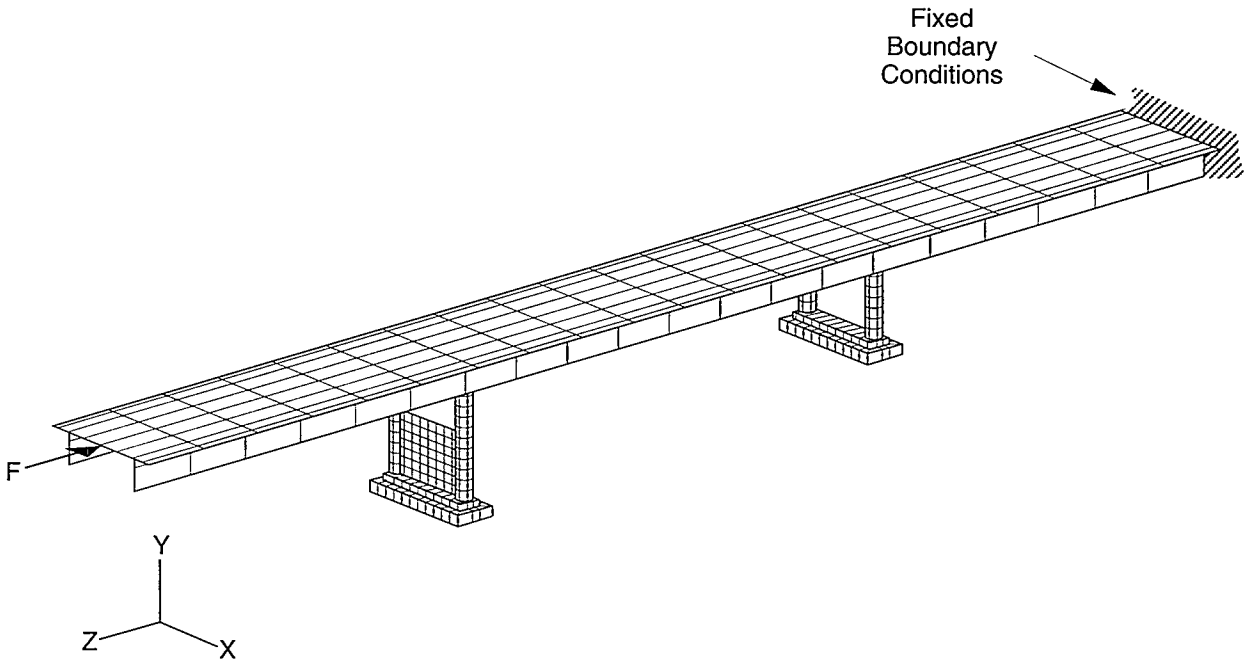

Fig. 36. Model that was analyzed to determine spring constants.

Six versions of this model were made. The difference between these versions lies primarily in the way that the connections between the bottom flange of the plate girder and the top of the piers or the abutment, shown in Figs. 5-7, were modeled. Another variation in these models was the addition of spring elements, fixed to "ground" at one end and connected to the top of Pier 3 as shown in Fig. 35. These springs were intended to simulate the stiffness added to this pier by the next section of the bridge that shares this pier with the section being analyzed and tested. To obtain the stiffness constant for these springs, the bridge model was fixed at one end, and Pier 3 was removed. All nodes corresponding to the free end were constrained to move uniformly. Loads were applied to this end in the three global directions as shown for the Z direction in Fig. 36. The calculated deflections of this end corresponding to the applied load provide the information necessary to approximate the stiffening effects that the next section of the bridge has on Pier 3. By providing a spring at both pier columns, these springs also stiffened the pier torsionally about all three axes. The individual spring constants calculated were

$k_x = 18.1 \times 10^3$ lbs/in.,

$k_y = 7.21 \times 103$ lbs/in., and

$k_z = 245 \times 10^3$ lbs/in.

The six versions are summarized below with a brief description of their distinguishing features. The global directions discussed below refer to those shown in Figs. 5 through 7 and Fig. 35.

BR3W At the abutment, nodes at the bottom plate girder flanges were constrained against translation in the X and Y directions. Rotations about the Y and Z axes were also constrained at these locations. These constraints were intended to simulate the connection detail shown in Fig. 5.

The nodes corresponding to the bottom of the plate girder at Piers 1, 2 and 3 were constrained to have the same translation in the X, Y, and Z directions as the nodes representing the top and center of the respective pier column. The detail of the connections at these piers are shown in Figs. 7, 6, and 5, respectively. Connections at Piers 2 and 3 would, in theory, allow relative translation in the Z direction between the plate girder flange and the pier. However, it was assumed that the levels of excitation were not sufficient to overcome the friction forces at these locations and, hence, this DOF was constrained. At all the piers, no constraints were imposed on the rotational DOF. Springs to simulate the stiffening effects of the other portion of the bridge sharing Pier 3 were not used.

BR3WB Identical to BR3W, but translation in the Z direction of nodes corresponding to the bottom plate girder flange at the abutment were also constrained. In theory, to account for thermal expansion, this connection allows for motion between the bottom web of the plate girder and the abutment in the Z direction. Observations made when the air temperature was significantly different showed that the connection appears to behave as intended. However, it was again assumed that the levels of excitation produced by the shaker were insufficient to overcome the friction at this connection. Therefore, translation in the Z direction was constrained.

BR3WC Identical to BR3W, but nodes at the top and center of the pier columns directly under the plate girder were fixed against rotation about the Y and Z axes. This condition forces the bottom of the plate girder to rotate with the top of the pier in these directions. The actual connections at these locations (Figs. 5 through 7) provides this restraint.

BR3WD Identical to BR3WC, except that the translation in the Z direction was constrained at the abutment.

BR3WDSP Identical to BR3WD, but with the spring elements shown in Fig. 35 and discussed above were added.

BR3WEQ At the nodes on the bottom of the plate girder that correspond to the support at the abutment, boundary conditions similar to those used in BR3WDSP were again used.

The nodes corresponding to the bottom flange of the plate girder over the center of Pier 1 were constrained to translate with the center node at the top of the pier in all three global directions. These nodes were also constrained to rotate together about the Y and Z axes. For this boundary condition, shell elements had to be added to the top of the pier.

Similar constraints were applied to the nodes at the bottom flange of the plate girder over the center of Piers 2 and 3 in an attempt to simulate the connection details shown in Figs. 5 and 6. Translation of the plate girder relative to the piers was not constrained in the Z direction at Piers 2 and 3. The springs were used with this model.

The boundary conditions associated with these different models are summarized in Table VIII.

TABLE VIII

Degrees of Freedom Constrained at the Nodes on the Bottom Flange of the Plate Girders Directly over the Piers and Abutment in Each Finite Element Model

Model	Abutment	Pier 1	Pier 2	Pier 3
BR3W	1,2,5,6[1]	(1,2,3)[2]	(1,2,3)[2]	(1,2,3)[2]
BR3WB	1,2,3,5,6	(1,2,3)[2]	(1,2,3)[2]	(1,2,3)[2]
BR3WC	1,2,5,6	(1,2,3)[2], 5,6	(1,2,3)[2],5,6	(1,2,3)[2],5,6
BR3WD	1,2,3,5,6	(1,2,3)[2], 5,6	(1,2,3)[2],5,6	(1,2,3)[2],5,6
BR3WDSP[3]	1,2,3,5,6	(1,2,3)[2], 5,6	(1,2,3)[2],5,6	(1,2,3)[2],5,6
BR3WEQ[3]	1,2,3,5,6	(1,2,3,5,6)[2]	(1,2,5,6)[2]	(1,2,5,6)[2]

[1] The 1, 2, and 3 directions correspond to translation in the X, Y, and Z directions shown in Fig. 34, respectively; the 4, 5, and 6 directions correspond to rotation about the X, Y, and Z axes shown in Fig. 35, respectively.
[2] These DOFs were constrained to the corresponding DOF at the node directly below on the top of the pier. For rotational DOFs, this constrain required the addition of shell elements to the top of the pier.
[3] Springs added to Pier 3.

A second, more detailed model was constructed, identical to the first, but with a more refined mesh. Beam elements that model the horizontal and vertical plate-girder web stiffeners were added to this model. This more detailed model uses 35,160 DOF to model the bridge deck and supporting steel structure. A modal analysis was made with the same material properties as those specified in the 7032 DOF model. Because the refinements to the model were for the bridge structure rather than the piers, the 7032 DOF model was modified to remove the piers and a corresponding modal analysis was performed. Note that all six 7032 DOF models are the same when the connection to the piers and abutment are not modeled. Boundary conditions that constrained all translational DOF were specified in both models at locations where the bottom plate-girder flange would normally

connect to a pier or abutment. The spring elements discussed above were not used in either model. Results from these two modal analyses are summarized in Table IX. These results indicate that the 7032 DOF model predicted almost identical dynamic properties as those given by the 35,160 DOF model. Based on these results, it was decided that all subsequent detailed finite element analyses would be done with the 7032 DOF model.

TABLE IX

Comparison of Dynamic Properties Identified By the 7032 DOF Model with the Dynamic Properties Identified by the 35,160 DOF Model

	7032 DOF Model		35,160 DOF Model	
Mode	Frequency (Hz)	Generalized Mass	Frequency (Hz)	Generalized Mass
1	2.82	1828	2.81	1784
2	3.77	1277	3.78	1225
3	3.81	988.2	3.79	963.7
4	3.88	584.4	3.87	562.0
5	5.11	1578	5.09	1484
6	5.23	1551	5.20	1473
7	5.48	756.4	5.39	738.6

IV. C. Damaged Structure

The 2nd, 3rd, and final damage states described in Sec. III. C. 1. were simulated by adding additional nodes and elements to the finite element representation of the web and bottom flange of the plate girder in the vicinity of damage as shown in Fig. 37. These modifications were made to model BR3W, and the new finite element models corresponding to the 2nd, 3rd, and final damage states are designated BR3WC1, BR3WC2, and BR3WC3, respectively. This method of modeling the damage changes the geometry only and does not introduce nonlinearities into the model. Therefore, a linear modal analysis can be performed to ascertain the effects of this damage on the dynamic properties of the structure. Before performing this modal analysis, dead-weight loading was applied in a static analysis of the undamaged model and the model corresponding to the final stage of damage. The relative deflection at the node representing the bottom flange at the cut location was calculated. During the experiments, the deflection of the bottom flange of the plate girder at a location adjacent to the cut was measured after the final stage of damage had been introduced. The measured deflection from the undamaged position was 0.81 in. The finite element model predicted a deflection of 0.29 in., a considerable difference. This lack of correspondence between the measured response and the finite element prediction is assumed to result from local yielding around the cut tip that produces a "hinge" allowing more rotation in this vicinity and, hence, larger deformation. To accurately model this effect, a very refined mesh in the vicinity of the cut tip is needed, and plasticity must beadded to the model. Although the bridge appears to be responding with reduced stiffness in this region, the dynamic response will not show the same reduced stiffness effects because the modulus of the yielded material does not change significantly from the material that has not yielded.

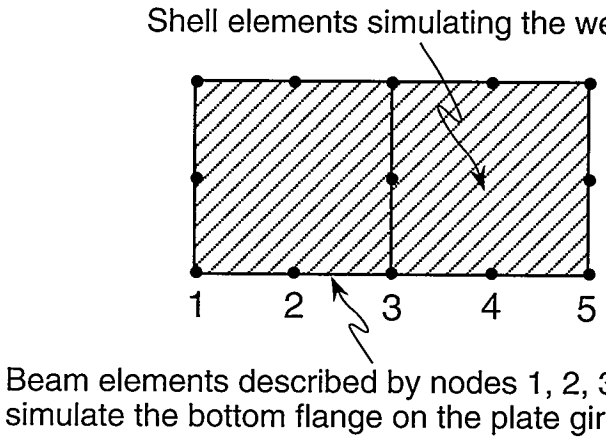

To model the second damage level, nodes 3' and 3" are defined, and a new beam element, 3-3'-3" is defined with similar cross-section properties as 1-2-3 and 3-4-5.

To model the third damage level, beam 3-3'-3" is given cross-section properties for a flange that has 1/2 the thickness of elements 1-2-3 and 3-4-5.

To model the final stage of damage, beam 3-3'-3" is removed completely.

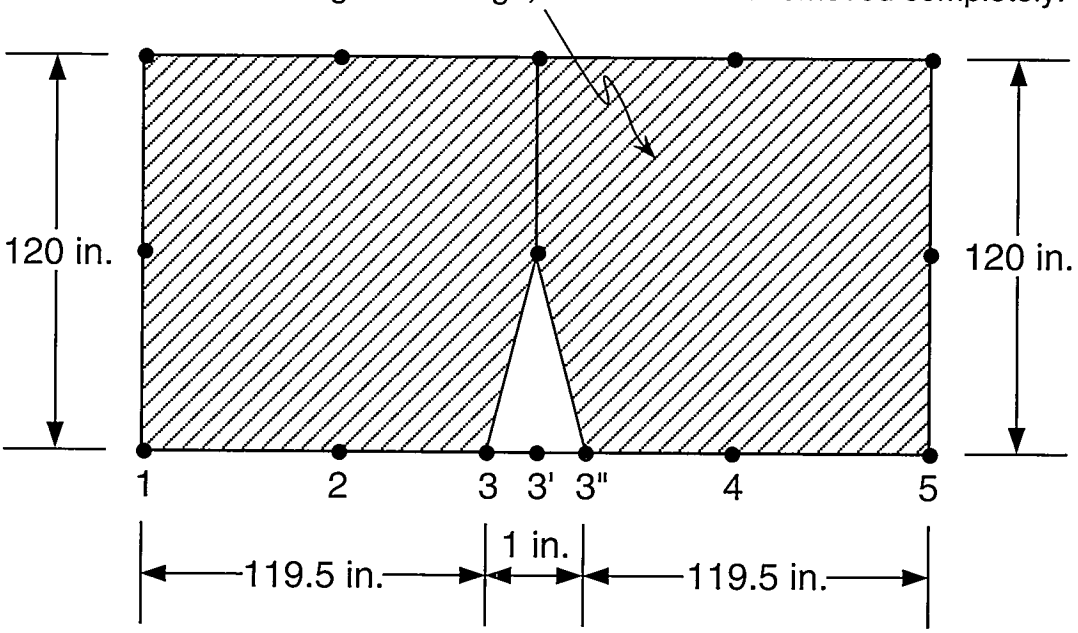

Fig. 37. Methods used to simulate the damage introduced to the I-40 Bridge.

IV. D. Detailed Finite Element Results Compared to Experimental Results

Results of the finite element analyses are compared to experimental results in terms of resonant frequencies and mode shapes for both the damaged and undamaged bridges. Undamped modal analyses of the different finite element models were run. These analyses provided estimates of the resonant frequencies and mode shapes of the bridge, which subsequently could be compared to similar measured quantities. Table X compares the results from the modal analyses of numerical models described in Sec. IV. B. with the experimental results obtained from forced vibration tests on the undamaged structure (see Sec. III. B.). Because accelerometers were mounted only in the vertical direction, experimental results concerning lateral modes of response were not obtained. Therefore, the average percent difference listed in Table X is for the vertical flexural modes and the torsional modes only.

TABLE X

Comparison of Analytical and Experimental Modal Analysis Results

	Resonant Frequency (Hz)						
	Experiment	BR3W	BR3WB	BR3WC	BR3WD	BR3WDSP	BR3WEQ
Mode 1	2.48	2.59	2.59	2.59	2.59	2.63	2.58
Mode 2	2.96	2.78	2.87	2.79	2.88	2.90	2.88
Mode 3	3.50	3.71	3.47	3.71	3.47	3.50	3.44
Mode 4	4.08	4.32	4.11	4.00	4.11	4.23	4.12
Mode 5	4.17	3.96	4.20	4.33	4.21	4.25	4.21
Mode 6	4.63	4.50	4.70	4.56	4.94	4.94	4.77
Ave. % Diff.	--	5.08	1.88	6.39	2.77	3.39	2.24

From resonant frequencies identified in Table X, it is evident that all the models are accurately predicting the measured response of the structure. In terms of an average percent error with the measured values of resonant frequencies, the models designated BR3WEQ and BR3WB provide the best approximation to the measured response of the bridge. Model BR3W has calculated the measured Mode 5 at a lower frequency than the measured Mode 4. When the translational constraints in the Z direction at the abutment are removed, the other numerical models also interchange these modes. The discrepancies with experimental results shown in Table X, which are considered small, are primarily caused by the idealization of the boundary conditions and the use of generic material properties for the concrete portion of the bridge.

The modal assurance criterion, Eq. 1, can be used to compare the analytical and measured mode shapes. To make this comparison, the components of the analytical mode shape vectors corresponding to translation in the vertical direction at locations similar to the accelerometer locations (see Fig. 9) were extracted from the finite element analysis to form a mode-shape vector that could be directly compared to the experimentally measured mode shapes. Table XI compared the modes determined from the finite element models with those identified during the undamaged forced vibration test (t16tr). The six

mode shapes identified by the finite element model BR3W that correspond to the experimentally measured mode shapes (Figs. 10 through 15) are shown in Figs. 38 through 43. The vertical bending modes are independent of the torsional response as was shown both in the analytical mode shapes and in the experimentally measured mode shapes. As can be seen in Table XI, the model designated BR3W predicts the measured mode shapes most accurately in spite of the fact that it has interchanged modes 4 and 5. Similar correspondence can be obtained with the other finite element models if the Z translational DOF at the abutment are left unrestrained. When this boundary condition is specified, the other finite element models also interchange modes 4 and 5.

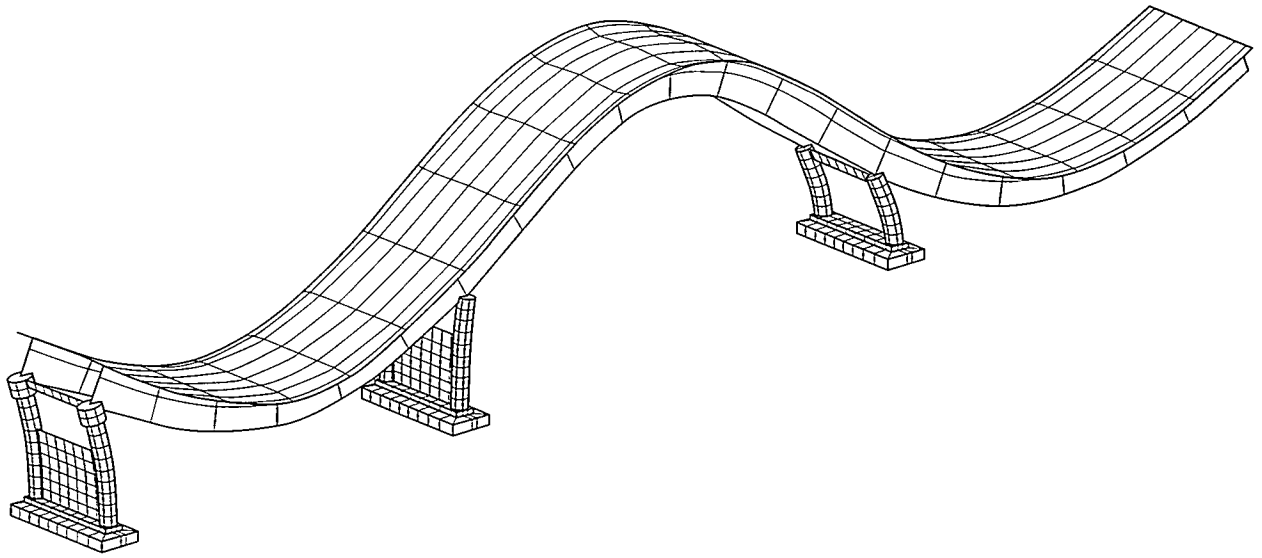

Fig. 38. First flexural mode calculated with finite element model BR3W.

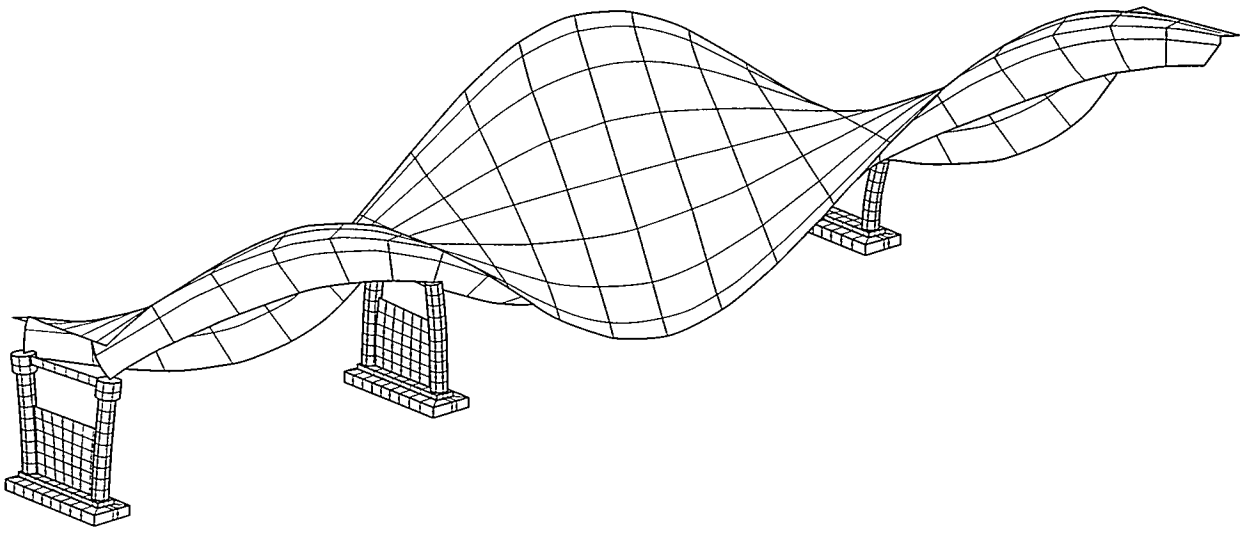

Fig. 39. First torsional mode calculated with finite element model BR3W.

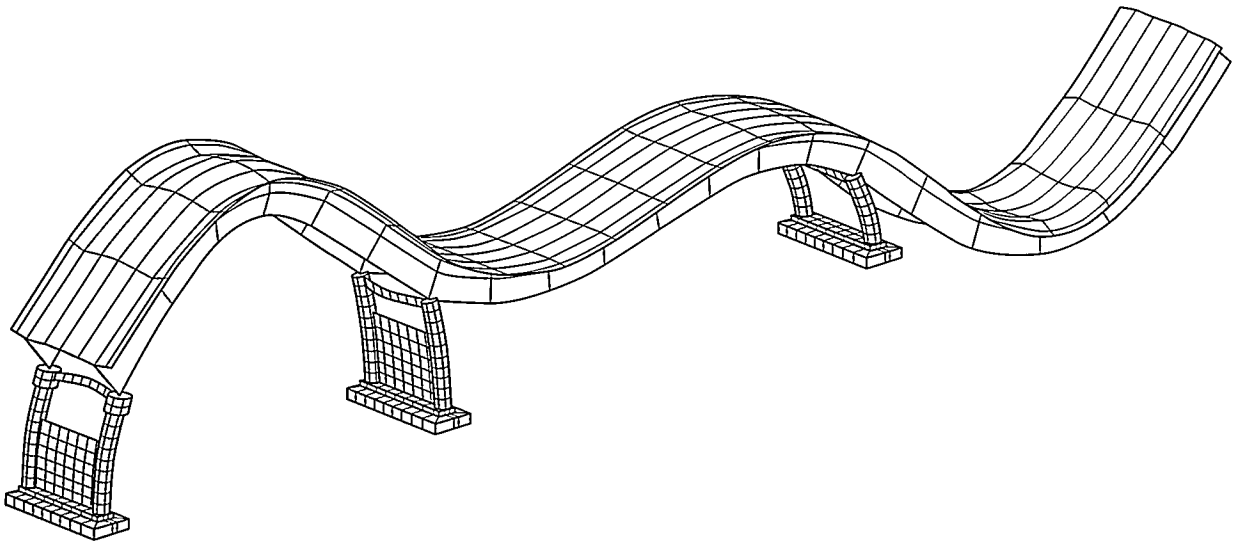

Fig. 40. Second flexural mode calculated with finite element model BR3W.

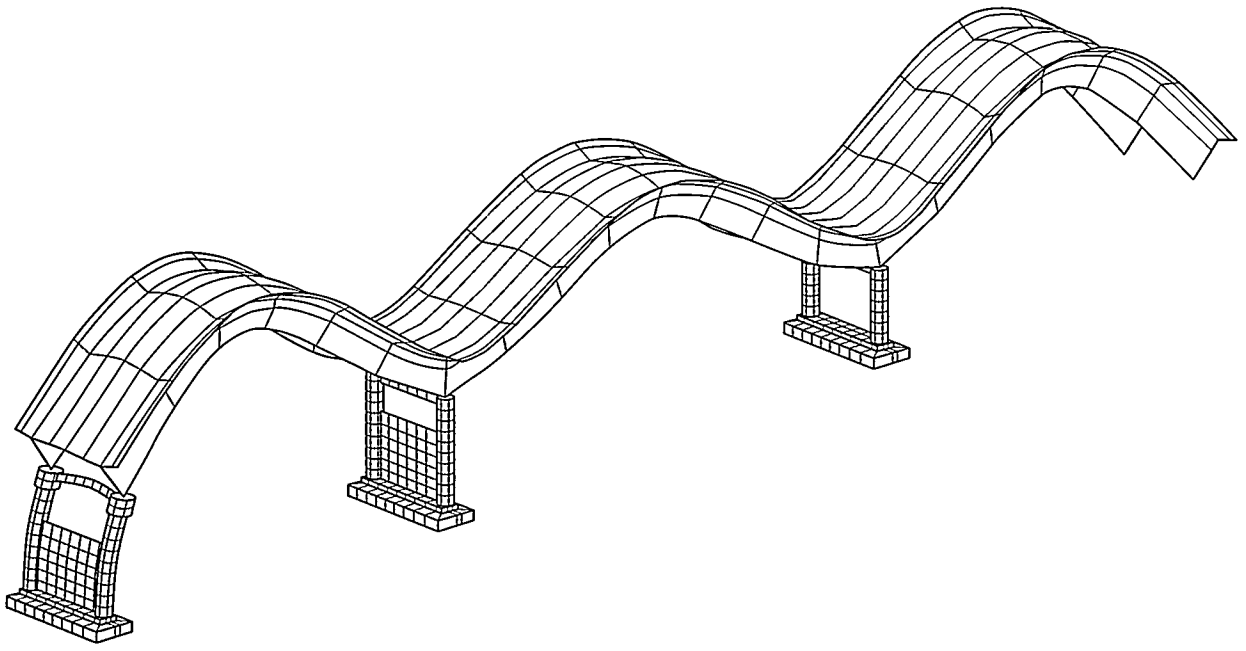

Fig. 41. Third flexural mode calculated with finite element model BR3W.

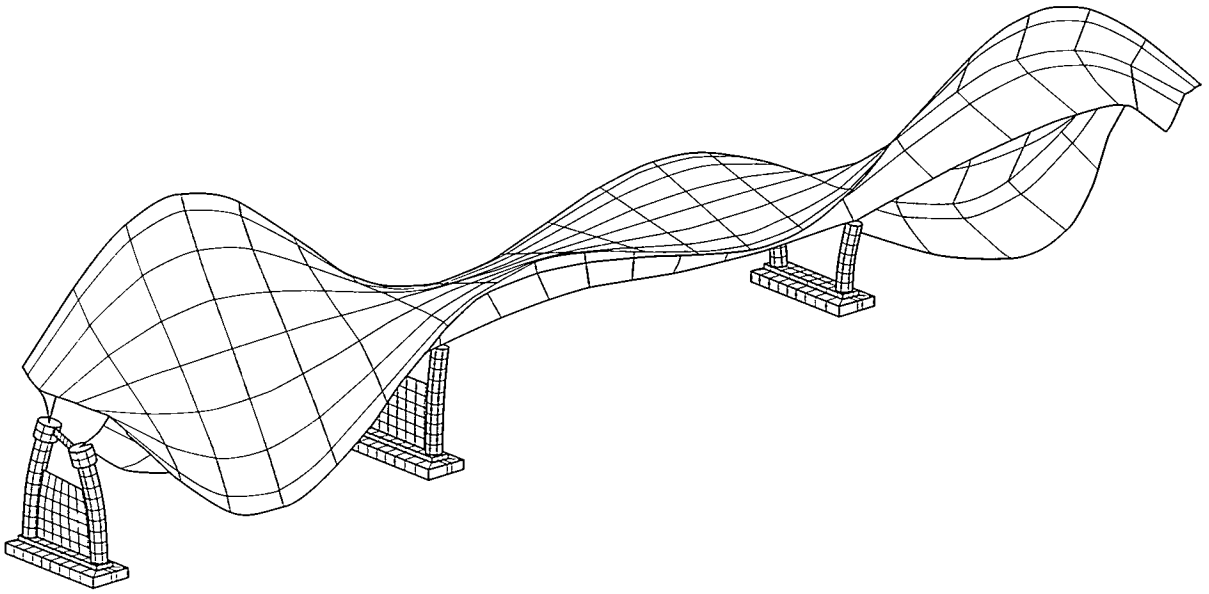

Fig. 42. Second torsional mode calculated with finite element model BR3W.

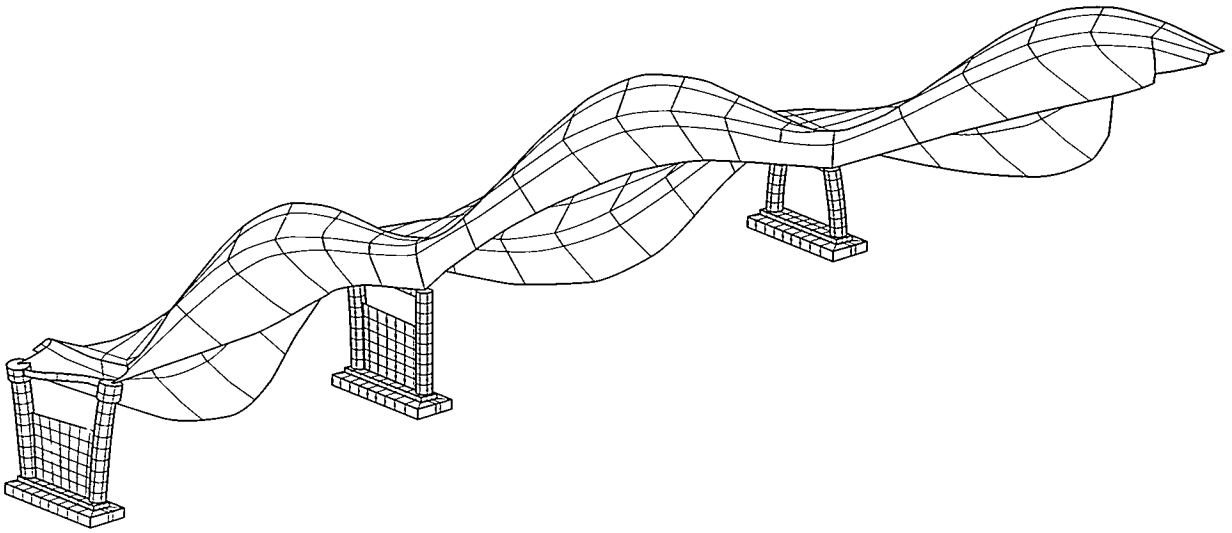

Fig. 43. Third torsional mode calculated with finite element model BR3W.

Figure 44 shows the first lateral mode identified by this finite element model. This mode shows coupling between the lateral bending response and the torsional response as predicted by the coupled equations of motion that are developed in Sec. V. E. 2. Gere and Lin (1958) have shown that the predominately torsional modes are not as affected by the coupling as the predominately lateral bending modes. This result is evident in the finite element mode shapes; however, measurements were not made to verify this result experimentally.

TABLE XI

Modal Assurance Criterion Comparing the Measured Mode Shapes from the Undamaged Bridge with Mode Shapes Calculated by Finite Element Analysis

Modal Assurance Criteria		t16tr X BR3W				
Mode	1	2	3	4	5	6
1	0.992	0.001	0.000	0.001	0.003	0.000
2	0.003	0.983	0.000	0.001	0.002	0.008
3	0.001	0.000	0.993	0.001	0.002	0.000
4	0.001	0.000	0.001	0.035	0.960	0.000
5	0.000	0.000	0.001	0.978	0.005	0.029
6	0.001	0.001	0.000	0.001	0.018	0.954
Modal Assurance Criteria		t16tr X BR3WB				
Mode	1	2	3	4	5	6
1	0.992	0.001	0.012	0.002	0.000	0.000
2	0.003	0.987	0.000	0.001	0.001	0.440
3	0.000	0.000	0.906	0.274	0.001	0.000
4	0.012	0.002	0.041	0.744	0.024	0.000
5	0.000	0.022	0.011	0.003	0.819	0.020
6	0.001	0.001	0.001	0.013	0.219	0.577
Modal Assurance Criteria		t16tr X BR3WD				
Mode	1	2	3	4	5	6
1	0.992	0.001	0.012	0.002	0.000	0.001
2	0.003	0.983	0.000	0.001	0.001	0.099
3	0.000	0.000	0.906	0.274	0.001	0.000
4	0.012	0.002	0.041	0.744	0.023	0.005
5	0.000	0.029	0.011	0.003	0.819	0.048
6	0.001	0.001	0.001	0.013	0.221	0.801
Modal Assurance Criteria		t16tr X BR3WEQ				
Mode	1	2	3	4	5	6
1	0.991	0.001	0.013	0.001	0.000	0.000
2	0.003	0.987	0.000	0.001	0.001	0.305
3	0.000	0.000	0.897	0.278	0.001	0.000
4	0.013	0.002	0.047	0.741	0.024	0.001
5	0.000	0.023	0.011	0.003	0.820	0.001
6	0.001	0.001	0.002	0.013	0.219	0.696
Modal Assurance Criteria		t16tr X BR3WDSP				
Mode	1	2	3	4	5	6
1	0.994	0.001	0.004	0.001	0.000	0.001
2	0.003	0.986	0.000	0.001	0.001	0.087
3	0.001	0.000	0.946	0.179	0.001	0.000
4	0.006	0.002	0.020	0.832	0.025	0.006
5	0.000	0.024	0.011	0.003	0.832	0.062
6	0.001	0.000	0.001	0.014	0.209	0.792

Based on a comparison of both the resonant frequencies and the mode shapes, it was decided that the numerical model designated BR3W showed the best correlation with the measured dynamic properties. This model was subsequently modified to simulate the damage as discussed in Sec. IV. C. Results of modal analyses performed with these modified finite element models are compared to corresponding experimental modal analysis results from the damaged structure in Tables XII and XIII. Figures 45 through 47 show the first three modes calculated by the finite element model that simulates the final stage of damage.

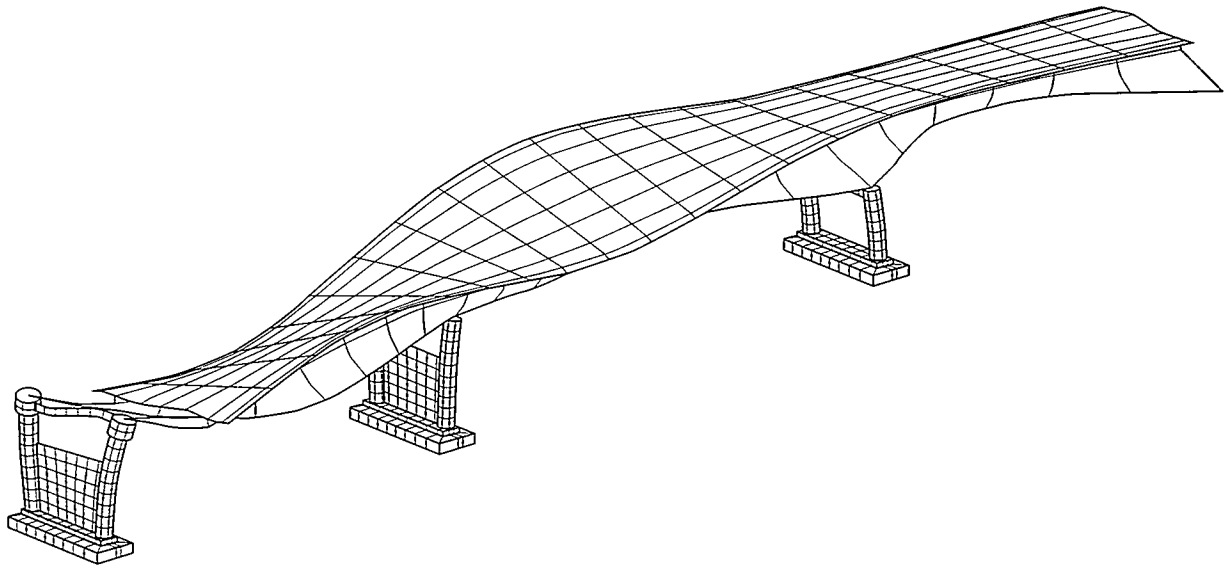

Fig. 44. First lateral flexural mode calculated with finite element model BR3W.

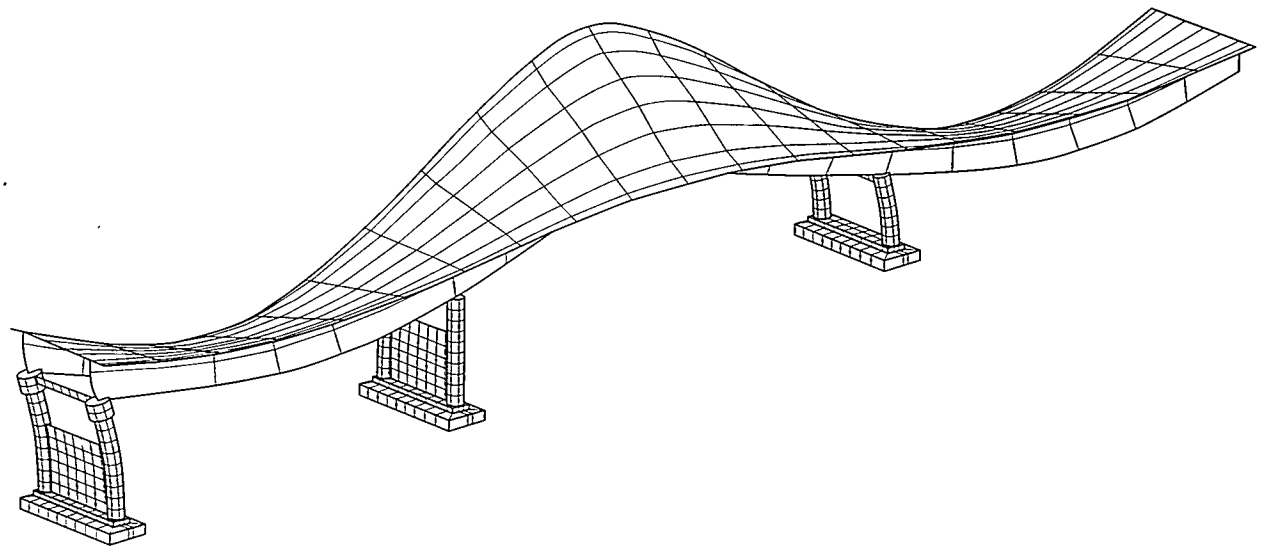

Fig. 45. The first flexural mode calculated with finite element model that simulates the final damage stage.

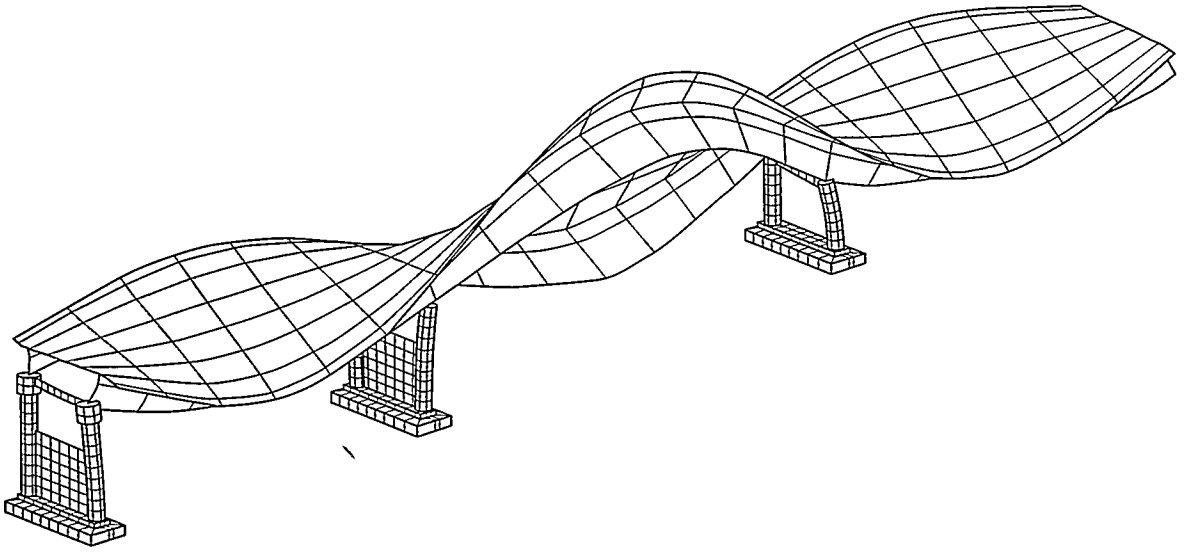

Fig. 46. The first torsional mode calculated with finite element model that simulates the final damage stage.

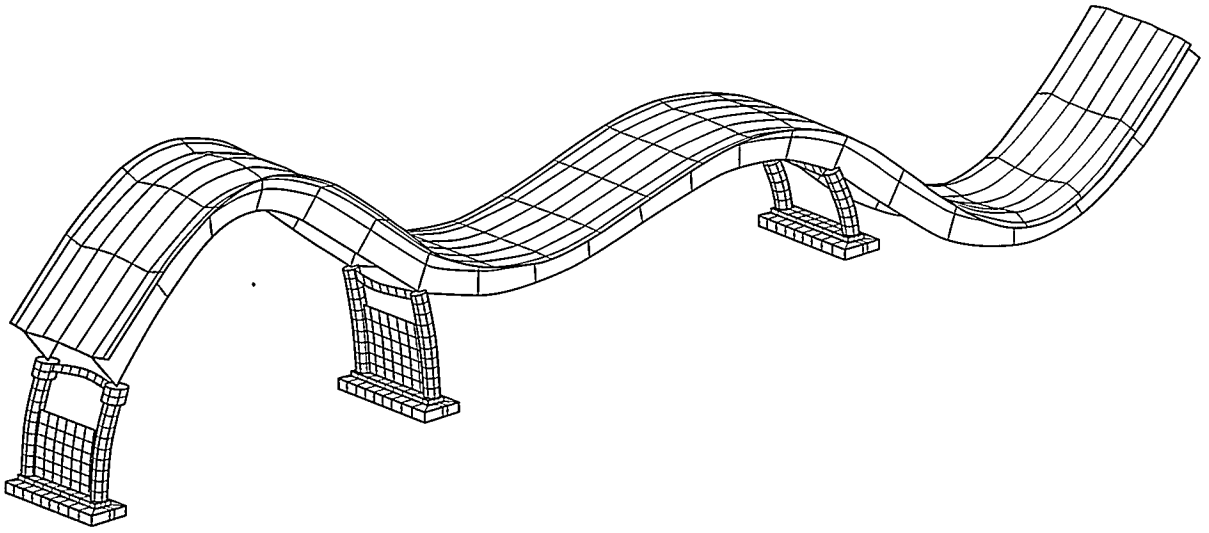

Fig. 47. The second flexural mode calculated with finite element model that simulates the final damage stage.

Table XII shows that the resonant frequencies do not change appreciably (greater than the frequency resolution) until the final stage of damage has been introduced. This result is shown in both the experimental data and the numerical calculations. No change in the mode shapes can be seen until the final stage of damage as is indicated by both the analytical and experimental mode-shape data summarized in Table XIII. It is of interest to note that after the final stage of damage, Modes 1 and 2 determined by finite element analysis showed the same percent drop in resonant frequency from their undamaged state as the corresponding drops in resonant frequencies measured on the bridge.

TABLE XII

Resonant Frequencies Measured on the Damaged Bridge Compared with Resonant Frequencies Calculated by Finite Element Analyses of the Damaged Structures Using Model BR3W

	2nd level of damage, 6 ft cut in web		3rd level of damage 6 ft cut in web, cut through half of the bottom flange		final level of damage 6 ft cut in web, cut through entire bottom flange	
Mode	Measured	BR3WC1	Measured	BR3WC2	Measured	BR3WC3
1	2.52	2.59	2.46	2.59	2.30	2.44
2	2.99	2.78	2.95	2.78	2.84	2.72
3	3.52	3.71	3.48	3.71	3.49	3.71
4	4.09	4.33	4.04	4.33	3.99	4.27
5	4.19	3.96	4.14	3.96	4.15	3.96
6	4.66	4.50	4.58	4.50	4.52	4.46

TABLE XIII

Modal Assurance Criterion Comparing the Measured Mode Shapes from the Damaged Bridge with Mode Shapes Calculated by Finite Element Analysis

Modal Assurance Criteria	t18tr X BR3WC1					
Mode	1	2	3	4	5	6
1	0.988	0.002	0.000	0.001	0.004	0.000
2	0.001	0.989	0.000	0.005	0.001	0.011
3	0.000	0.000	0.994	0.001	0.002	0.000
4	0.011	0.001	0.000	0.015	0.980	0.002
5	0.000	0.000	0.014	0.977	0.005	0.019
6	0.001	0.012	0.000	0.001	0.012	0.950
Modal Assurance Criteria	t19tr X BR3WC2					
Mode	1	2	3	4	5	6
1	0.994	0.000	0.000	0.001	0.005	0.000
2	0.001	0.988	0.000	0.004	0.001	0.011
3	0.000	0.000	0.994	0.001	0.002	0.001
4	0.011	0.001	0.000	0.012	0.983	0.002
5	0.000	0.000	0.010	0.982	0.005	0.017
6	0.001	0.006	0.000	0.002	0.011	0.962
Modal Assurance Criteria	t22tr X BR3WC3					
Mode	1	2	3	4	5	6
1	0.981	0.005	0.001	0.000	0.001	0.002
2	0.025	0.973	0.000	0.002	0.007	0.007
3	0.000	0.000	0.996	0.000	0.001	0.001
4	0.016	0.000	0.001	0.007	0.947	0.074
5	0.000	0.000	0.008	0.986	0.007	0.011
6	0.002	0.004	0.001	0.001	0.049	0.878

The numerical models show that Mode 3 did not change from its predamaged configuration even after the final stage of damage was introduced. Also, the resonant frequency associated with this mode is unchanged by the damage. Damage was introduced near a node for this mode, and it is evident that damage at such a location has little appreciable effect on this mode. This result was verified by the experimental data, which also showed no change in Mode 3, from its undamaged state, after the final level of damage had been introduced.

All the finite element models simulate composite action between the concrete deck, the stringers and the plate girders. The correlation between both the ambient and forced vibration experimental results and the finite element results indicate that, at the levels of excitation produced by traffic or by the Sandia shaker, the bridge is exhibiting composite behavior even though no shear studs were provided.

Other analyses of three-span continuous bridges reported in the technical literature show flexural mode shapes similar to those identified in our study (Lee, Ho and Chung (1987), and Raghavendracharm and Aktan (1992)). Raghavendracharm and Aktan also state that the second and third flexural modes have considerably higher participation factors than the fundamental flexural mode. Similar results were obtained with the finite element models reported herein. This qualitative correlation of the results reported herein with results from similar analyses made by other investigators lends further credibility to the accuracy of the numerical models developed during this study.

V. SIMPLIFIED FINITE ELEMENT MODEL

When compared with experimental results as discussed in Section IV. D., it is evident that the detailed finite element model of the I-40 Bridge described in the previous section provides an accurate model for calculating the dynamic response of the bridge. However, the detailed model suffers from complexity and size, as structural elements are intricately modeled using shell elements. A more simplified and practical model using a single beam element to represent the cross section of the bridge, which still accurately models the global dynamic response characteristics of the bridge, is desirable. Modeling of the I-40 Bridge using a simplified beam, finite element model vastly reduces the DOF compared to the shell element model. This simplified model makes the determination of the modal response of the bridge on a microcomputer, as opposed to a mainframe, more practical. The development of such a model is presented in this section.

Certain confounding factors make the representation of the bridge by simple beam elements somewhat difficult. These factors include

1. The composite (steel and concrete) nature of the bridge construction.

2. The presence of but a single axis of symmetry in the cross section.

3. The dynamic nature of the bridge response.

Implications of the above factors are that some flexural and torsional modes of response will be coupled, and that determination of the shear center, warping constant, sectorial moment, and the torsional constant of a thin-walled, open, noncircular composite cross section will be required.

In this section, the methods of modeling the dynamic flexural behavior of the bridge are first discussed, followed by a summary of the methods for modeling dynamic torsional behavior, appropriate modeling of the mass distribution for bending and torsion, and a discussion of kinematic constraints and boundary conditions needed to tie the beam elements representing the bridge cross section to the beam elements representing the piers. Flexural-torsional coupling details are also discussed, followed by a summary of results from a series of increasingly complex beam examples. These beam examples were used to verify the accuracy of the methods that were applied herein and subsequently used to develop the simple beam model of the I-40 Bridge. Finally, a summary of the beam model of the I-40 Bridge is presented. This beam model is based on the idealized cross-section geometry shown in Fig. 34 and discussed in Sec. IV. B.

The ABAQUS Finite Element Program was selected for the refined-shell-element model of the I-40 Bridge as well as for the simplified beam-element modeling presented in this section. The program is representative of a class of sophisticated, general purpose, finite element packages commercially available to the technical community. Therefore, the development which follows regarding consistent input for the simplified beam model is representative of the input considerations needed for most other finite element software packages as well.

The following are the input parameters (with units assuming mass as a derived unit, L = length, t = time, f = force) for the ABAQUS beam model (Beam General Section) which are relevant to the discussion here:

A	=	Beam cross-sectional area (L^2)
I_{11}, I_{22}	=	Area moments of inertia of the beam cross section about the centroidal axis (L^4)
J	=	Torsional constant (L^4)
Γ_0	=	Sectorial moment (L^4)
Γ_ω	=	Warping constant (L^6)
μ	=	Mass density ($f\text{-}t^2/L^4$)
E	=	Young's modulus (f/L^2)
G	=	Shear modulus (f/L^2)
x_0, y_0	=	Shear-center location relative to the centroid (L)

When thermal effects are neglected and the 11 and 22 axes define the principal moments of inertia (that is, the products of inertia are zero), ABAQUS calculates the forces acting on a beam as

$$N = E(A\varepsilon_c + \Gamma_0\chi), \tag{4}$$

$$m_{11} = EI_{11}\kappa_{11}, \tag{5}$$

$$m_{22} = EI_{22}\kappa_{22}, \tag{6}$$

$$T = G(J\phi + I_p w), \text{ and} \tag{7}$$

$$W = E(\Gamma_0\varepsilon_c + \Gamma_\omega\chi), \tag{8}$$

where N = axial force,
ε_c = axial strain at the centroid,
χ = axial strain caused by twisting of the beam,
m_{11} = moment about axis 1,
κ_{11} = curvature change about axis 1,
m_{22} = moment about axis 2,
κ_{22} = curvature change about axis 2,
T = torque about the longitudinal axis,
ϕ = angle of twist,
w = warping amplitude, and
W = the bimoment that produces warping.

A detailed summary of the beam-element formulation for thin-walled open sections can be found in the ABAQUS Theory Manual (1994).

It is necessary that the above input be consistent with the composite nature of the cross section, the presence of only a single axis of symmetry in the cross section, and the fact that dynamic response is occurring with coupled bending and torsional beam response. While it may not be possible to precisely model all aspects of the composite beam with the above input parameters, the purpose of this section is to demonstrate how the beam can best be modeled.

The discussions below focus on developing the input parameters for the beam elements representing the bridge deck and supporting steel beams. Similar methods were applied to develop equivalent beam representations of the concrete piers. In these developments the reinforcement in the piers was neglected.

V. A. Modeling Flexural Behavior

Flexural stiffness of the composite cross section is modeled by developing an "equivalent" or "transformed" cross-sectional area using well-known techniques as discussed in Popov (1968). Assuming compatibility of strains at the interface of the two materials, the transformation is accomplished by adjusting the dimensions of the cross section parallel to the neutral axis, about which bending is assumed to occur, by a factor equal to the ratio of the elastic moduli of the materials in the cross section. For example, consider a cross section consisting of material 1 and material 2, for which respective elastic moduli are E_1 and E_2, with $E_1 > E_2$. The original and transformed cross sections are shown in Fig. 48 for the case in which an equivalent model is constructed in terms of Material 1. In this case, the forces on both elements are unchanged by the simultaneous modification of the modulus and width of material 2. However, because the cross section is now of a single material, strength-of-materials beam behavior and associated concepts again apply. This method provides an exact single-material representation of a multimaterial beam's flexural response subject to the limitations of strength-of-materials beam theory (linear elastic response, small deformations, etc.).

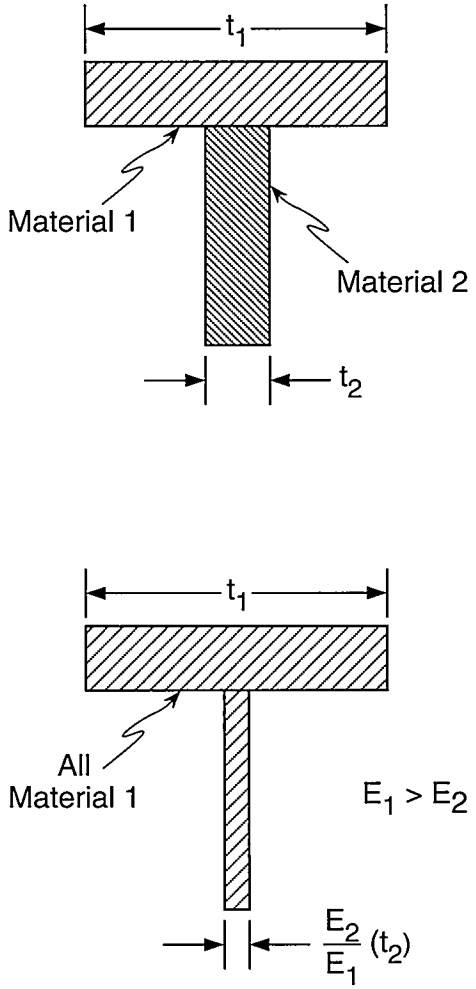

Fig. 48. Example of a beam of two materials and its transformed section representation.

The resulting centroidal axis location found from the centroid of the transformed cross-sectional area is then the correct neutral axis for bending. Similarly, the area moment of inertia of the transformed section about this neutral axis is appropriate for modeling the flexural response. While the stresses are incorrect for the transformed material (they have to be adjusted by the modular ratio), the bending moment is correct. The process can be repeated about the orthogonal axis, again resulting in the correct bending moment about that axis. A linear superposition argument then justifies simultaneous bending about both axes. It is straightforward to show that the total transformed area for bending about one principal axis is equal to the transformed area for bending about the orthogonal axis.

The procedures for representing the composite bridge cross section as a simple beam for the purpose of calculating the dynamic flexural response are listed below. Note that shear deformation and rotary inertia effects are not considered in this development.

1. The composite cross section of the bridge is transformed into a single material as discussed above.

2. The centroid of the transformed section is determined.

3. The moment of inertia about the centroidal axis is determined for the transformed section. This moment of inertia and the modulus of the single material used to represent the bridge define the flexural stiffness of the bridge.

4. An equivalent mass density of the bridge is determined such that the transformed section will have the same mass per unit length as the original section. Rotary inertia effects are not considered when calculating this equivalent mass density.

5. The process (1–3) is repeated for bending about the orthogonal principal axis.

For the beam model of the I-40 Bridge, this method provides the location of the centroidal axis and the two area moments of inertia about the centroidal axis, I_{11} and I_{22} (I_x and I_y, using axes labels in Fig. 34) for each of the two cross sections modeled. Detailed calculations for centroidal axis locations of the transformed bridge cross section and moments of inertia of the transformed sections about these axes are presented in Appendix A where the bridge has been modeled as an equivalent steel cross section. Numerical values of these parameters are summarized below in Section V. G. The concrete deck is assumed to be uncracked, and reinforcing steel is ignored. These effects tend to be self-canceling. Compatibility of strains at the concrete-steel interface is assumed in the development given above. This compatibility implies that the bridge is assumed to exhibit composite action. Although this method will give the appropriate transformed cross-sectional area, this area will have to be adjusted based on mass distribution considerations for torsion discussed in Section V. C. At this point, the ABAQUS input values of I_{11} and I_{22} (I_x, and I_y, using axes labels in Fig. 34), the centroidal axis location and, by implication, E have been determined for the beam model of the I-40 Bridge cross section.

V. B. Modeling Torsional Behavior

Certain torsional properties must be supplied as input to the simplified beam element model; and these torsional properties can be difficult to determine, particularly for a multi-material, thin-walled, branched cross section. In the subsequent discussions a "branched cross section" refers to a cross section that can not be described by a single, continuous path coordinate. It is the purpose of this section to develop the necessary background on torsion and to illustrate procedures for determining the torsional input parameters required by the beam-element model. Included in this section are discussions of the types of torsion that must be modeled, the method used to determine the torsional rigidity of the bridge cross section, analytical and numerical methods to locate the shear center, a numerical method used to determine the warping constant and sectorial moment of the cross section, and sample problems used to verify the accuracy of these methods.

As discussed in numerous sources, e.g., Galambos (1968), Heins (1975), and Boresi, et al. (1978) torsion can be separated into two distinct categories: pure or St. Venant torsion and warping torsion. With a few notable exceptions (solid and hollow circular cross sections), cross sections that are initially plane no longer remain plane when torsion is applied, but rather undergo warping deformations. If a cross section is free to warp, the applied torque is resisted by purely torsional response only. However, if these warping deformations are restrained to any degree, the applied torque is resisted by a combination of pure torsional response and warping torsional response.

Out-of-plane distortions which are caused by the application of a torque do not induce any normal stresses as long as constraints to these warping displacements are not introduced. If warping is restrained, however, normal stresses will be induced which, in turn, induce a warping torsional moment. This moment is in addition to the pure torsional moment. Warping deformations can be constrained in one of two ways: by certain constraints on the end conditions, that is, by fully fixing the end of the torsion member so that out-of-plane deformations are restricted, or by a variation of the resultant torque along the longitudinal axis of the member.

An illustration of these out-of-plane deformations is shown in Fig. 49. The hollow circular cylinder does not warp when a torque is applied. Based on equilibrium considerations, shear stresses in the plane of the cross section are accompanied by internal shear stresses along the length of the cylinder. When a longitudinal slit is made in the tube, it is transformed from a tube into a thin-walled open section, and with the application of a torsional moment, warping deformations occur. The longitudinal shear stress on the newly exposed face is no longer present, so the face deforms upward with the mating face deforming downward. In this case only pure torsion occurs unless these warping deformations are restrained, say by a restraint at the lower boundary (as an example, welding the tube to a rigid plate).

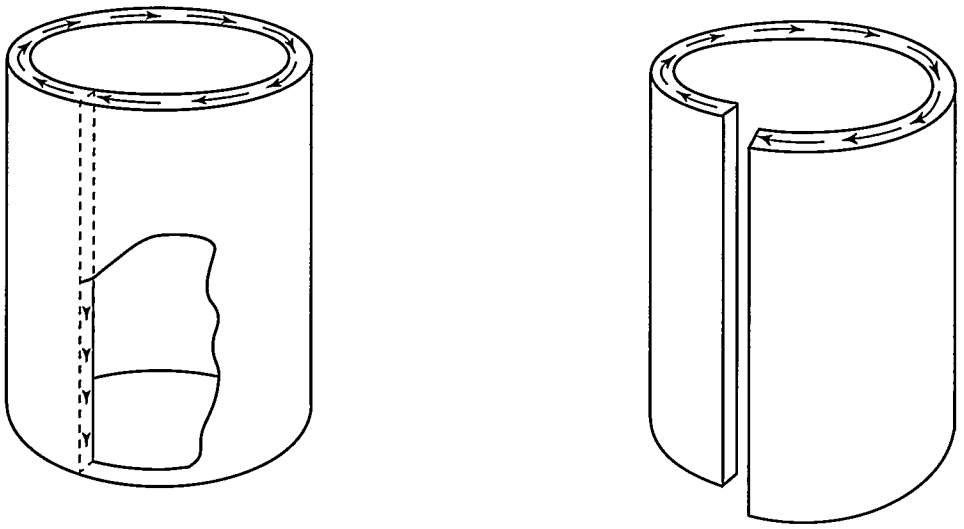

Fig. 49. Illustration of out-of-plane deformations caused by warping.

Varying the resultant torque along the longitudinal axis of the member also results in the constraint of warping deformations. Again, consider the thin-walled circular section with a longitudinal slit, Fig. 49, but this time as it undergoes general elastic vibrations. There are constraints to the warping deformations caused by changes in generalized inertial forces along the length of beam.

Based on the observation discussed above, it appears essential to account for warping torsion when performing a dynamic analysis of the I-40 Bridge. Notwithstanding the fact that the ends of the section of the bridge analyzed may be modeled as "simply supported for torsion," that is, allowed to freely warp at the boundaries, dynamic torsional vibrations will cause varying degrees of partial or complete constraint depending on the torsional mode and location along the longitudinal axis. Before calculating the cross-sectional properties related to warping, the equivalent torsional rigidity of the cross section is determined.

V. B. 1. Torsional Rigidity

Expressions are readily available for the torsional rigidity of both individual and built-up, thin, noncircular members made from the same material (Boresi, et al, 1978). However, in the case of the I-40 Bridge, the cross section is composed of steel and concrete members. Most advanced strength-of-materials texts do not discuss how the combined torsional rigidity should be determined for such cross sections. For example, consider the multimaterial beam cross section shown in Fig. 50. The beam is assembled from individual components such that it functions as a single beam. In other words, all components undergo the same angular twist, ϕ, or angular twist per unit length, $\theta = \phi/L$, when subjected to some resultant torque, T.

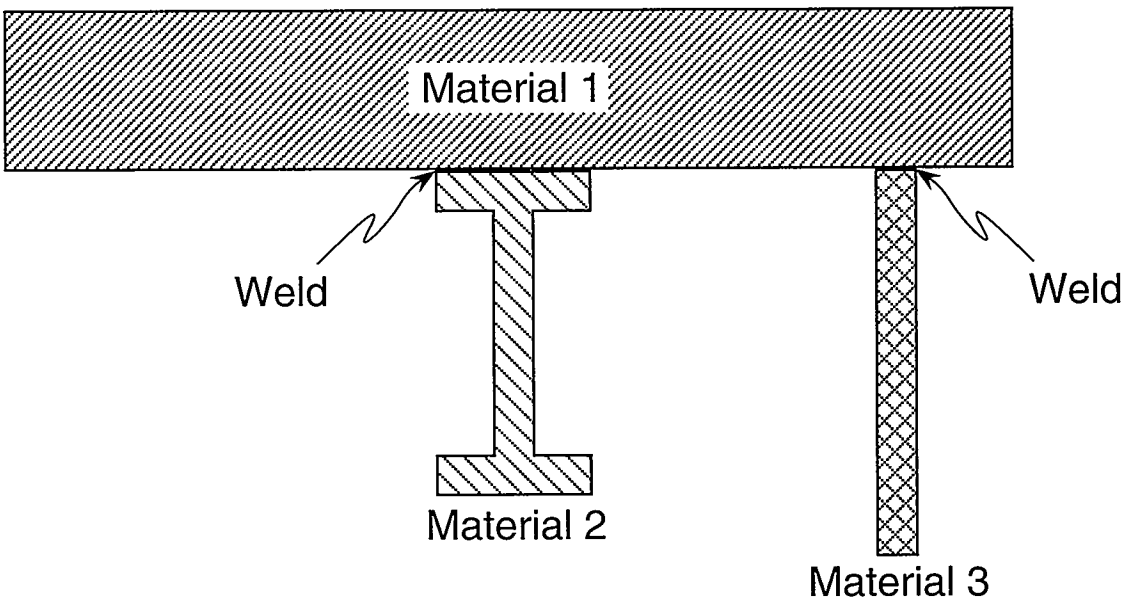

Fig. 50. Cross section of a three-material beam.

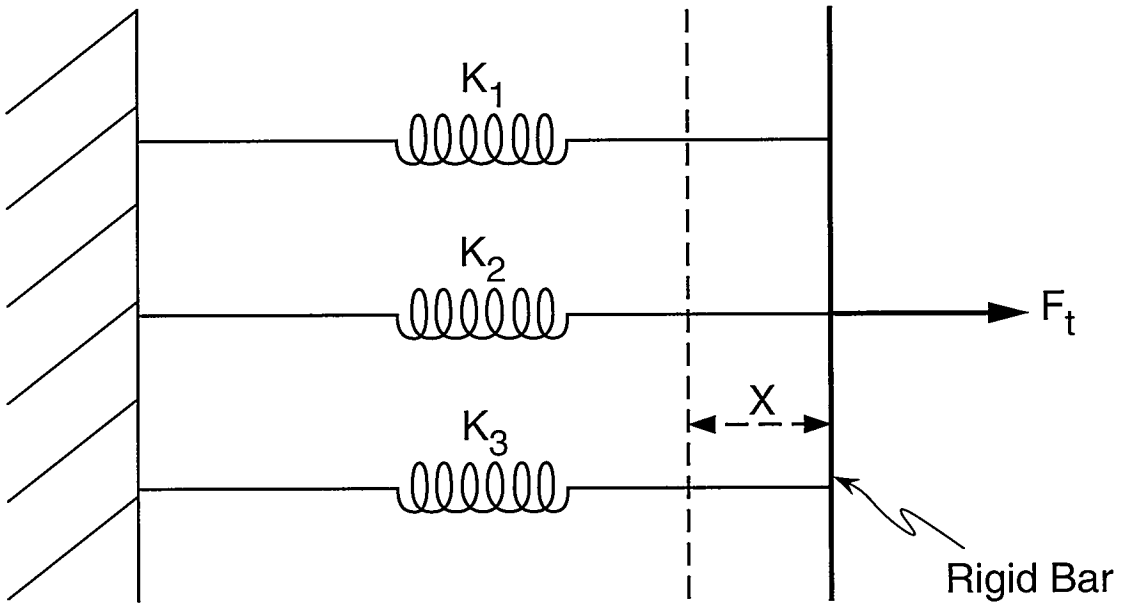

Fig. 51. Equivalent linear spring analogy for torsion of multi-material cross sections.

The torsion of a composite structural member is analogous to the case of linear springs in parallel, as shown in Fig. 51. For this simple analogy, the total force, F_t, is the sum of the 3 forces, F_1, F_2, and F_3, exerted by the individual springs,

$$F_t = F_1 + F_2 + F_3. \tag{9}$$

Also, the displacements of the 3 springs are equal to x, so

$$F_t = K_1x + K_2x + K_3x. \tag{10}$$

The stiffness (force for unit deflection) of the system is then

$$\frac{F_t}{x} = K_1 + K_2 + K_3, \tag{11}$$

the sum of the individual stiffnesses. Therefore, the total generalized force (tòrque in this case) is equal to the sum of generalized forces for each element, and the generalized displacement of each of the elements (the angle of twist per unit length, θ) is the same.

Assuming linear elastic behavior, the relationship between applied torque and the angle of twist per unit length resulting from pure torsion of a single-material cross section is

$$T = GJ\theta, \tag{12}$$

where G is the shear modulus, and J is the torsion constant of the cross section.

By the above analogy, the torsional rigidity of the n individual members are additive, hence

$$\frac{T}{\theta} = \sum_{i=1}^{n} G_iJ_i, \tag{13}$$

where G_i and J_i are the shear modulus and torsional constant for the *i* th material.

The cross section of the I-40 Bridge is modeled as a composite section using Eq. 13 to calculate torsional rigidity. Individual torsional constants are determined using handbook values (AISC (1989)) or the well-known formula for a section built up from thin rectangular plates (Boresi, et. al, 1978),

$$J = \sum_{i=1}^{n} \frac{1}{3} b_i t_i^3, \quad b_i \geq 10t_i, \tag{14}$$

where b_i is the length of a thin rectangular section making up the cross section, t_i is the corresponding width, and n is the number of thin rectangular members making up the cross section. For sections where b_i is not greater than $10t_i$, the coefficient of 1/3 must be reduced as discussed in Oden and Ripperger (1981).

In addition to defining an equivalent torsional rigidity, the shear center, warping constant, and sectorial moment for the equivalent beam must be found in order to accurately model the torsional dynamic response of the bridge using a single beam element. The shear center in a straight, uniform-cross-section beam is that point in the cross section through which the load must pass if there is to be no torsion in the beam (Boresi, et al, 1978). The relationship between shear center and center of twist is discussed by Stephen and Maltbaek (1979). These authors show that for a thin-walled, open-section cantilever beam of constant thickness, the shear center and center of twist coincide. Because the warping constant and the sectorial moment are defined with reference to the shear center, the next portion of this development will focus on determining the location of the shear center.

V. B. 2. Analytical Method for Locating the Shear Center

Specification of the shear center and the warping constants (as discussed previously) are required when the torsional response of a thin-walled open beam is sought. Galambos (1968) developed equations and procedures for determining these quantities for the case of single-material members. McManus and Culver (1969) extended the work of Galambos (1968) to a general composite, open, thin-walled beam and presented the resulting expressions in series form for the case of a cross section consisting of a series of flat plates, each of a different material. Heins and Kuo (1972a, 1972b) developed approximate equations for the evaluation of shear center and torsional constants of a single-girder, concrete-slab member. Briefly, the composite section shown in Fig. 52 is transformed into the idealized, single-material torsional model in Fig. 52 by converting the concrete slab to an equivalent area of steel. Note, however, that unlike the "equivalent section" method for bending of composite sections discussed in Section V. A., the torsional equivalent-steel section is approximate, based on the theory of torsion for thin-walled sections. Unfortunately, while the simplified expressions are extremely useful, there appears no way of extending them to more complicated structural cross sections. Kollbrunner and Basler (1969) present a detailed discussion on built-up, open cross sections, including a tabular procedure for determining warping constants. They also briefly allude to the treatment of composite cross sections. Finally, Heins (1975) presents extensive numerical procedures based on the work of Galambos (1968) for determining warping torsional properties.

Notwithstanding the availability of numerical procedures for determining the shear center and warping constants, the methods are difficult to apply and require great care to prevent errors. For that reason, the shear center for the I-40 Bridge cross section is first determined in closed form in the following section using standard methods given by Gere and Timoshenko (1990).

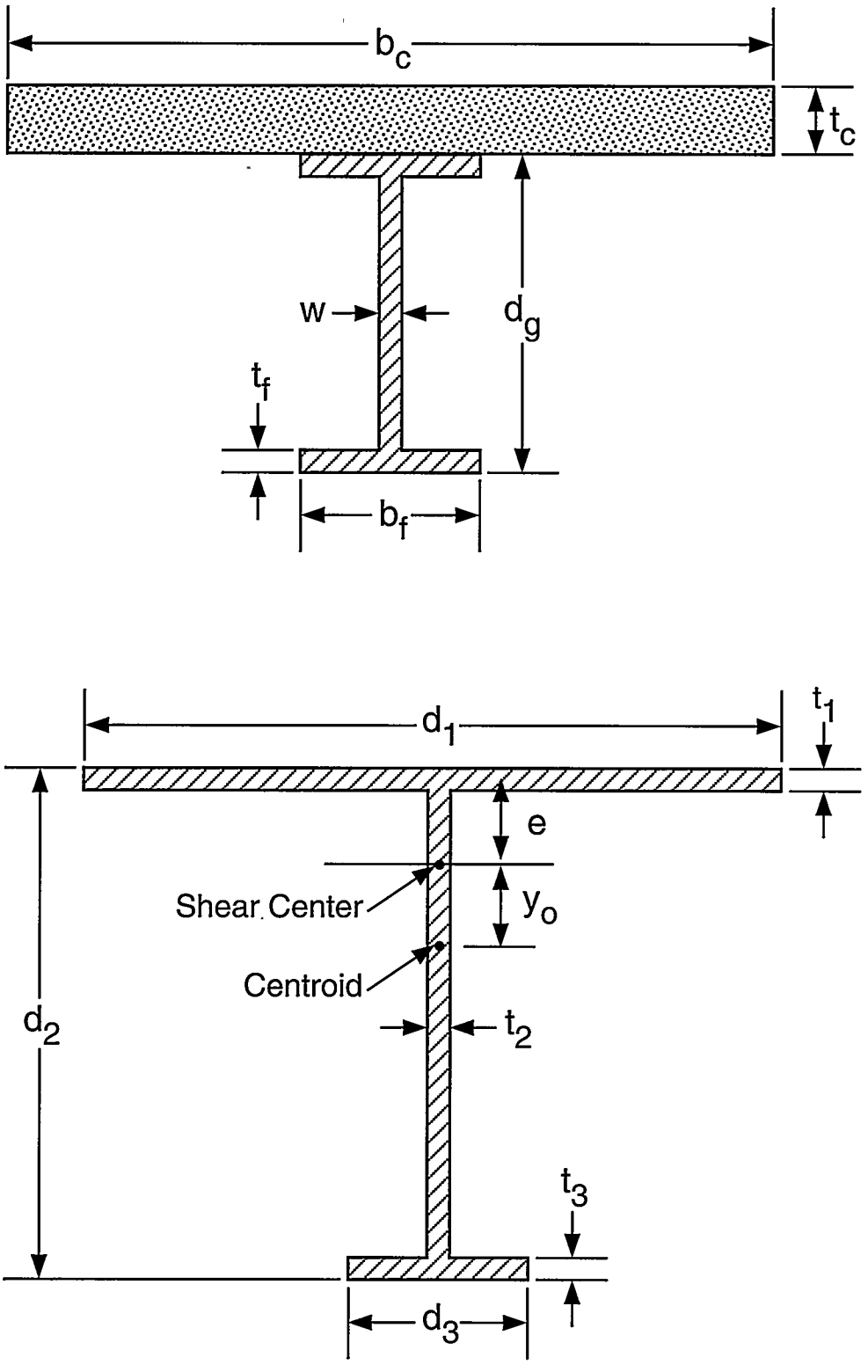

Fig. 52. Approximate torsional model of a composite cross section (from Heins and Kuo, 1979).

Additional simplifications to the idealized cross section of the I-40 Bridge shown in Fig. 34 are now made so that the methods of Gere and Timoshenko (1990) can more easily be applied:

1. The cross section is transformed to a single-material cross section by multiplying the thickness of the concrete slab by the modular ratio, $n = E_c/E_s$, based on procedures discussed in Kollbrunner and Basler (1969) and Heins and Kuo (1972).

2. The three steel stringers (21 WF 62) are ignored as their contribution to torsional response will be slight.

3. The transformed concrete slab is considered as a "thin" rectangular element, as justified experimentally by Heins and Kuo (1972).

4. The top flanges of the two girders are ignored, as justified by Heins and Kuo (1972).

The resulting simplified equivalent, "all steel" cross section is shown in Fig. 53.

The beam cross section shown in Figure 53 is singly symmetric. Thus both the centroid and shear center will lie on the axis of symmetry. In order to determine a sign convention for shear flow, consider that the idealized bridge cross section shown in Fig. 53 is that of a cantilever beam subjected to a concentrated end load as shown in Fig. 54. The end load is assumed to pass through the as-yet-determined shear center.

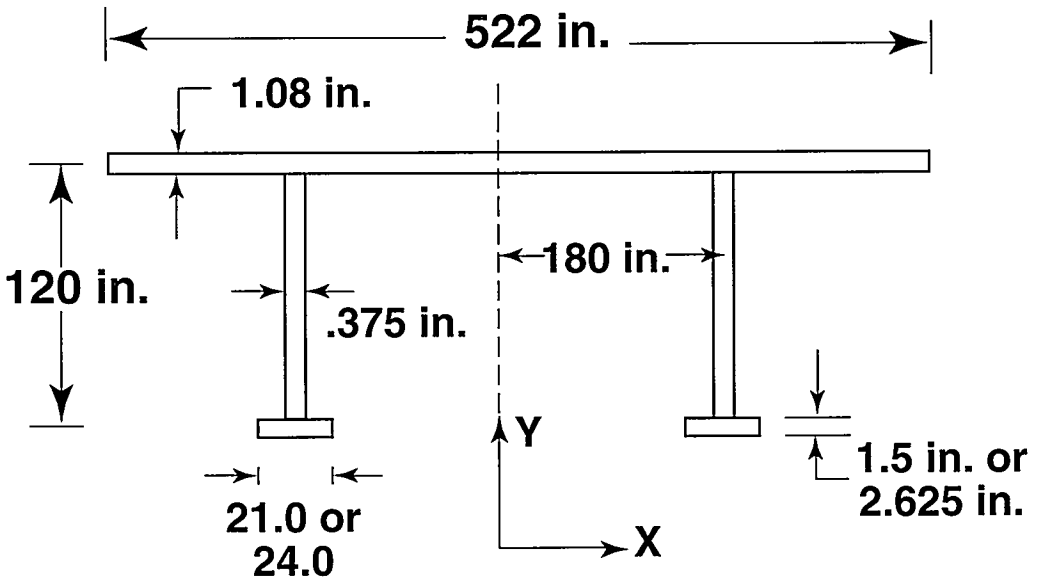

Fig. 53. Approximate I-40 Bridge geometry used to locate the shear center.

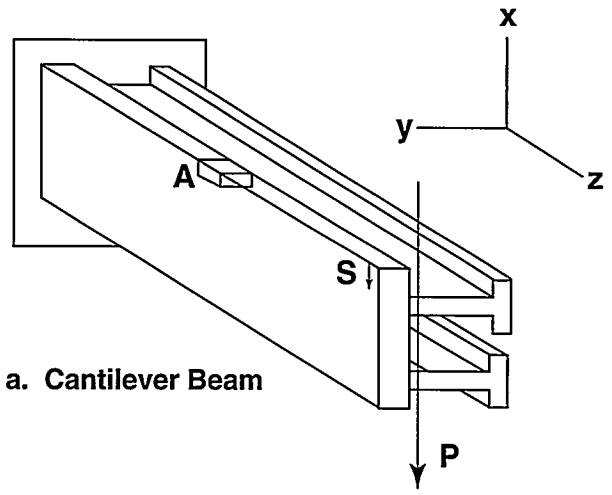

a. Cantilever Beam

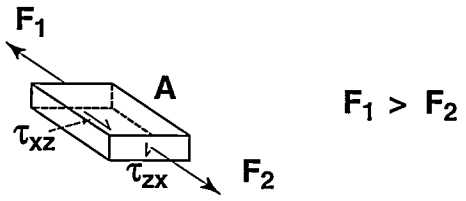

b. Segment A showing direction of shear stresses

Fig. 54. Cantilever beam representation of I-40 Bridge cross section.

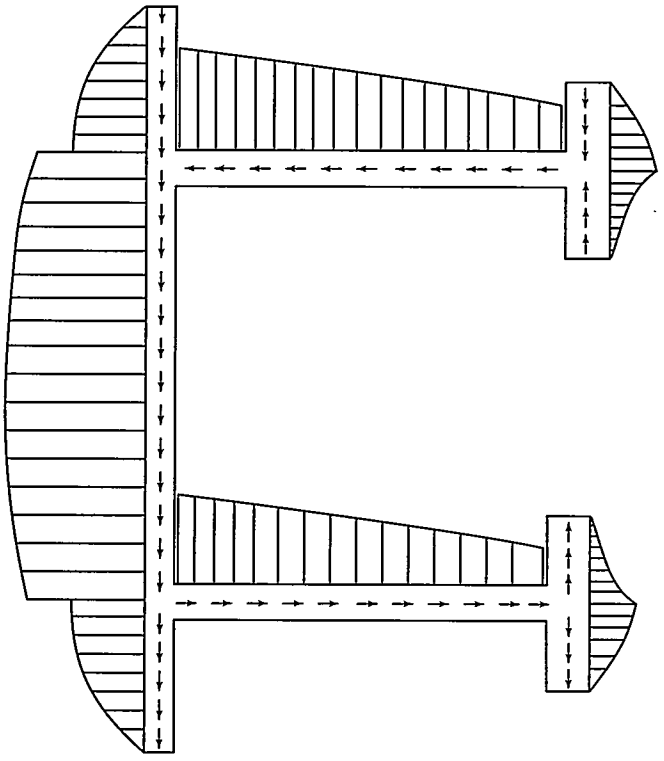

Fig. 55. Shear stress distribution and shear flow in I-40 Bridge approximation.

A small element labeled "A" is cut from the bridge deck as shown in Fig. 54. Force F_1 is greater than force F_2 because the bending moment increases toward the fixed end of the beam. For equilibrium, element A requires a shear force in the direction shown on its bottom surface. This force results in the shear stress, τ_{xz}, shown in Fig. 54. Moment equilibrium of element A requires a downward transverse shear force on its front face resulting in the shear stress, τ_{zx}, shown in Fig. 54. The magnitude of the shear stress, τ, can be determined using standard strength-of-materials analysis (Gere and Timoshenko, 1990) as

$$\tau = \frac{V_x Q_y}{I_y t} \tag{15}$$

if it is assumed that shear stresses, τ, are directed along the centerline of the cross section and are of constant magnitude across the wall thickness. Here, V_x is the resultant shear force acting on the cross section in the x-direction, I_y is the moment of inertia about the centroidal y-axis, t is the section thickness at the location where τ is being evaluated, and Q_y is the first moment of area of the cross section from s = 0 to S (See Fig. 54) measured with respect to the neutral axis.

Following Gere and Timoshenko (1990) the procedure is to

1. Determine the direction of the shear flow in each segment of the cross section by inspection.
2. Determine the magnitudes of the shear stresses at all points in the cross section. (The general shape of the shear stress distribution is shown in Fig. 55).
3. Determine the resultant shear forces in each segment of the cross section.
4. Apply statics to determine the location of the shear center.

A detailed summary of the application of steps 1 through 4 is presented in Appendix B. Corresponding shear-center locations, e, measured from the center of the transformed concrete slab, are

Thin-flange section: e = 23.63 in.

Thick-flange section: e = 33.55 in.

The shear center for the I-40 Bridge was also located numerically using the ABAQUS shell model BR3W described in Section IV. B. The procedure is shown conceptually in Fig. 56 where a static force, V_x, is applied to the bridge cross section using a rigid link offset from the center of the concrete slab by a distance e. By calculating the rotation of the cross section about the z-axis for two different values of e, an extrapolation was made to determine the value of e that results in no net rotation of the cross section. This value of e defines the location of the shear center. A third run with this value of e verified that the shear center had been accurately located. It should be noted that the location of the shear

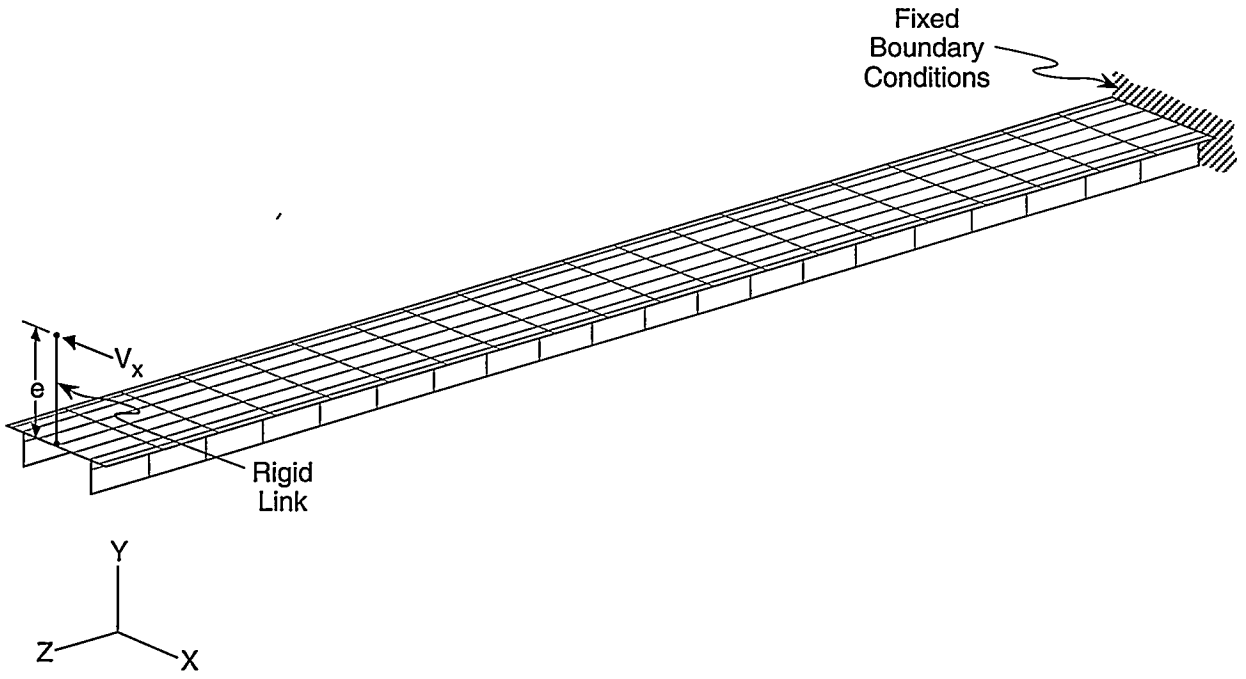

Fig. 56. Finite element model used to determine the shear-center location.

center identified in this matter is actually an "average" shear-center location because the cross-section geometry of the plate girders varies along the length of the bridge. The value of e identified by this procedure lies between the values calculated by the closed-form method, as would be expected, lending further credibility to the accuracy of the closed-form solution.

Because the shear-center location is an essential parameter that is necessary to develop an accurate simplified beam model of the bridge, a procedure for determining the shear-center location of general thin-walled, open cross sections, which does not require detailed finite element modeling or time-consuming closed-form solution, is needed.

V. B. 3. Numerical Method for Locating the Shear Center

Numerical procedures discussed by Heins (1975) and others (Galambos (1968) and Kollbrunner and Basler (1969)) can be used to determine the shear-center location. Although for the I-40 Bridge cross section it was possible to determine the shear center analytically (when certain simplifying assumptions were made), a numerical procedure is more easily adapted to other geometries and does not require the simplifying assumptions made previously.

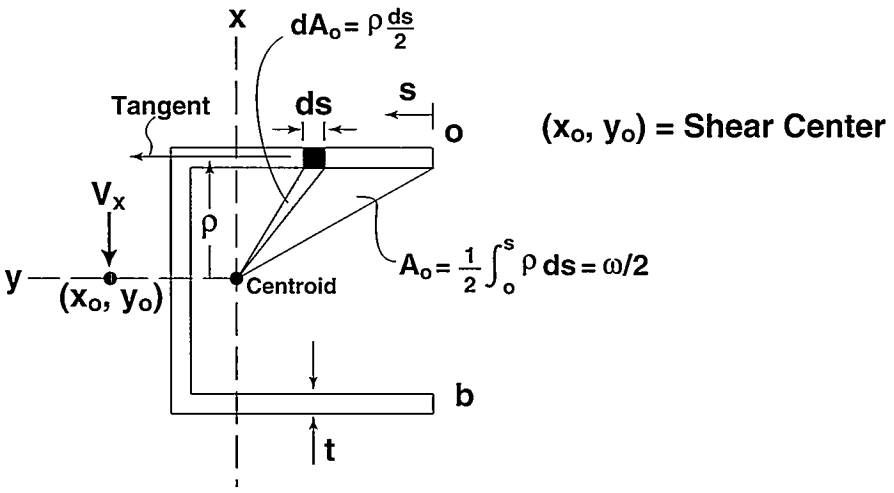

Fig. 57. Channel section used to develop numerical procedure.

Consider, for illustrative purposes, the channel section shown in Fig. 57. Examine stresses caused by a shear force, V_x, acting in the x direction through the shear center (x_0, y_0). The coordinates x_0 and y_0 locate the shear center relative to the centroid of the cross section. Assuming thin-walled sections, which implies that the shear stress is constant across the thickness, equilibrium considerations require that

$$\tau t = -\frac{V_x}{I_y}\int_o^s xt\ ds. \tag{16}$$

The integral

$$\int_o^s xt\ ds \tag{17}$$

is referred to as the **statical moment of area,** and it is based on the area bounded on one end by the location in the cross section at which the shear flow, τt, is evaluated.

If the shear force is applied through the shear center, the moment about the centroid caused by this force, $V_x y_0$, must be equal and opposite to the moment caused by the resultant shear stresses acting over their respective areas. Referring to Fig. 57, this relation can be stated as

$$V_x y_0 = \int_o^b \rho\tau t \; ds, \text{ or} \tag{18}$$

$$y_0 = \frac{1}{V_x} \int_o^b \rho\tau t \; ds, \tag{19}$$

where ρ is the lever arm for the resultant shear force, or more specifically, it is the perpendicular distance from a tangent in the s-direction of an element ds to a parallel axis passing through the centroid. In general, ρ will be a function of s. Substituting Eq. 16 into Eq. 19 yields

$$y_0 = -\frac{1}{I_y} \int_o^b \rho \left(\int_0^s xt \; ds \right) ds. \tag{20}$$

Referring to Fig. 57, the total shaded area from 0 to s is

$$A_0 = \frac{1}{2} \int_0^s \rho \; ds, \tag{21}$$

and A_0 is referred to as the **sectorial area.** The d**ouble sectorial area**, $2A_0$, or **unit warping constant with respect to the centroid** is labeled ω, and is defined as

$$\omega = 2A_0 = \int_0^s \rho \; ds, \tag{22}$$

and hence $d\omega = \rho \; ds.$ (23)

Substituting Eq. 23 into Eq. 20 yields

$$y_0 = -\frac{1}{I_y} \int_o^b \left(\int_0^s xt \; ds \right) d\omega. \tag{24}$$

Integration by parts gives the relationship

$$\int udv = uv - \int vdu, \tag{25}$$

and with the substitutions

$$u = \int_0^s xt \; ds,$$

$$dv = d\omega,$$

$$du = xt \; ds, \text{ and}$$

$$v = \omega$$

Eq. 24 becomes

$$y_0 = -\frac{1}{I_y}\left(\omega \int_0^b xt\, ds - \int_0^b \omega xt\, ds \right). \tag{26}$$

But, t ds = da, hence

$$\int_0^b xt\, ds = \int_a xda = 0 \tag{27}$$

because x is measured from the centroid. Therefore

$$y_0 = \frac{\int_0^b \omega xt\, ds}{I_y}. \tag{28}$$

The quantity

$$\int_0^b \omega xt\, ds \tag{29}$$

is defined as $I_{\omega x}$ and is referred to as the **warping product of inertia**. Substituting this designation into Eq. 28 yields the following relation for the location of the shear center

$$y_o = \frac{I_{\omega x}}{I_y}. \tag{30}$$

The above derivation follows that given by Galambos (1968) for a general thin-walled section.

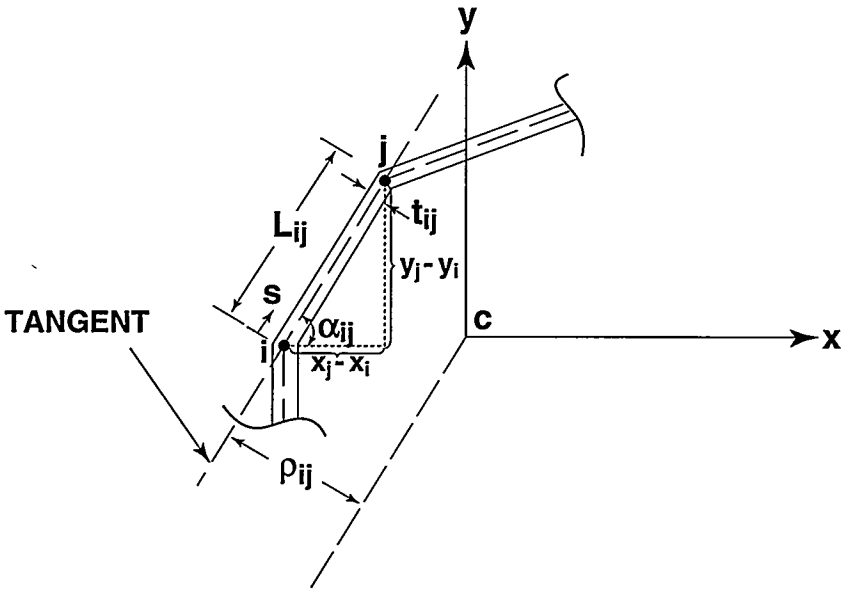

Fig. 58. A general thin rectangular element making up the cross section of a beam.

Heins (1975) presents a numerical procedure for evaluating $I_{\omega x}$ assuming the cross section can be idealized as a series of straight, connected segments, as shown in Fig. 58. At some distance s in Fig. 58, there exists an element ij of thickness t_{ij} and length L_{ij}. From Eq. 22 it is seen that the parameter ω can be represented as

$$\omega_j = \omega_i + \rho_{ij} L_{ij} \tag{31}$$

and that it varies linearly over the segment ij. Therefore, over segment ij $\omega(x)$ can be expressed as

$$\omega(x) = \omega_i + \frac{(\omega_j - \omega_i)(x - x_i)}{(x_j - x_i)}. \tag{32}$$

It is also noted from examination of Fig. 58 that

$$ds = \frac{dx}{\cos \alpha_{ij}}, \tag{33}$$

and the integral expression for the warping product of inertia given by Eq. 29 can be written as

$$I_{\omega x} = \sum_{k=1}^{n} \frac{t_{ij}}{\cos \alpha_{ij}} \int_{x_i}^{x_j} \left[\omega_i + \frac{(\omega_j - \omega_i)(x - x_i)}{(x_j - x_i)} \right] x \; dx, \tag{34}$$

where k is an index representing the n thin rectangular elements forming the cross section.

Figure 58 shows that

$$\cos \alpha_{ij} = \frac{x_j - x_i}{L_{ij}}. \tag{35}$$

Based on algebraic manipulation of the integration results from Eq. 34, and Eq. 35, the expression for the warping product of inertia given in Eq. 29, can be evaluated as

$$I_{\omega x} = \frac{1}{3} \sum_{k=1}^{n} (\omega_i x_i + \omega_j x_j) t_{ij} L_{ij} + \frac{1}{6} \sum_{k=1}^{n} (\omega_i x_j + \omega_j x_i) t_{ij} L_{ij}. \tag{36}$$

Similarly, Fig. 58 shows the moment of inertia I_y, appearing in Eq. 16 can be represented as

$$I_y = \int_A x^2 dA = \int_o^b x^2 t ds = \sum_{k=1}^{n} \frac{t_{ij}}{\cos \alpha_{ij}} \int_{x_i}^{x_j} x^2 dx. \tag{37}$$

Substituting Eq. 35 into Eq. 37 and evaluating the integral gives the following expression for the moment of inertia about the y axis:

$$I_y = \frac{1}{3} \sum_{K=1}^{n} (x_i^2 + x_i x_j + x_j^2) t_{ij} L_{ij}. \tag{38}$$

For the numerical evaluation, tabular procedures, amenable to spreadsheet formulation, are given by Heins. However, it should be mentioned in passing that several confounding factors present themselves for the I-40 Bridge cross section. One is the presence of "branchings" whose inclusion in the tabular procedure is not fully discussed by Heins. Kollbrunner and Basler (1969) indicate that thin-walled open cross sections that cannot be fully described by a single path coordinate will require a modification of the tabular procedure.

A relatively simple cross section was selected as an example for initial verification of the numerical method. The particular cross section selected has the following attributes in common with the I-40 Bridge cross section:

1. There is only a single axis of symmetry, that is, the centroid and shear center are not collocated; and

2. The cross section contains "branches" (i.e., more than two intersecting elements).

Further, the actual shear center is known "exactly."

The cross section analyzed is shown in Fig. 59. It is assumed here that all cross sections are thin-walled. Centerline dimensions are used. The distance from the centerline of the web to the shear center, labeled e in Fig. 59, is shown by Gere and Timoshenko (1990) to be

$$e = \frac{3t_f(b_2^2 - b_1^2)}{ht_w + 6t_f(b_1 + b_2)}, \tag{39}$$

where t_f, t_w, b_1, b_2, and h are defined in Fig. 59. Shear flow directions and shear stress distributions for this cross section are shown in Fig. 60.

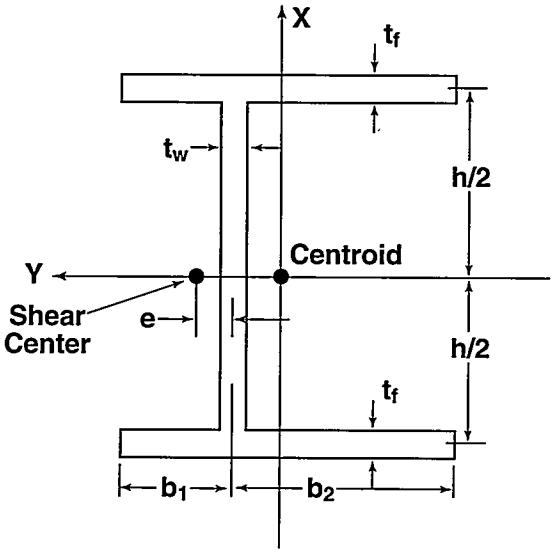

Fig. 59. Branched cross section used to verify numerical procedure for locating the shear center.

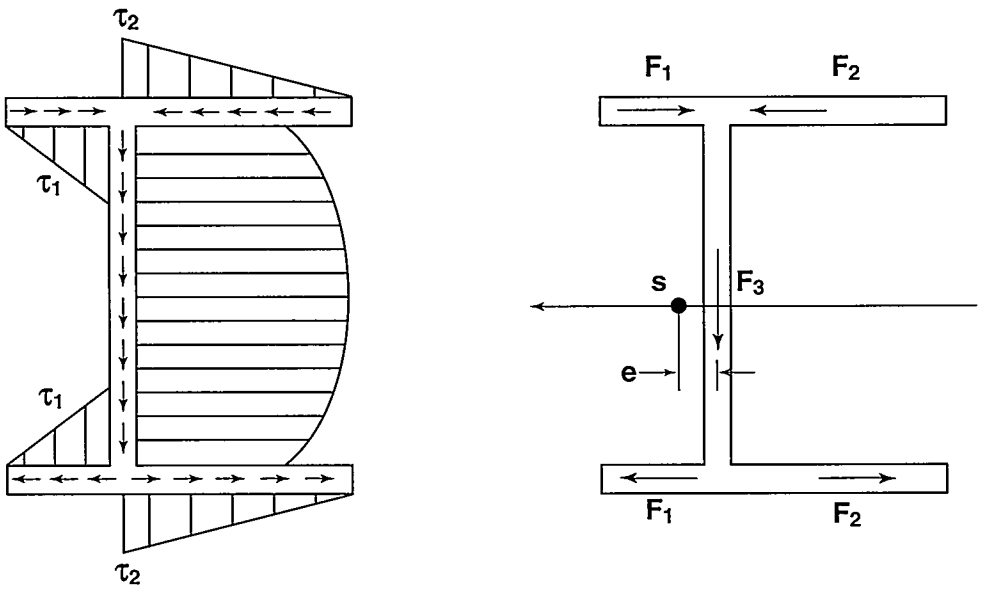

Fig. 60. Shear flow and shear stress distribution in the branched cross section.

The numerical solution for this cross section is done by first adopting Heins' "continuous flow" argument across the section points 1-2-3-4 identified in Fig. 61. The "flow" in the other elements is assumed "directed from the free edges to the intersections" (Heins, 1975) as shown in Fig. 61. Note that the "flow" in section 6-3 of Fig. 61 is directed opposite to that shown in Fig. 60 and does not correspond to the shear flow.

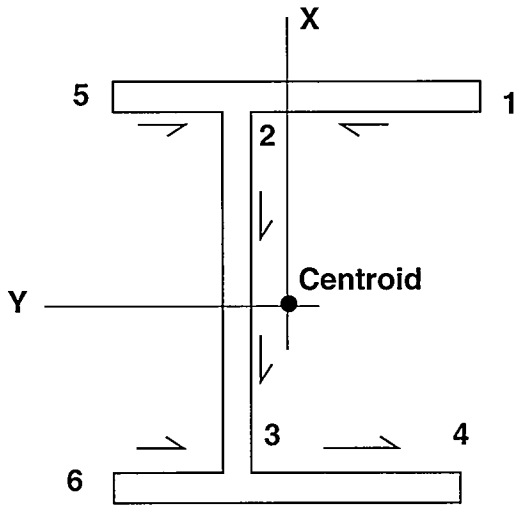

Fig. 61. Flow based on Heins' method.

The Heins procedure was placed in tabular format, as shown in Table XIV, using the EXCEL (Microsoft, 1993) spreadsheet. The first column identifies the points and elements. First, those points and elements associated with the continuous flow 1-2-3-4 are identified. The numerical procedure proceeds from a known value at point 1 proceeding through point 4. Segments 5-2 and 6-3 are next treated. Basically, the calculation is done in reverse for these "branches." For example, take branch 5-2. Quantities at point 2 have been previously calculated in the procedure, appearing earlier in the table. Values at point 2 are then used to calculate values at point 5 in an order reverse from the direction used for the first four points. Thus, one proceeds from the known values at point 2 up the table to unknown point 5.

TABLE XIV
Spreadsheet for Calculation of Shear-Center Location

SHEAR CENTER DETERMINATION FOR CROSS SECTION SHOWN IN FIG. 59															
1	2	3	4	5	6	7	8	9	10	11	12	13	14	15	16
POINT	X	Lij	RHOij	Wij	Wi	Tij	Tij Lij	Wi Xi	Wj Xj	Wi Xj	Wj Xi	SUM 1	SUM 2	Iy	
1	10				0										
1--2		10	10	100		0.2	2	0	1000	0	1000	2000	2000	600	
2	10				100										
2--3		20	1.875	37.5		0.1	2	1000	-1375	-1000	1375	-750	750	200	
3	-10				137.5										
3--4		10	10	100		0.2	2	-1375	-2375	-1375	-2375	-7500	-7500	600	
4	-10				237.5										
5	10				150										
5--2		5	-10	-50		0.2	1	1500	1000	1500	1000	2500	2500	300	
2	10				100										
6	-10				87.5										
6--3		5	10	50		0.2	1	-875	-1375	-875	-1375	-2250	-2250	300	
3	-10				137.5							-6000	-4500		
								Iwx	yo					Iy SUM	ZBAR
								-2750	-4.125					666.7	1.875
INPUT															
ZH	B1	B2	Tf	Tw											
20	5	10	0.2	0.1											
SHEAR CENTER LOCATION FROM CENTER OF WEB															
2.25															

The second column is the x-coordinate of the *i*th point (See Fig. 58). The third column denotes the length, L_{ij} of the *ij*th element. The fourth column denotes the perpendicular distance, ρ_{ij}, between a tangent to element ij and an axis parallel to this tangent passing through the centroid, as shown in Fig. 58. The sign convention for ρ_{ij} is that, as one proceeds along the element from i to j, ρ is positive if the centroid is to the left of element ij. In the branched sections the sign convention for ρ is based on the path coordinate originating at the free end, that is, location i is the free end and location j is the end with a known value of ω. Note in this example that to determine the sign for ρ_{23}, it is necessary to know the centroid location. It is straightforward to show that, for the example in Fig. 59, the centroid is located at

$$y_c = \frac{t_f(b_2^2 - b_1^2)}{2t_f(b_1 + b_2) + ht_w}. \tag{40}$$

The fifth column, ω_{ij}, is the product $\rho_{ij}\ L_{ij}$, and the sixth column, denoted ω_i, is the sum denoted in Eq. 31. T_{ij} in the seventh column is the thickness of the *ij*th element, and $T_{ij}\ L_{ij}$ in the eighth column is simply the area of the *ij*th element.

The next four columns (9-12) are the corresponding four terms $\omega_i x_i$, $\omega_j x_j$, $\omega_i x_j$, and $\omega_j x_i$ that can be identified in Eq. 36. Column 13 (SUM1) represents the term

$$(w_i x_i + \omega_j x_j)\ t_{ij}\ L_{ij}, \tag{41}$$

and column 14 (SUM2) denotes the term

$$(\omega_i x_j + \omega_j x_i)\ t_{ij}\ L_{ij}. \tag{42}$$

Both these terms are found in Eq. 36. The parameter $I_{\omega x}$ is then computed from the sum of column 13 and of column 14 according to Eq. 36.

The moment of inertia (about the centroid) is determined using Eq. 38. Entries in column 15 are

$$\left(x_i^2 + x_i x_j + x_j^2\right) t_{ij} L_{ij}. \tag{43}$$

This column is then summed and divided by 3 according to Eq. 38, and the result is presented below column 15.

The various entries in Table XIV correspond to a numerical example where the following geometric parameters, corresponding to those shown in Fig. 59, were assigned

$$\begin{array}{ll} h = 20.0 & t_f = 0.2 \\ b_1 = 5.0 & t_w = 0.1 \\ b_2 = 10.0 & \end{array} \tag{44}$$

Using the above input, the shear-center location, relative to the centroid, is found in Table XIV to be $y_0 = -4.125$. Inspection of Fig. 59 reveals that the shear-center location given by Eq. 39 is measured relative to the center of the web, not the centroid. Further, e is measured positive in the negative y direction. Therefore, the following equation relates the shear-center location, y_0, determined using Heins' method with that in Eq. 39:

$$y_0 = -(e + y_c). \tag{45}$$

For $e = 2.25$ (Eq. 39), $y_c = 1.875$ (Eq. 40) and $y_0 = -4.125$ (Table XIV), it can be seen that Eq. 39 is satisfied implying that the shear-center location calculated by Heins' method agrees exactly with the closed-form solution given by Gere and Timoshenko (1990) for this numerical example.

In Appendix B this numerical procedure is applied to the transformed I-40 Bridge cross section (neglecting the three stringers), and the shear-center locations obtained are (measured from the center of the transformed slab)

Thin-flange section: e = 23.63 in., and

Thick-flange section: e = 33.53 in.

These values are in almost exact agreement with those obtained by the closed-form procedure discussed in Section V. B. 2. These results indicate that Heins' numerical procedure is an efficient and accurate method to locate the shear center of a general cross section made up of thin-walled rectangular members of different materials.

A final calculation (also summarized in Appendix B) was made to examine the effect of the neglected stringers on the shear-center location of the thin-flange section. Before calculating the new shear-center location, it was necessary to determine the new centroidal location that reflects the addition of the stringers. Results of this calculation yield a shear-center location (measured from the center of the transformed slab) of

Thin-flange section (stringer included) : e = 23.52 in.

This result indicates that, for the I-40 Bridge cross section, neglecting the stringers introduces less than a 0.5 percent error in the calculated shear-center location.

V. B. 4. Numerical Method for Determination of the Warping Constant and Sectorial Moment

Heins' numerical procedures are now utilized to calculate the warping constant and sectorial moment for a thin-walled open cross section. It should be noted that the method for determining the shear center is referenced to the centroid of the cross section. The procedure for determining the warping torsional constants, on the other hand, is referenced to the shear center. First, the double sectorial area or unit warping with respect to the shear center, ω_0, is defined as

$$\omega_o = \int_o^s \rho_o ds, \tag{46}$$

or in discrete form as

$$\omega_o = \sum \rho_{oij} L_{ij} \tag{47}$$

where ρ_{oij} is the perpendicular distance between a tangent along the length of a thin rectangular element of length L_{ij} and a parallel axis passing through the shear center. The sign convention on ρ_{oij} is that in going from point i to point j along L_{ij}, ρ_{oij} is positive if the shear center is to the left.

Next, the integral

$$\int \omega_o t ds, \tag{48}$$

where t is element thickness, is evaluated for an element ij using Heins (1975) as

$$\sum t_{ij} L_{ij} \left(\omega_{0_i} + \omega_{0_j}\right)/2. \tag{49}$$

The **normalized unit warping** of the cross section is given by Heins as

$$W_n = \frac{1}{A} \int \omega_o t ds - \omega_o \tag{50}$$

where A is total cross-sectional area, $\Sigma\ t_{ij}\ L_{ij}$.

Numerically, this normalized unit warping is written by Heins at point i for any element ij as

$$W_{n_i} = \left[\frac{1}{2A} \sum_{1}^{n} \left(\omega_{0_i} + \omega_{0_j}\right) t_{ij} L_{ij}\right] - \omega_{0_i} \tag{51}$$

where n is the number of rectangular members forming the cross section. The **warping constant**, I_ω, is defined by Heins as

$$I_\omega = \int_{o}^{b} W_n^2 t ds \tag{52}$$

where b is the entire length of the section. The numerical evaluation of this warping constant is given by

$$I_\omega = \frac{1}{3} \sum_{1}^{n} \left(W_{n_i}^2 + W_{n_i} W_{n_j} + W_{n_j}^2\right) t_{ij} L_{ij}. \tag{53}$$

Finally, the **warping statical moment**, S_w, is given by Heins as

$$S_w = \int_0^b W_n t ds. \tag{54}$$

This integral can be written in a form for numerical evaluation as

$$S_w = \frac{1}{2}\sum_1^n \left(W_{n_i} + W_{n_j}\right) t_{ij} L_{ij}. \tag{55}$$

Note that the warping constant, I_ω, is identical to the warping constant, Γ_ω required in the input data for the ABAQUS program. Further, the warping statical moment, S_w, is identical to the sectorial moment, Γ_0, required for ABAQUS.

To verify the accuracy of Heins' numerical method for calculating the warping constant and warping statical moment, a spreadsheet calculation was made for a wide-flange, W 36 X 359 beam where the web thickness, t_w = 1.12 in., the flange thickness, t_f = 2.01 in., the flange width, b = 16.73 in., and the beam depth, d = 37.4 in. For this case the shear center and centroid coincide, but the section is branched. The spreadsheet is shown in Table XV.

TABLE XV
Spreadsheet for Calculation of Warping Constant and Sectorial Moment

DETERMINATION OF TORSIONAL CONSTANTS FOR W 36 X 359 CROSS SECTION										
POINT	RHO ZERO	Lij	RHO*Lij	W ZERO	Tij	Tij Lij	(Wi+Wj)TijLij	Wn	WARPING	STATICAL
1				0				148.0653		
1--2	17.69	8.37	148.0653		2.01	16.8237	2491.006188		368831.578	2491.006
2				148.0653				0		
2--3	0	33.38			1.12	37.3856	11071.02016		0	0
3				148.0653				0		
3--4	17.69	8.37	148.0653		2.01	16.8237	7473.018563		368831.578	-2491.01
4				296.1306				-148.065		
5				296.1306				-148.065		
5--2	-17.69	8.37	-148.065		2.01	16.8237	7473.018563		368831.578	-2491.01
2				148.0653				0		
6				0				148.0653		
6--3	17.69	8.37	148.0653		2.01	16.8237	2491.006188		368831.578	2491.006
3				148.0653				0		
						104.68	30999.06966		1475326.31	0
			WARPING CONSTANT=			491775				
		WARPING STATICAL (SECTORIAL) MOMENT=					0			

Column 1 in Table XV is identical to that used in Table XIV for the shear-center determination. The second column, labeled "RHO ZERO," is the perpendicular distance, in inches, from an axis through the shear center parallel to a tangent through a given element in the cross section. Points and elements of the cross section are identified in Fig. 62 where it can be seen that the shear center coincides with the centroid. Note the sign convention on ρ_0, for element 5-2. When considering a path from point 5 to point 2, the shear center is to the right, so ρ_0 is negative for element 5-2.

In column 3 "L_{ij}" is the length, in inches, of element ij, as in Table XIV. Column 4, labeled "RHO*L_{ij}" is the product of the second and third columns and is used to calculate the double sectorial area in column 5. This column, labeled "W ZERO" is used to calculate the double sectorial area at each point in the cross section, starting from point 1 and continuing through point 4 downward in the table using values in column 4. The procedure for the "branches" 5-2, and 6-3, is to proceed from the known quantity (2 or 3) to the unknown quantity (5 or 6) upward in the table. Column 6, "T_{ij}," is the thickness of each element in inches. Column 7, "$T_{ij}\ L_{ij}$," is the product of columns 3 and 6.

Column 8, "$(W_i + W_j)\ T_{ij}L_{ij}$," is constructed from columns 5 and 7. It is used in the calculation of the normalized unit warping given by Eq. 51.

Column 9, "Wn," is also used for the calculation of the normalized unit warping. In Eq. 51

$$A = \sum_{i=1}^{n} t_{ij}L_{ij} \tag{56}$$

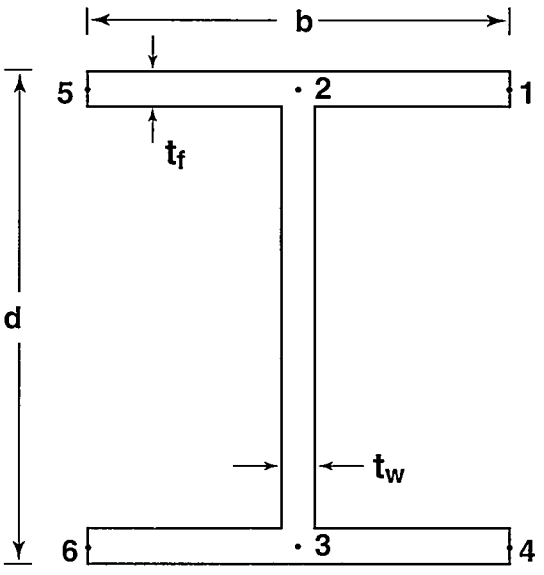

Fig. 62. Wide flange W 36 X 359 beam used to verify numerical method of evaluating the warping constant and statical warping moment.

and is the sum of column 7. Also the term

$$\sum_{1}^{n}\left(\omega_{0_i}+\omega_{0_j}\right)t_{ij}L_{ij} \tag{57}$$

is the sum of column 8.

Finally, the term ω_{0_i} in Eq. 51 is obtained from the *i* th row of column 5.

Column 10, "WARPING," evaluates the term

$$(W_{n_i}^2+W_{n_i}+W_{n_j}+W_{n_j}^2)t_{ij}L_{ij} \tag{58}$$

in Eq. 53 for each element. The column is summed at the bottom of the column. The result is divided by 3 and is identified near the bottom of the spreadsheet as "WARPING CONSTANT."

Column 11, "STATICAL", evaluates the term

$$(W_{n_i}+W_{n_j})t_{ij}L_{ij} \tag{59}$$

in Eq. 51 for each element. The column is summed at the bottom of the column. The result is divided by 2 and is identified at the bottom of the spreadsheet as "WARPING STATICAL MOMENT."

For this example a warping constant of 491775 in^6 is identified and a statical warping moment of 0 in^4 are identified. This warping constant can be compared to the closed-form solution given by Oden and Ripperger (1981) as

$$I_\omega=\frac{t_f b^3\left(d-t_f\right)^2}{24}. \tag{60}$$

The geometric parameters of the W 36 X 359 beam listed above give a warping constant of 491172 in^6, a 0.12 percent difference from the closed-form solution. Note the AISC Steel Manual (1989) lists a warping constant of 493000 in^6 for this section, but this value includes the fillets. The statical warping moment should be zero when evaluated relative to the shear center.

From this example it is evident that the numerical method given by Heins for calculating the warping constant and the statical warping moment has been accurately implemented in a spreadsheet and can be applied to the I-40 Bridge cross section.

Spreadsheet calculations of the two torsional constants, I_ω and S_w, of the transformed I-40 Bridge cross section (neglecting the stringers) using Heins' numerical procedure are summarized in Appendix C. The calculations resulted in the following values for the torsional constants needed to model the I-40 Bridge:

Thin-flange section: $I_\omega = 3.35 \times 10^{10}$ in^6 $S_w = 6.69 \times 10^{-10}$ in^4

Thick-flange section: $I_\omega = 5.06 \times 10^{10}$ in^6 $S_w = 6.98 \times 10^{-10}$ in^4

These values do not include the effects of the stringers. An additional run, also summarized in Appendix C, was made adding the stringers to the transformed geometry of the thin-flange section to assess the stringers' effect on the torsional constants. The results of this calculation are

Thin-flange section: (Stringers Added) $I_\omega = 3.35 \times 10^{10}$ in^6

It is seen that neglecting the stringers has negligible effect on calculated torsional constants.

At this point, only the mass density and cross-sectional area of the beam are yet unspecified in the ABAQUS input. Further, the bending and torsional static responses have been properly accounted for in the input data at this point. However, there are additional considerations regarding both torsional and bending responses when beam dynamics are considered, as discussed in the next section.

V. C. Modeling the Mass Distribution

For the torsional portion of the coupled beam response to be correct, the generalized torsional mass must be input properly. This implies that the mass polar moment of inertia about the center of mass must be correct. The area polar moment of inertia in ABAQUS is internally computed from the user-supplied area moments of inertia as

$$I_p = I_{11} + I_{22} \; (= I_x + I_y, \text{ based on axes shown in Fig. 34}). \tag{61}$$

The quantity $\mu L I_p$, where L is the length of the beam, then provides the generalized torsional mass necessary to correctly model the torsional vibration response. A confounding factor is that I_{11} (I_x) and I_{22} (I_y) are input about the centroid of the cross section which, for a composite cross section, is not, in general, coincident with the center of mass. Unfortunately, I_p cannot be explicitly input to ABAQUS. Therefore, in order to input the appropriate rotating mass for torsional vibrations, it is necessary to modify one of the input parameters μ, A, or L. The length of the beam cannot be modified. Further, the cross-sectional area, A, will need to be modified to properly model the generalized flexural

mass. Therefore, the remaining possibility is to determine a modified density, μ, which results in the proper rotating mass.

The procedure utilized is to calculate the center of mass of the composite steel/concrete beam cross section, determine the polar moments of inertia about the center of mass for both steel and concrete components in the cross section, and then use the following equation to determine an equivalent mass density, μ_{eq}, for torsional vibrations:

$$\mu_{eq} = \frac{\mu_c I_{pc} + \mu_s I_{ps}}{I_{11} + I_{22}}, \tag{62}$$

where I_{11}, I_{22} = Transformed area moments of inertia supplied to ABAQUS,
μ_S = Mass density of steel,
μ_C = Mass density of concrete,
I_{ps} = Polar area moment of inertia of steel cross section about the center of mass, and
I_{pc} = Polar area moment of inertia of concrete cross section about the center of mass.

Finally, the area of the equivalent beam is specified such that

$$A = \frac{A_c \mu_c + A_s \mu_s}{\mu_{eq}}, \tag{63}$$

where A_c = the area of concrete forming the cross section, and
A_s = the area of steel forming the cross section.

The value of μ_{eq} and A given by Eq. 62 and Eq. 63, respectively, will give the proper mass distribution to simulate the flexural dynamics using the transformed section properties (bending rotary inertia is ignored here because it is a secondary effect which may or may not be modeled in the particular beam element used by ABAQUS). Specifying the area in this manner will produce errors in the axial response of the beam, but these errors will not significantly affect the flexural or torsional response of the bridge model. Appendix A summarizes the calculation of μ_{eq} and A for the I-40 Bridge cross sections. Note that this method of calculating an equivalent mass density for the bridge cross section does not account for the mass of the floor beams. However, this mass is present in the detailed finite element model. To circumvent this problem, the mass of the floor beams was uniformly distributed along the length of the bridge and the cross-sectional area was increased so that the total mass of the cross section accounts for this additional distributed mass. By modifying the cross-sectional area only, the additional mass will not affect the torsional response of the beam model.

V. D. Kinematic Constraints and Boundary Conditions

When a beam element is used, the node points that define the element are typically located at the centroid of the cross section. The simplified beam element model of the I-40 Bridge was defined in this manner. Such a model poses problems when trying to simulate the connectivity of the plate girder to the column. As was shown in Sec. IV., the modeling of these interfaces can significantly influence the calculated mode shapes and resonant frequencies.

The following boundary conditions and kinematic constraints were applied to the beam element model of the I-40 Bridge:

1. The node of the beam representing the plate girder corresponding to the abutment end was fixed against translation in the x, y, and z direction and against rotation about the y and z axes. The coordinate axes can be seen in Fig. 35.

2. The nodes at the ends of the beam elements representing the base of the piers were fully fixed against translation and rotation in all directions.

3. Translation in the x and y directions of the nodes representing the top of the pier were constrained to similar translations of the node on the beam centroidal axis directly above the pier.

4. Rotations in the y and z directions of the nodes representing the top of the pier were constrained to similar rotations of the node on the beam centroidal axis directly above the pier.

5. Translation in the z direction of the nodes representing the top of the pier was constrained to rotation about the x axis of the node on the beam centroidal axis directly above. The constrain equation was

$$\delta_z = h\,\theta_x\,, \tag{64}$$

where δ_z is translation in the z direction of the node at the top of the pier, h is the distance from the centroidal axis of the beam to the top of the pier, and θ_x is the rotation about the x axis of node on the beam directly above the pier. The distance h can be determined from the centroid locations given in Appendix A and the details of the connection between the plate girders and piers shown in Figs. 5 through 7.

V. E. Flexural-Torsional Coupling

When the shear center and center of mass are not coincident, there will be coupling between the bending and torsional modes of response. The equation of motion for uncoupled torsional vibration is first discussed followed by a brief presentation of the coupled equations of motion.

V. E. 1. Uncoupled Torsional Vibrations

In order to investigate the torsional behavior of the I-40 Bridge, it is helpful to first consider the torsional equation of motion of a prismatic beam with two axes of symmetry in the cross section, as shown in Fig. 63. For this single-material beam, the centroidal axis is coincident with the shear-center axis. For the case where the centroidal axis is coincident with the shear-center axis, there is no coupling between bending and torsional modes of vibration.

The angle of twist, $d\theta$, in a segment of the beam, dz, is given by

$$d\theta = \frac{T}{GJ} dz \tag{65}$$

where T is the net torque acting on the two faces of the segment, G is the shear modulus, and J is the torsional constant. Applying Euler's equation about the center of mass, it can be shown that the equation of torsional motion is

$$\frac{\partial^2 \theta}{\partial t^2} = \frac{GJ}{\mu I_p} \frac{\partial^2 \theta}{\partial z^2}, \tag{66}$$

where I_p is the polar area moment of inertia of the cross section about the center of mass. Note that, for this case of a doubly symmetric cross section of a single material, the center of mass, centroid, and shear center are coincident.

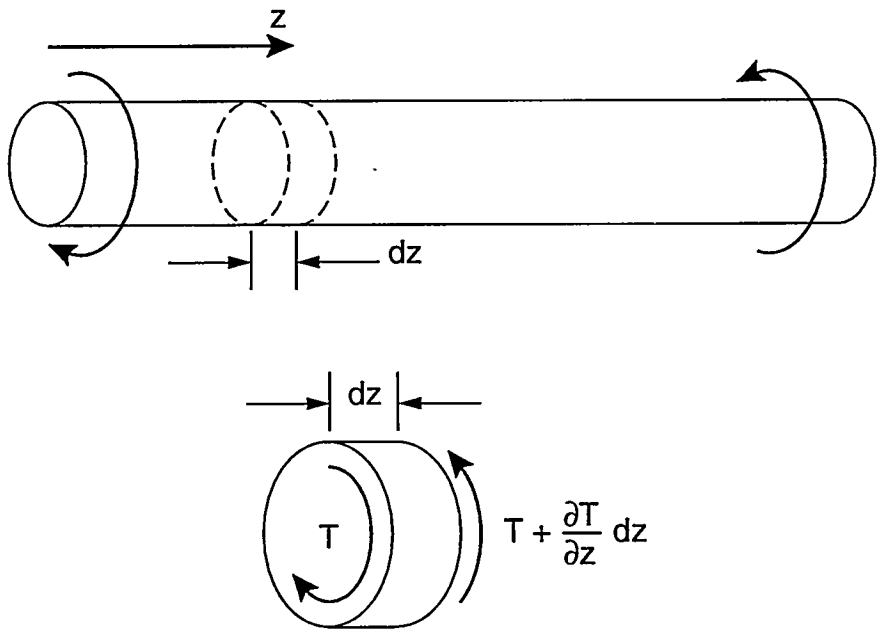

Fig. 63. Beam with two axes of symmetry undergoing torsional vibration.

Equation 66 has a solution of the general form

$$\theta(z,t) = \left[A \sin \omega \sqrt{\frac{\mu I_p}{GJ}} z + B \cos \omega \sqrt{\frac{\mu I_p}{GJ}} z \right] [C \sin \omega t + D \cos \omega t], \tag{67}$$

where A, B, C, and D are constants to be determined from boundary conditions and initial conditions.

For example, consider the particular case of a rod of length L with left end fixed and right end free. Then it can be shown (Blevins, 1979) that the natural torsional frequencies of the rod are given by

$$f_t = \left(\frac{n}{2} + \frac{1}{4} \right) \frac{1}{L} \sqrt{\frac{GJ}{\mu I_p}} \quad , n = 0, 1, 2... \tag{68}$$

Here, GJ is the generalized torsional stiffness of the beam, and μI_p is the generalized torsional mass.

V. E. 2 Coupled Flexural-Torsional Vibrations

For the torsional vibration of a beam made from a single material that was investigated in the previous subsection, the geometrical shape of the cross section was such that it possessed two axes of symmetry similar to an I-beam. In that case, the centroidal axis, about which bending would occur, is coincident with the shear-center axis.

When the shear center and centroid do not coincide, torsional vibrations will be accompanied by bending vibrations, that is, bending and torsional modes are coupled (Gere, 1954). The bending motion occurs about the centroidal axis, and torsional motion occurs about the shear-center axis. The bridge cross section under consideration in this report is an example of a cross section with a single axis of symmetry. While in this case the shear center and centroid do not coincide, the shear center does lie along the axis of symmetry.

A straightforward development of the equations for coupled bending-torsional vibrations is given by Gere and Lin (1958). Coupled bending and torsion of open-section, thin-walled beams is also discussed by in Carr (1969), Falco and Gasparetto (1973), Bishop and Price (1977), Hallauer and Liu (1982), Wekezer (1987), Bishop, et al. (1989), Dokumaci (1987), Krishnan and Singh (1991), and Capuani, et al. (1992). Other torsional vibration considerations for open-section beams are presented in Rao (1975) and Gay (1978).

Based on elementary beam theory, Gere and Lin develop the equations of motion for the most general situation in which bending vibrations in two perpendicular directions are coupled with torsional vibrations. In the special case of a cross section that has a single axis of symmetry, one of the bending vibrations is independent of the torsional vibration. For the case of a channel cross section, as shown in Fig. 64, it turns out that bending vibrations about the y-axis are coupled with torsional vibrations, whereas bending vibrations about the x-axis are independent of torsional vibrations. Gere and Lin give three equations of motion (two bending and one torsional) for the general case of no symmetry. For the case depicted in Fig. 64, where one axis of symmetry is present, these equations reduce to the following:

$$EI_y \frac{\partial^4 v}{\partial z^4} + \mu A \frac{\partial^2 v}{\partial t^2} - \mu A y_0 \frac{\partial^2 \phi}{\partial t^2} = 0 \ , \tag{69}$$

$$EI_x \frac{\partial^4 w}{\partial z^4} + \mu A \frac{\partial^2 w}{\partial t^2} = 0 \ , \tag{70}$$

$$EI_\omega \frac{\partial^4 \phi}{\partial z^4} - GJ \frac{\partial^2 \phi}{\partial z^2} - \mu A y_0 \frac{\partial^2 v}{\partial t^2} + \mu I_0 \frac{\partial^2 \phi}{\partial t^2} = 0 \ , \tag{71}$$

where : v, w = deflections of shear center in x and y directions, respectively,

ϕ = Angle of rotation of cross section,

I_y, I_x = Principal centroidal area moments of inertia,

J = Torsion constant,

E = Modulus of elasticity,

μ = Mass density of beam material,

A = Cross-sectional area,

t = Time,

y_0 = Offset of the shear center from the centroid,

I_0 = Polar moment of inertia about the shear center, "0", and

I_ω = warping constant.

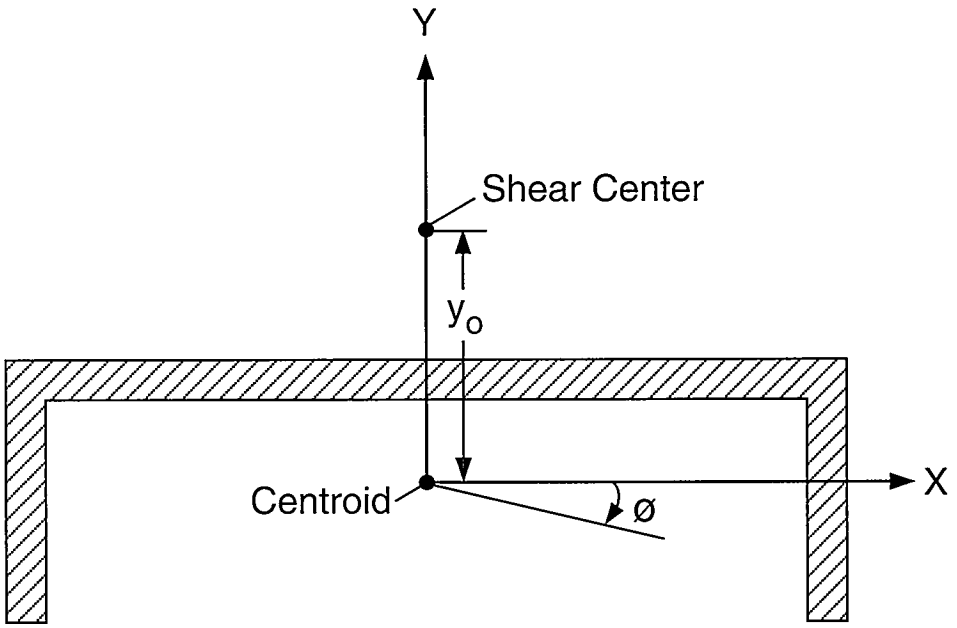

Fig. 64. Channel cross section.

Note that with y being an axis of symmetry, bending about the x axis is uncoupled, as is evidenced by the lack of a term containing ϕ in Eq. 70. By inspection, Eqs. 69 and 71 are coupled (displacement, v and rotation, ϕ). It should also be noted that Eqs. 69 and 70 are developed from the flexural considerations, and so are bending equations fundamentally. Equation 71 originated from torsional considerations. If the shear center (0) and centroid (C) were collocated, then $y_0 = 0$, and Eqs. 69 and 70 would describe purely bending response while Eq. 71 would describe purely torsional response.

Assuming solutions for displacements v, w, and ϕ in a product form Z(z) T(t), then eigenvectors (mode shapes) and eigenvalues (modal frequencies) can be found. The result for the uncoupled case, Eq. 70, will be a series of bending mode shapes and corresponding modal frequencies that describe the bending response about the x axis (See Fig. 34) and a set of coupled mode shapes and modal frequencies corresponding to torsional response coupled with bending about the y axis that is determined from Eqs. 69 and 71.

For a simply supported beam (both in bending and torsion) undergoing coupled vibrations, Gere and Lin (1958) show that there is a quadratic equation for the two coupled frequencies, f_c. The frequency for bending about an axis through the center of mass and perpendicular to the axis of symmetry is, of course, unaffected. Results are presented in terms of the uncoupled bending and torsional frequencies, f_b and f_t:

$$\frac{I_p}{I_0}\left(\frac{f_c^2}{f_b^2}\right)^2 - \left(1+\frac{f_t^2}{f_b^2}\right)\frac{f_c^2}{f_b^2} + \frac{f_t^2}{f_b^2} = 0, \tag{72}$$

where $f_b = \frac{n^2\pi^2}{L^2}\sqrt{\frac{EI_z}{\mu A}}$, n = 1, 2, 3 ... , (73)

$$f_t = \frac{n\pi}{L^2}\left[\frac{n^2\pi^2 EI_\omega + L^2 GJ}{\mu I_0}\right]^{1/2}, \text{ and} \tag{74}$$

I_p = the polar area moment of inertia about the centroid.

The resulting quadratic yields two frequencies: the lower coupled frequency is always less than the uncoupled frequencies f_b and f_t, and the upper frequency is always greater.

This change in frequencies is a smooth and implicit function of the offset, y_0. One of the frequency "branches" does emanate from a bending frequency and the other branch from a torsion frequency. For small y_0, one of the modes can be interpreted as "predominantly bending" and the other as "predominantly torsion."

V. F. Summary Of Beam Examples

To verify that the methods for calculating the torsional constant, the equivalent mass of a composite cross section, and the shear center are correct, finite element beam examples and corresponding closed-form solutions were developed. Four different beams, 100 in. long, were modeled first with shell elements and then with beam elements. The cross-section geometries of these beams are shown in Fig. 65. Two different material combinations were modeled for each cross section shown in this figure. First, steel material properties were specified for both the flanges and the web. Next, concrete material properties were specified for the flanges, and steel properties were specified for the web. Note that the overlap in the beam and the web shown in Fig. 65 was specified so that the shell element and beam element models would be as identical as possible. The finite element shell models for the I cross section and the channel cross section are shown in Fig. 66.

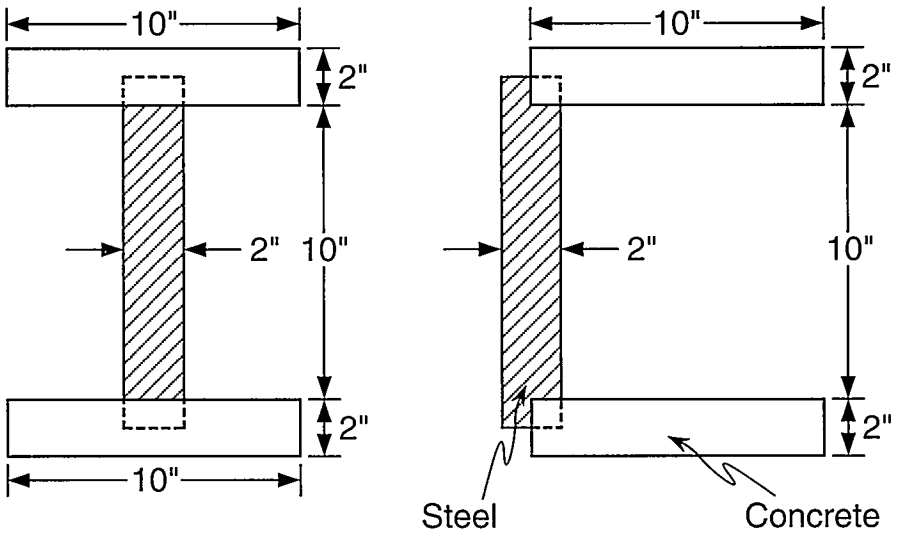

Fig. 65. Cross-section geometries used in beam verification problems.

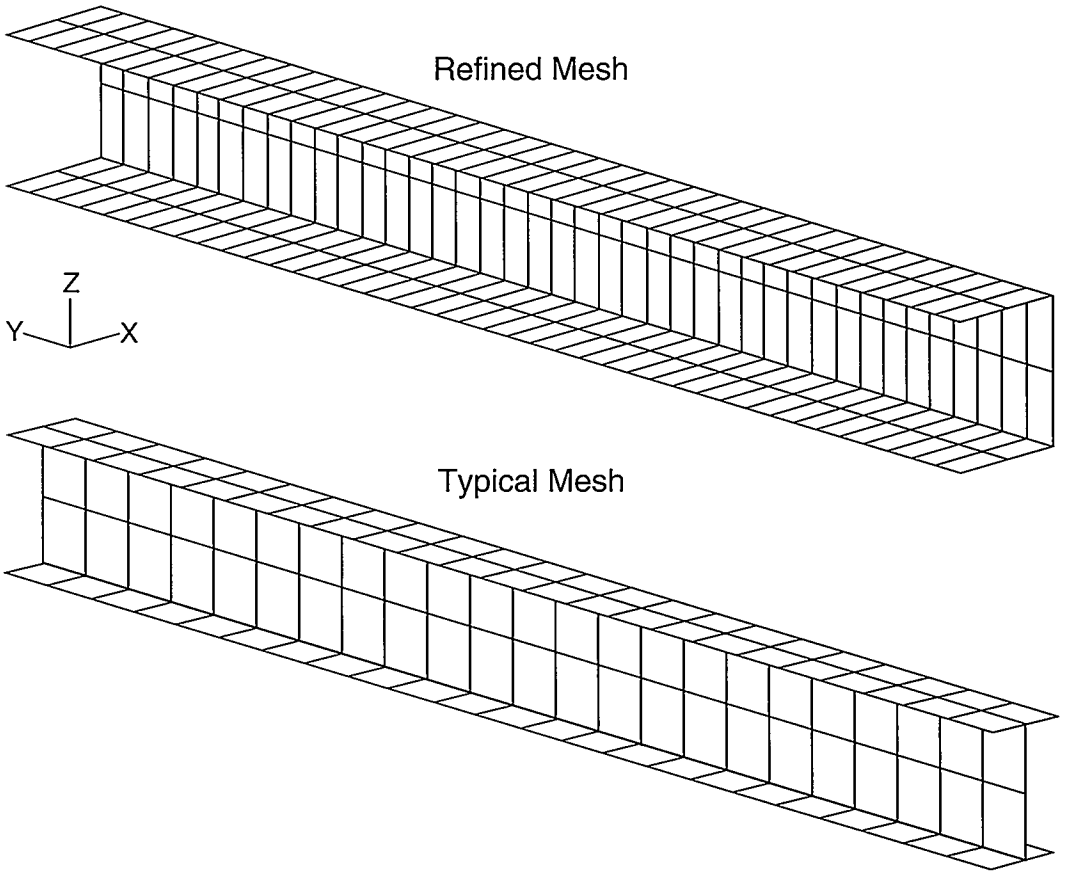

Fig. 66. Finite element meshes of the beams used in the verification problems.

Material properties that were used in these models are

Concrete: $E = 3 \times 10^6$ psi
$\nu = 0.15$
$G = 1.304 \times 10^6$ psi
$\mu_c = 2.16 \times 10^{-4}$ lb-s^2/in^4

Steel: $E = 30 \times 10^6$ psi
$\nu = 0.3$
$G = 11.54 \times 10^6$ psi
$\mu_s = 7.48 \times 10^{-4}$ lb-s^2/in^4

The first analysis to be performed was to statically apply an equal and opposite moment, T, with a magnitude of 1×10^6 in.-lbs, to either end of the all steel I cross-section shell and beam models. The center node was fixed for this analysis. The theoretical angles of rotation, ϕ, at the quarter points that should result from these applied moments are

$$\phi = \frac{TL}{GJ} = \frac{(1x10^6 lb - in)(25in)}{(11.54x10^6 psi)(74.5in^4)} = 2.91x10^{-2} rad, \quad (75)$$

where J = torsional constant given by Eq. 13, but modified to account for the width-to-thickness ratio of the rectangular sections making up the cross section as suggested by Oden and Ripperger (1981). The shell element model gave a corresponding angle of rotation of 2.88×10^{-2} rad (a 1.03% error). Results identical to the theoretical solution were obtained with the beam element model as would be expected because the value of J was explicitly specified in the input to this model. Results from these analyses verified that the beam parameters are being correctly entered into the finite element code and that the stiffness of the section is being accurately modeled.

Next, this analysis was repeated for the I section with concrete flanges and steel web. The equivalent GJ value for this section, again based on Eq. 13., is

$$GJ = 1.304 \times 10^6 \text{ psi } (46.6 \text{ in}^4) + 11.54 \times 10^6 \text{ psi } (27.9 \text{ in}^4) = 383.1 \times 10^6 \text{ lb-in}^2. \quad (76)$$

Based on Eq. 75, the theoretical angle of rotation at the quarter points is 6.53×10^{-2} rad. An angle of rotation of 6.06×10^{-2} rad was calculated with the shell-element model, a 7.2 % difference from the theoretical solution. This error was attributed to the course mesh being used to model the abrupt changes in material properties at the flange-web interface. Subsequent runs with a more refined mesh that had twice the number of elements gave a rotation of 6.20×10^{-2} rad., reducing the error to 5.1%. Again, because the values of G and J corresponding to the equivalent GJ calculated above were specifically entered for the beam model, this model gave results identical to theoretical solution. The results obtained with the shell model imply that the method given in Eq. 13 for calculating an equivalent torsion constant for a cross section built up from thin rectangular sections of different materials is correct.

These two analyses were repeated for the channel cross-section models. In theory, results identical to those obtained with the I cross-section model should be obtained for the angle of rotation. That is, the torsional stiffness of a cross section built up from thin rectangular members is independent of the orientation of those members. For the channel cross-section shell and beam models with steel specified for both the flanges and the web, results for the angle of twist at the quarter points were identical to those obtained above for the I cross section. The concrete flanges and steel web cross-section shell model gave slightly different results as the angle of rotation at the quarter points was 6.10×10^{-2} rad. These results further demonstrate the accuracy of the method given in Eq. 13 for calculating an equivalent torsion constant for a composite cross section. Table XVI summarizes the static beam examples that were run and the results that were obtained.

TABLE XVI

Summary of Static Results from Beam Examples[1]

Model	Element Type	Material	Calculated Angle of Rotation[2] (Rad)	Theoretical Angle of Rotation[3] (Rad)	Percent Error
I-Beam	Shell	Steel	2.88×10^{-2}	2.91×10^{-2}	1.03
I-Beam	Beam	Steel	2.91×10^{-2}	2.91×10^{-2}	0.00
Channel	Shell	Steel	2.88×10^{-2}	2.91×10^{-2}	1.03
Channel	beam	Steel	2.91×10^{-2}	2.91×10^{-2}	0.00
I-Beam	Shell	Composite[4]	6.06×10^{-2}	6.53×10^{-2}	7.20
I-Beam	Shell (refined)	Composite	6.20×10^{-2}	6.53×10^{-2}	5.10
I-Beam	Beam	Composite	6.53×10^{-2}	6.53×10^{-2}	0.00
Channel	Shell	Composite	6.10×10^{-2}	6.53×10^{-2}	6.59
Channel	beam	Composite	6.53×10^{-2}	6.53×10^{-2}	0.00

[1]Beam 100 in. long subjected to equal and opposite moments applied at either end of 1×10^{6} in.-lbs. Center node of the beam is fixed.
[2] Calculated at the quarter point of the beams.
[3] Obtained from Eqs. 13 and 75.
[4] Concrete flanges and steel web.

To verify that the mass distribution of the beams was being properly modeled, modal analyses were performed to determine the first torsional mode frequency. Free boundary conditions were specified for these analyses. For the steel I-beam the theoretical first torsion mode frequency, as given by Eq. 3, is 117.5 Hz. A corresponding frequency of 123.3 Hz was calculated with the shell-element model yielding a 4.94% difference from the closed-form solution. For the beam model to accurately predict the torsional frequency when free boundary conditions are specified, the mass moment of inertia about the center of mass must be specified correctly. This mass moment of inertia is calculated from the specified mass density and the area polar moment of inertia about the shear center. ABAQUS calculates I_p internally as described by Eq. 61. With area moments of inertia

about the centroid of $I_x = 1741$ in.^{4}, $I_y = 341$ in.^{4}, and μ_s specified, the beam element model of the steel I-beam gave a first torsional mode frequency of 117.5 Hz, which is identical to that given by the closed-form solution.

The shell-element model of the composite I-beam gave a first torsional mode frequency of 133.3 Hz. To obtain a closed-form result, an equivalent mass density, μ_{eq}, for the composite section must be calculated using Eq. 62. This relation gives a value of $\mu_{eq} I_p = 0.607$ lb-s^2. When this value is substituted into Eq. 3 along with the equivalent GJ given by Eq. 76, a theoretical first torsional mode frequency of 125.6 Hz is calculated. There is a 6.10% difference between this frequency and that obtained with the shell finite element model. If an I_x and I_y based on a flexural transformed section analysis are specified in the beam model of the composite I cross section, then the appropriate equivalent mass density is

$$\frac{0.607}{I_x + I_y} = 1.28 \times 10^{-3} \frac{\text{lb} - \text{s}^2}{\text{in}^4} . \tag{77}$$

With this mass density and these moments of inertia specified, the ABAQUS beam model calculates a first torsional mode frequency identical to that given by Eq. 3. It should be noted that this mass density will not necessarily be the correct equivalent mass density for flexural response, implying that the area will have to be adjusted to obtain the proper mass per unit length for flexural vibration response.

These calculations were repeated for the steel and composite channel cross-section beams. Gere and Lin (1958) show that, in general, the torsional response and the bending response about the axis of symmetry will be coupled. As shown previously in Eq. 72, the coupled frequencies are a function of the uncoupled torsional and bending frequencies (given by Eqs 2 and 3 for the case of free boundary conditions), and the ratio of the polar moment of inertia about the center of mass to the polar moment of inertia about the shear center. For the steel channel section with free boundary conditions $I_p/I_o = 2.37$ and $f_t/f_b = 0.29$. Gere and Lin show that for these ratios the torsional frequency is unaffected by the coupling. This result was obtained with the finite element shell model of the steel channel section, which gave a first torsion mode frequency of 114.7 Hz. Equation 3 gives a first torsion mode frequency of 108.1 Hz, a 6.20% difference from the finite element result. The beam finite element model of the steel channel section gives a result for the first torsional mode frequency that is identical to that obtained with Eq. 3. For this model, I_y is specified about the center of mass and is equal to 716 in^4.

For the composite channel section with free boundary conditions, $I_p/I_o = 2.37$ and $f_t/f_b = 0.45$. The mass density per unit length used in Eq. 2 to calculate f_b was calculated as

$$\rho = \mu_c A_c + \mu_s A_s = 0.0266 \frac{\text{lb} - \text{s}^2}{\text{in}^2}, \tag{78}$$

where A_c = the area of concrete, and
A_s = the area of steel.

Again, Gere and Lin show that these ratios will result in the torsional mode being unaffected by the coupling implying that Eq. 3 should accurately predict the first torsional mode frequency. The shell finite element model proved this to be the case as the first torsional mode frequency of 119.8 Hz was calculated, and Eq. 3 predicts a corresponding frequency of 112.9 Hz, a 6.11% difference. For the beam model an equivalent μI_p must be obtained in a manner similar to that given by Eq. 62. This equation give a value of $\mu I_p = 0.752$ lb-s^2 for the composite channel. Results of the dynamic analyses performed with these beam examples are summarized in Table XVII.

TABLE XVII

Summary of Dynamic Results from Beam Examples[1]

Model	Element Type	Material	Calculated First Torsional Mode Frequency (Hz)	Theoretical First Torsional Mode Frequency[2] (Hz)	Percent Error
I-Beam	Shell	Steel	123.3	117.5	4.94
I-Beam	Beam	Steel	117.5	117.5	0.00
Channel	Shell	Steel	114.7	108.1	6.20
Channel	beam	Steel	108.1	108.1	0.00
I-Beam	Shell	Composite[3]	133.3	125.6	6.10
I-Beam	Beam	Composite	125.6	125.6	0.00
Channel	Shell	Composite	119.8	112.9	6.11
Channel	beam	Composite	112.9	112.9	0.00

[1]Beam 100 in. long with free boundary conditions.
[2]Based on Eqs. 3, 13, 62, and 76.
[3]Concrete flanges and steel web.

The method of locating the shear center using a finite element model described in Sec. V. B. 2. was tested by applying it to the shell models of the steel and composite channel cross-section beams. For the steel model the thicknesses of the web and flanges were reduced to 0.2 in. to better simulate thin-wall behavior. The composite model had a specified flange thickness of 0.2 in. and a web thickness of 0.02 in. The resultant shear forces in the flange and in the web, F_v, can be obtained by integrating the shear flow, q, over the length

$$F_v = \int_0^L q dL. \tag{79}$$

By summing moments about the center of the web, as shown in Fig. 67, the location of the shear center can be determined in closed form. Note that for the composite section, an equivalent steel representation of the concrete flanges is obtained by reducing the thickness of the flange by the shear modular ratio. This reduction is opposite of that done when considering flexural response where the width of the flange would typically be adjusted by the modular ratio. Because of the selected dimensions, the closed-form solution for the location of the shear center relative to the center of the web is 4.17 in. for both the steel and composite beams. The numerical method for locating these shear centers gave corresponding values of 4.12 for both models, a 1.2% difference from the closed-form solution, indicating that this method is an accurate way to locate the shear center.

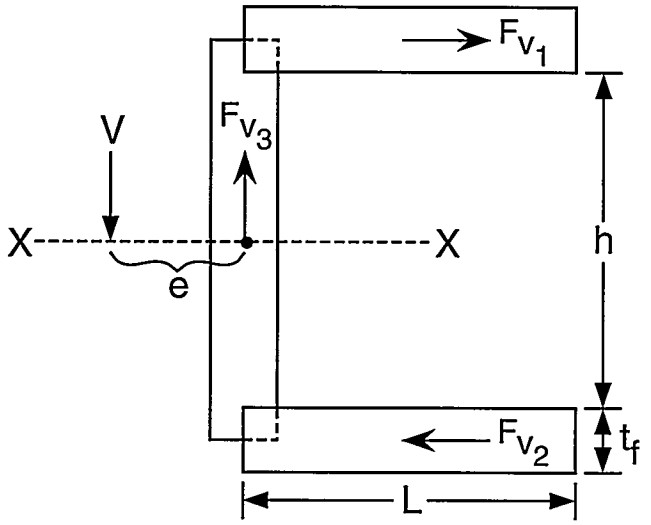

$$F_{v_1} = F_{v_2} = \frac{V\, t_f\, h}{2I_x} \int_0^L L\, dL$$

$$e = \frac{F_{v_1}\, h}{V}$$

Fig. 67. Method to locate the shear center of a channel cross section.

V. G. Summary Of The I-40 Bridge Model

Numerical values of input parameters used for the simplified beam element model of the I-40 Bridge are summarized in Table XVIII. Appendices A–C summarize the calculation of these parameters. Because the plate girders have increased flange dimensions at locations near the interior piers, two sets of beam properties were developed.

In theory, there are two options for specifying the mass moment of inertia about the shear center. An equivalent mass density, as given by Eq. 62, can be specified, and the location of the shear center relative to the centroidal axis can also be specified. ABAQUS then performs the appropriate transfer of axis calculation internally. Alternately, an equivalent mass density based on the mass moment of inertia about the shear center can be directly entered. The beam examples showed that only the latter approach gave results that correspond to the closed-form solution; hence, this method was adopted when calculating the equivalent beam properties for the I-40 Bridge. Both methods require the location of the shear center to be known *a priori*.

TABLE XVIII

Summary of Input Values for the Simplified Beam Element Model of the I-40 Bridge

PARAMETER	THIN GIRDER	THICK GIRDER
Cross-Sectional Area, A	881.1 $in.^2$	997.6 $in.^2$
Moments of Inertia I_{xx}	1.23 x 10^6 $in.^4$	1.95 x 10^6 $in.^4$
I_{xy}	0.0	0.0
I_{yy}	2.01 x 10^7 $in.^4$	2.42 x 10^7 $in.^4$
Torsional Constant, J	1.577 x 10^4 $in.^4$	1.625 x 10^4 $in.^4$
Shear Center[1], y_0	41.43 in.	59.84in.
Warping Constant, Γ_ω	3.35 x 10^{10} $in.^6$	5.06 x 10^{10} $in.^6$
Sectorial Moment, Γ_0	Approx. 0	Approx. 0
Elastic Modulus[2], E	29 x 10^6 psi	29 x 10^6 psi
Shear Modulus, G	11.54 x 10^6 psi	11.54 x 10^6 psi
Mass Density, μ	1.400 x 10^{-3} lb-$s^2/in.^4$	1.339 x 10^{-3} lb-$s^2/in.^4$

[1]Distance from centroidal axis to shear center axis.
[2]Based on transformation to an equivalent steel cross section.

V. H. Simplified Finite Element Results Compared to Experimental Results

Table XIX compares the resonant frequencies identified by the simplified beam model with those measured on the I-40 Bridge and those calculated with the detailed finite element model BR3W. In Table XIX it can be seen that the percent difference between resonant frequencies calculated with the beam model and the measured resonant frequencies is less than 15% for the first flexural mode and the first two torsional modes. However, for higher-frequency modes the error in the resonant frequencies becomes significantly larger. The boundary conditions specified in the beam model were intended to simulate those in the detailed finite element model BR3W. When compared with the resonant frequencies calculated with this detailed finite element model, the beam model again shows similar comparisons as were observed with the experimental data.

TABLE XIX

Comparison of Simplified-Beam-Model Analytical Modal Analysis Results with Experimental Modal Analysis Results and Detailed Finite Element Analytical Modal Analysis Results

	Resonant Frequency (Hz)				
	Experiment	Beam Model	BR3W	Percent Difference Between Experimental Values and Beam Model	Percent Difference Between BR3W Values and Beam Model
Mode 1 (Bending)	2.48	2.84	2.59	14.5	9.65
Mode 2 (Torsion)	2.96	2.63	2.78	11.1	5.40
Mode 3 (Bending)	3.50	4.36	3.71	24.6	17.5
Mode 4 (Bending)	4.08	5.53	4.32	35.5	28.0
Mode 5 (Torsion)	4.17	4.06	3.96	2.64	2.52
Mode 6 (Torsion)	4.63	5.59	4.50	20.7	24.2
Ave. % Diff.	--	--	--	18.2	14.5

The mode shapes calculated with the simplified beam model are shown in Figs. 68 through 73. In these figures very stiff beam elements with negligible mass have been added perpendicular to the beam elements representing the bridge so that torsional modes can be visualized. A qualitative comparison can be made visually by comparing these modes to those obtained experimentally from ambient tests, shown in Figs. 10 through 15, those from forced vibration tests, Figs. 18 through 23, and with those obtained from the detailed finite element model BR3W shown in Figs. 38 through 43. In all cases it appears that the simplified model is accurately predicting the experimental results and the results obtained with the detailed finite element model. Quantitative comparisons of the mode shapes can be obtained with Eq. 1.

The primary sources for discrepancy between the simple beam model and the detailed finite element model is thought to be the inability to accurately model the three-dimensional boundary conditions with the beam model and the inability to accurately model the influence of the cross-beams. The connections of the plate girders to the piers provide partial restraint of warping which cannot be accurately modeled when only a single beam element is used to simulate the bridge cross section.

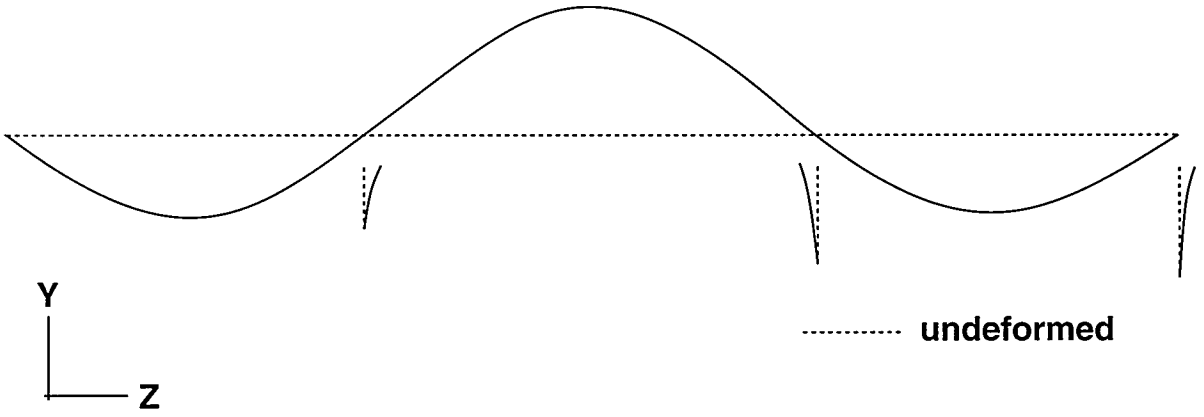

Fig. 68. First flexural mode calculated with the simplified beam finite element model.

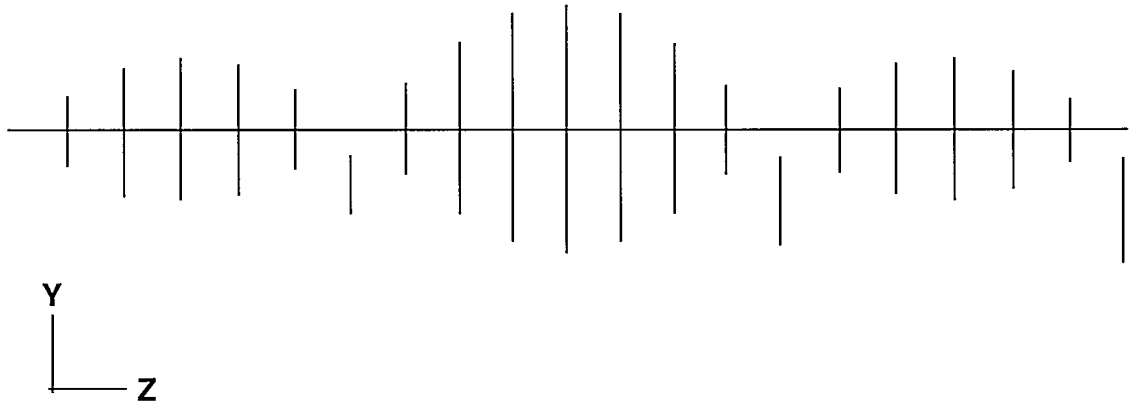

Fig. 69. First torsional mode calculated with simplified beam finite element model.

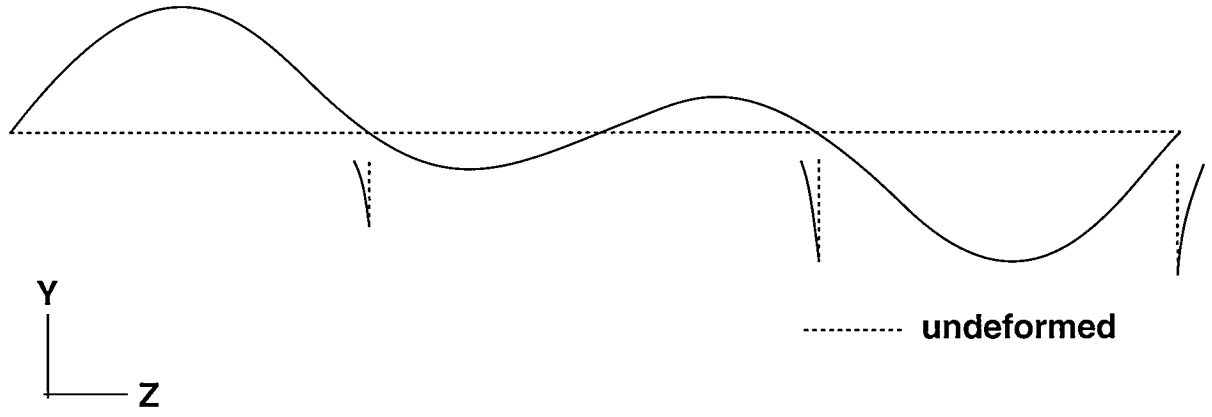

Fig. 70. Second flexural mode calculated with simplified beam finite element model.

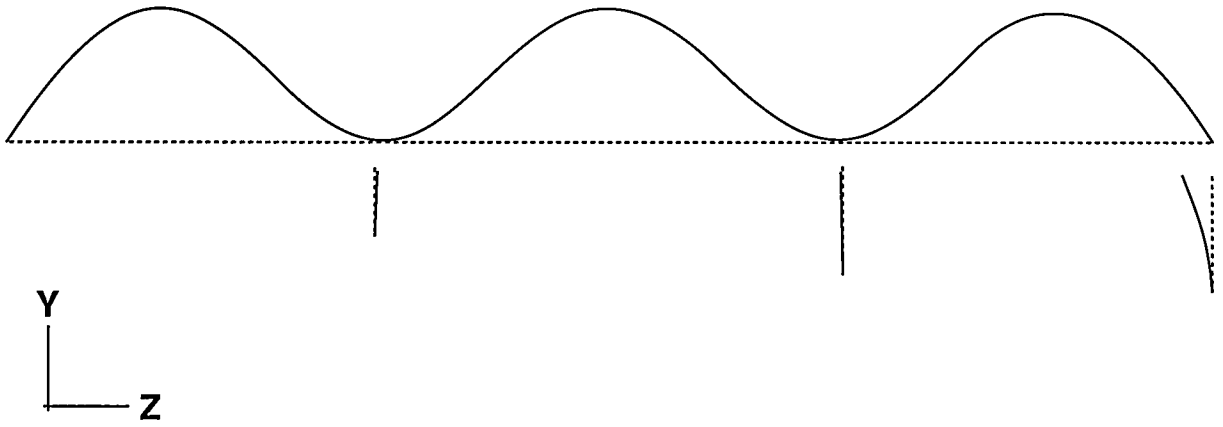

71. Third flexural mode calculated with the simplified beam finite element model.

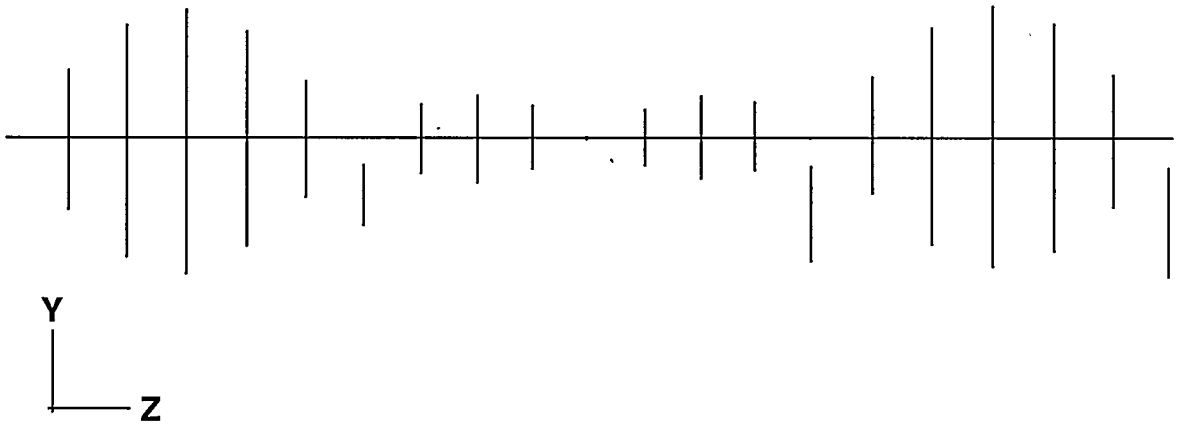

72. Second torsional mode calculated with simplified beam finite element model.

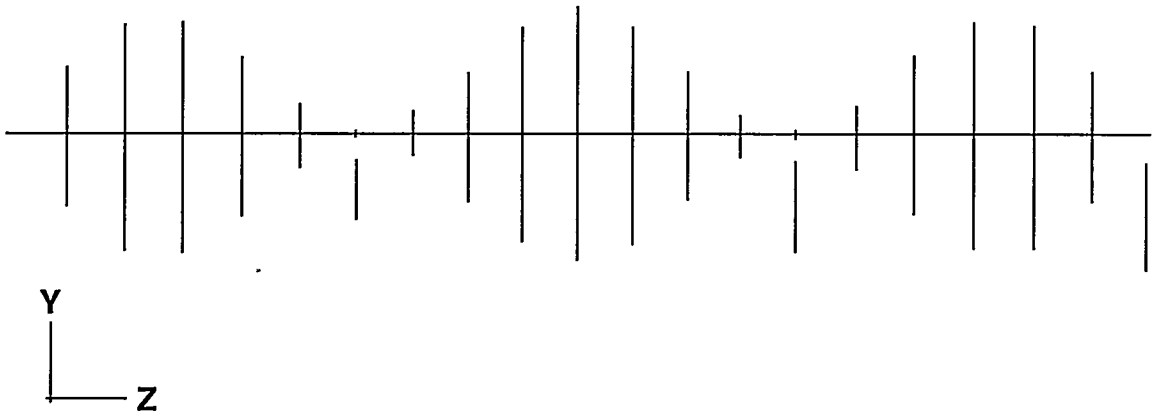

73. Third torsional mode calculated with simplified beam finite element model

VI. SUMMARY & CONCLUSIONS

As part of the research effort to study the effects of damage in plate-girder bridges, 3-D, finite-element models of the first three spans of the I-40 Bridge over the Rio Grande were developed with varying levels of sophistication. The most refined model simulated the bridge substructure above the piers with approximately 35,160 DOFs, and a second model of intermediate refinement had 7032 DOFs. Mode shapes and resonant frequencies identified with these models were identical, and these results were in agreement with the dynamic properties measured on the bridge (typically less than 5% error in resonant frequencies). Calculated mode shapes were shown to be almost identical to those measured on the structure during forced and ambient vibration tests. The calculated mode shapes were found to be particularly sensitive to the boundary conditions used to model the connection of the plate girder to the abutment. Boundary conditions that provide the most accurate model in terms of correlation between measured and calculated resonant frequencies were not the same boundary conditions that provided the best correspondence with calculated and measured mode shapes. The authors felt that adequate agreement with measured dynamic properties was obtained, hence systematic model-updating techniques were not employed.

These numerical models simulate composite action between the concrete deck and the supporting steel girders. The agreement with measured data indicates that the bridge was exhibiting composite action even though shear studs were not present. Differences with measured dynamic properties are attributed to idealization of the boundary conditions, as mentioned above, and the use of generic material properties for the concrete portion of the bridge. Qualitative agreement was obtained with other investigators' analytical results for flexural mode shapes identified for three span bridges.

The 7032 DOF model did not accurately simulate the static deflection that was caused by the dead load of the structure when the final cut was made in the plate girder. The lack of agreement is attributed to localized yielding around the cut that forms a hinge and allows more deformation than a strictly elastic model would predict. Because the modulus of the yielded material does not change, this yielding will not influence the measured resonant frequencies or mode shapes. The 7032 DOF model accurately predicted the measured changes in the dynamic properties that resulted from the damage. To obtain this correspondence with measured data, only the geometry of the model was changed to simulate the damage. The implication is that the actual damage did not introduce a discernible nonlinearity into the structure. Based on the agreement demonstrated between the numerical results and the measured modal results, both in the damaged and undamaged states, the authors feel that the numerical models can now be used to accurately assess various damage-identification algorithms applied to other damage scenarios. The results of such a study will be summarized in a subsequent report

A major portion of this study focused on the development of a simple 1687 DOFs model that uses a single beam element to model the entire bridge cross section. This model required the development of a method for analyzing the torsional properties (shear-center location, torsional constant, warping constant, and sectorial moment) of an open thin-walled cross section of two materials. Numerical procedures summarized in the technical literature, but not widely used, were adopted to calculate these properties. These procedures were first demonstrated on sections where values of torsional properties are tabulated in closed form. Next, they were tested on numerical examples where the beam element formulations could be directly and easily compared to 3-D, shell-element formulations. In all cases the methods used to determine the torsional properties calculated input parameters that accurately predicted 3-D, shell-element results and the closed-form solutions. When calculating equivalent torsional and flexural parameters for the bridge, it became apparent that the stringers add negligible torsional or flexural stiffness to the cross-section. Subsequently, the stringers were neglected when calculating the torsional properties of the cross section.

Because the finite element code used does not allow the polar area moment of inertia to be specified explicitly for beam elements, methods of calculating an equivalent mass density and cross-sectional area had to be developed to accurately model both the flexural and torsional response. This method introduces small (less than 2%) errors into the calculated axial stiffness, but this response is considered of less interest when studying a bridge subjected to typical dynamic loading. Cross-sectional areas of the beam had to be increased to account for the mass of the floor beams and concrete barriers which were not explicitly modeled in the beam element representation of the bridge.

The dynamic properties predicted by this simple model were compared to those measured on the bridge. Mode shapes showed qualitative agreement with the measured mode shapes and mode shapes calculated with the refined 3-D shell-element models. Resonant frequencies were found to have an average of 18.2% difference with measured values and an average of 14.5% difference with those determined by the refined 3-D shell, finite element model. The primary limitation of the simple beam models is their inability to accurately model 3-D boundary conditions such as those that arise from the connections of the plate girders to the piers and their inability to model the cross beams. However, the authors feel that the simple models provide approximations to the dynamic properties that are accurate enough to be useful in preliminary scoping studies such as determining if the bridge has modes of response in the strong motion portion of an earthquake response spectrum. Also, because of the limited numbers of DOFs, this type of model can be exercised extensively on a PC (typical of the computing environment at most smaller consulting engineering firms) to study the response of the bridge to time-varying inputs such as seismic or wind loading.

ACKNOWLEDGMENTS

The authors would like to acknowledge the cooperation and teamwork that was exhibited by all parties involved in the I-40 Bridge project including engineers from Sandia National Laboratory; faculty, technicians, and students from New Mexico State University; faculty from Texas A&M University; numerous people at the New Mexico State Highway and Transportation Department; and the staff at the Alliance for Transportation Research. This research was funded by the Federal Highway Administration.

VII. REFERENCES

Abdel-Ghaffar, A. M. and G. W. Housner (1978) "Ambient Vibration Tests of Suspension Bridge," *ASCE Journal of the Engineering Mechanics Division*, **104**, 983-999.

ABAQUS Theory Manual Version 5.4 (1994) Hibbitt, Karlsson and Sorensen, Inc., Providence RI.

ABAQUS User's Manual Version 5.4 (1994) Hibbitt, Karlsson and Sorensen, Inc., Providence RI.

American Institute of Steel Construction (1989) *Manual of Steel Construction Allowable Stress Design*, 9th Ed., Chicago, IL.

Bishop, R. E. D. and W. G. Price (1977) "Coupled Bending and Twisting of a Timoshenko Beam," *Journal of Sound and Vibration*, **50**, 469-477.

Bishop, R. E. D., S. M. Cannon and S. Miao (1989) "On Coupled Bending and Torsional Vibration of Uniform Beams," *Journal of Sound and Vibration*, **131**, 457-464.

Blevins, R. (1979) *Formulas for Natural Frequencies and Mode Shapes,* Krieger Pub. Co., Malabar, Fl.

Boresi, A. P., O. M. Sidbottom, F. B. Seely, and J. O. Smith (1978), *Advanced Mechanics of Materials*, John Wiley, New York.

Capuani, D., M. Savoia, and F. Laudiero (1992) "A Generalization of the Timoshenko Beam Model for Coupled Vibration Analysis of Thin-Walled Beams," *Earthquake Engineering and Structural Dynamics*, **21**, 859-879.

Carr, J. B. (1969) "The Torsional Vibration of Uniform Thin-Walled Beams of Open Section," *The Aeronautical Journal of the Royal Aeronautical Society*, **73**, 672-674.

Dokumaci, E. (1987) "An Exact Solution for Coupled Bending and Torsional Vibrations of Uniform Beams Having Single Cross-Sectional Symmetry," *Journal of Sound and Vibration*, **119**, 443-449.

Ewins, D. J. (1985), *Modal Testing: Theory and Practice,* John Wiley, New York.

Falco, M. and M. Gasparetto (1973) "Flexural-Torsional Vibrations of Thin-Walled Beams," *Meccanica*, **8**, 181-189.

Farrar, C. R., et al., (1994) "Dynamic Characterization and Damage Detection in the I-40 Bridge over the Rio Grande," Los Alamos National Laboratory report LA-12767-MS.

Galambos, T. V. (1968), *Structural Members and Frames*, Prentice - Hall, Inc., NJ.

Gay D. (1978) "Influence of Secondary Effects on Free Torsional Oscillations of Thin-Walled Open Section Beams," *Journal of Applied Mechanics*, **45**, 681-683.

Gere, J. M. (1954), "Torsional Vibrations of Beams of Thin-Walled Open Section," *Journal of Applied Mechanics*, 381-387.

Gere, J. M., and Y. K. Lin (1958), "Coupled Vibrations of Thin-Walled Beams of Open Cross Section," *Journal of Applied Mechanics*, 373-378.

Gere, J. M. and S. P. Timoshenko (1990), *Mechanics of Materials*, Third Edition, PWS Publishing Co., Boston.

Hallauer, W. L. and R. Y. L. Liu (1982) "Beam Bending-Torsion Dynamic Stiffness Method for Calculation of Exact Vibration Modes," *Journal of Sound and Vibration*, **85**, 105-113.

Heins, C. P., and J. T. C. Kuo (1972a), "Composite Beams in Torsion," *ASCE Journal of the Structural Division,*, **98**, 1105-1117.

Heins, C. P., and J. T. C. Kuo (1972b), "Torsional Properties of Composite Girders," *AISC Engineering Journal*, **9**, 79-85.

Heins, C. P. (1975), *Bending and Torsional Design in Structural Members*, D.C. Heath and Company, Lexington, MA.

James, G. H., T. G. Carne, and J. P. Lauffer (1993) "The Natural Excitation Technique (NExT) for Modal Parameter Extraction From Operating Wind Turbines," Sandia National Laboratory report SAND92-1666.

Krishnan, A. and V. K. Singh (1991) "Some Studies on Vibration of Thin Walled Open Sections," *Journal of Sound and Vibration*, **149**, 297-310.

Kollbrunner, C.F. and K. Basler (1969), *Torsion in Structures*, Springer - Verlag, New York.

Lee, P., D. Ho, and H. Chung (1987) "Static and Dynamic Tests of Concrete Bridge," *ASCE Journal of Structural Engineering,* **113**, No. 1, .

McManus, P. F., and C. G. Culver (1969), "Nonuniform Torsion of Composite Beams," *Journal of the Structural Division, ASCE,* **95**, 1233-1256.

Microsoft EXCEL Version 4.0 (1993), Microsoft Corp.

Oden, J. T., and E. A. Ripperger (1981), "*Mechanics of Elastic Structures*," 2nd Ed., McGraw-Hill Co., NY.

P3/PATRAN User Manual (1992) PDA Engineering, Costa Mesa CA.

Popov, E. P. (1968), *Introduction to Mechanics of Solids*, Prentice-Hall, Inc., Englewood Cliffs, NJ.

Raghavendracharm, M. and A. Aktan (1992) "Flexibility by Multireference Impact Testing for Bridge Diagnostics," *ASCE Journal of Structural Engineering*, **118**, No. 8.

Rao, C. K. (1975) "Nonlinear Torsional Vibrations of Thin-Walled Beams of Open Section," *Journal of Applied Mechanics*, **42**, 240-242.

Stephen, N. G. and J. C. Maltbaek (1979) "The Relationship Between the Centres of Flexure and Twist," *International Journal of Mechanical Sciences*, **21**, 373-377.

Vold, H. and G. F. Rocklin (1982) "The Numerical Implementation of a Multi-Input Modal Estimation Method for Mini-Computers," *Proc. 1st International Modal Analysis Conference*, Kissimmee, FA.

Wekezer, J. W. (1987) "Free Vibration of Thin-Walled Bars with Open Cross Sections, *ASCE Journal of Engineering Mechanics*, **113**, 1441-1453.

APPENDIX A

CALCULATION OF EQUIVALENT BEAM PROPERTIES FOR THE I-40 BRIDGE

A simplified representation of the I-40 Bridge cross section was shown in Fig. 34. The development of equivalent beam properties with which the bridge was modeled are based on this cross-section geometry and the following material properties:

Concrete: $E = 3.6 \times 10^6$ psi,
$G = 1.304 \times 10^6$ psi,
$\mu_c = 2.16 \times 10^{-4}$ lb-s^2/in^4,

Steel: $E = 29 \times 10^6$ psi,
$G = 11.54 \times 10^6$ psi, and
$\mu_s = 7.48 \times 10^{-4}$ lb-s^2/in^4.

These properties yield a modular ratio of 8.05. The concrete is assumed uncracked and steel reinforcement is neglected. Two different cross sections are considered and denoted as the "thin flange" and the "thick flange." These cross sections correspond to the different plate-girder flange dimensions that are present along the length of the bridge as shown in Fig. 34. Standard procedures are used to determine the following beam bending properties of the composite cross section:

1. A transformed cross section in terms of steel,
2. The centroid of the transformed section, and
3. Transformed area moments of inertia about this centroidal axis.

A.1 Equivalent Cross Section in Steel and Centroid Location

Cross-section properties of the steel members making up the bridge cross section are listed in Table A-1.

TABLE A-1

Cross-Section Properties of Steel Members

Property	21WF62	Thin-Flange Girder	Thick-Flange Girder
Area (in^2)	18.2	108	171
I_{xx} (in^4)	1330	2.87×10^5	5.28×10^5
I_{yy} (in^4)	53.1	2.32×10^3	6.05×10^3
depth, d, (in.)	21.0	120	120
Flange thickness, t_f, (in.)	0.615	1.50	2.625
Web thickness, t_w, (in.)	0.400	0.375	0.375
flange width, b, (in.)	8.24	21.0	24.0

To develop an equivalent bending cross section in steel, the width of the concrete slab is divided by the modular ratio yielding a transformed slab 8.7 in. thick and 64.8 in. wide for bending about the X-axis shown in Fig. 34, and a slab 1.08 in. thick and 522 in. wide for bending about the Y-axis. The transformed areas and corresponding vertical distances from the reference axis shown in Fig. 34 to the centroids of the respective transformed areas are listed in Table A-2.

TABLE A-2

Transformed Areas and Centroids

Area	Transformed Area, (in^2)	Y-Distance to Centroid, (in.)	X-Distance to Centroid, (in.)
Thin Flange Girder	108	60	180
Thick Flange Girder	171	60	180
21WF62	18.2	109.5	0, 90[2]
Concrete Slab	564[1]	124.35	0

[1] Transformed Value
[2] One stringer is on the centroidal axis, the other two are 90 in. from the centroidal axis.

The resulting centroid location, $\overline{Y}$, is obtained from the familiar relation derived in most statics texts,

$$\overline{Y} = \frac{\sum A_i \overline{Y}_i}{\sum A_i}, \tag{A-1}$$

where A_i is the cross-sectional area of the ith element forming the beam, and $\overline{Y}_i$ is the centroid location of the ith element.

Based on the origin shown in Fig. 34 and the values listed in Table A-1, the centroidal locations for the transformed areas are

Thin-Flange Girder: $\overline{Y} = 106.7$ in.

Thick-Flange Girder: $\overline{Y} = 100.6$ in.

Because of the vertical axis of symmetry, $\overline{X} = 0$.

A. 2 Moments of Inertia of the Transformed Section

Area moments of inertia are determined in the conventional manner about the centroidal axes for both the thin- and thick-flange sections listed above. The calculation is done for both horizontal and vertical centroidal axes of the transformed section. The contribution to the moment of inertia about a given centroidal axis for each area is determined using the notation shown in Figure A-1. The general equation, from the Parallel Axis Theorem, is

$$I_{\beta\beta} = I_{00} + Ad_{0\beta}^2, \tag{A-2}$$

where $I_{\beta\beta}$ is the moment of inertia of area A about an axis, β–β, I_{00} is the moment of inertia of area A about its local centroidal axis, 0-0 , and d is the distance between the 0 and β axis. For rectangular sections,

$$I_{00} = \frac{bd^3}{12}, \tag{A-3}$$

where b is the dimension parallel to the 00 axis and h is the corresponding dimension perpendicular to the 00 axis. For I-beam shapes, I_{00} takes on the values

$$I_{00} = \frac{t_w(d-2t_f)^3}{12} + 2\left(\frac{bt_f^3}{12} + bt_f\left(\frac{d}{2} - \frac{t_f}{2}\right)^2\right) \tag{A-4}$$

for the moment of inertia about the strong axis, and

$$I_{00} = \frac{(d-2t_f)t_w^3}{12} + 2\left(\frac{t_f b^3}{12}\right) \tag{A-5}$$

for the moment of inertia about the weak axis, with notation as indicated in Table A-1. Results are presented in Table A-3 for the cross sections with thin and thick girders, respectively.

TABLE A-3

Area Moments of Inertia About Local Centroid and Distance to Transformed Cross-Section Centroid

Area	Moment of Inertia about element centroidal axis I_{XX}, (in^4)	Moment of Inertia about element centroidal axis I_{YY}, (in^4)	X-Distance to Transformed Centroid (in.)	Y-Distance to Transformed Thin-Flange Centroid (in.)	Y-Distance to Transformed Thick-Flange Centroid (in.)
Transformed Slab[1]	3.56×10^3	12.8×10^6	0	-17.65	-23.75
21WF62[2]	1.33×10^3	53.1	0, 90	-2.8	-8.9
Thin Girder	2.87×10^5	2.32×10^3	180	46.7	--
Thick Girder	5.28×10^5	6.05×10^3	180	--	40.6

[1] Based on transformed area
[2] Moments of inertia are taken from the AISC Manual

Total moments of inertia about the centroid of the transformed section are

1. Cross section with thin-flange girders:
   $I_{xx} = 1.23 \times 10^6$ in^4
   $I_{yy} = 20.1 \times 10^6$ in^4

2. Cross section with thick-flange girders:
   $I_{xx} = 1.95 \times 10^6$ in^4
   $I_{yy} = 24.2 \times 10^6$ in^4

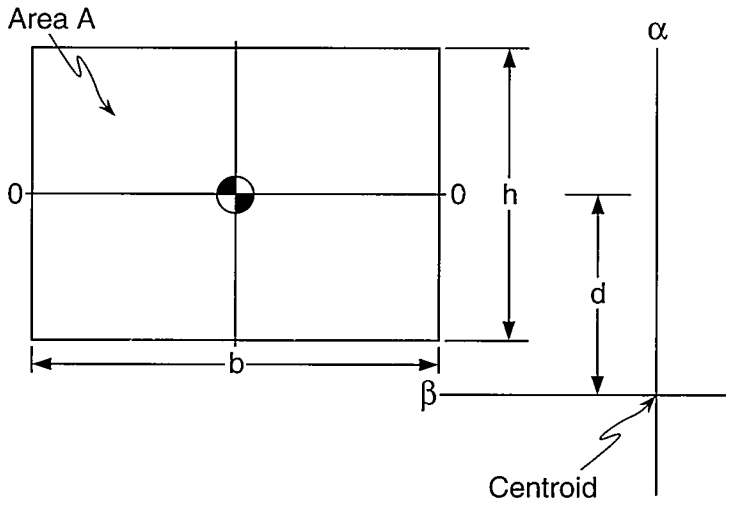

Fig. A-1. Calculation of moments of inertia.

A. 3. Torsional Constant of the Composite Cross Section

The equivalent torsional constant of the composite cross section, J_{eq}, is calculated as

$$J_{eq} = \frac{\sum_{i=1}^{n} G_i J_i}{G_T}, \tag{A-6}$$

where G_i is the shear modulus of the ith thin section forming the cross section, G_T is the shear modulus of the material that is being used to represent the transformed section, and

$$J_i = \frac{1}{3} b_i t_i^3, \tag{A-7}$$

where b_i is the length of the thin section and t_i is its width. The factor of 1/3 is an approximation and sufficiently accurate for sections where the ratio of b_i to t_i is greater than 10. This approximation is valid for all members forming the I-40 Bridge cross section. Table A-4 summarizes the torsional constant for the various members forming the I-40 Bridge cross section.

TABLE A-4

Torsional Constants and Shear Moduli for Members Making up the I-40 Bridge Cross Section

Area	Torsional Constant, J_i, (in^4)	Shear Modulus, G_i, (psi)
Concrete Slab	11.5×10^5	1.576×10^6
21WF62[1]	1.83	11.54×10^6
Thin Girder	49.36	11.54×10^6
Thick Girder	291.5	11.54×10^6

[1] Torsional constant was listed in AISC Manual

The values listed in Table A-4 yield the following torsional constants when the transformed section is expressed in terms of steel material properties (that is, $G_T = 11.54 \times 10^6$ psi)

1. Cross section with thin flange girders:
   $J = 1.577 \times 10^4$ in^4,

2. Cross section with thick flange girders:
   $J = 1.625 \times 10^4$ in^4.

It should be noted that the torsional constant is independent of the orientation of the members forming the cross section.

A. 4. Equivalent Mass Density for the Cross Section

An equivalent mass density, μ_{eq}, is calculated such that the polar mass moment of inertia about the shear center is accurate. A confounding factor in the calculation of this parameter is that the computer code being used does not specifically allow the polar area moment of inertia to be entered, but instead calculates this parameter as the sum of I_{xx} and I_{yy} . The equivalent mass density is given by

$$\mu_{eq} = \frac{\sum \mu_i I_{p_i}}{I_{xx} + I_{yy}}, \tag{A-8}$$

where μ_i is the mass density of the ith section forming the bridge cross section, and I_{p_i} is the polar moment of inertia of the ith section about the shear center. Table A-5 lists the polar moment of inertia about the shear center for the various sections forming the bridge cross section.

TABLE A-5

Parameters Needed to Calculate the Equivalent Mass Density for the I-40 Bridge Cross Section

Area	Moment of Inertia about local centroid, I_{XX}, (in^4)	Moment of Inertia about local centroid, I_{YY}, (in^4)	Y-Distance to Shear Center[1] (in.)	Polar Moment of Inertia, I_p, About the Shear Center (in^4)	Mass Density ($lb\text{-}s^2/in^4$)
Concrete Slab (Not Transformed)	28.6×10^3	1.03×10^8	23.63 (thin), 33.53 (thick)	1.06×10^8 1.08×10^8	2.16×10^{-4}
21WF62[2]	1.33×10^3	53.1	34.67 (thin), 44.57 (thick)	3.65×10^5 4.08×10^5	7.48×10^{-4}
Thin Girder[3]	2.87×10^5	2.32×10^3	84.17	9.11×10^6	7.48×10^{-4}
Thick Girder[3]	5.28×10^5	6.05×10^3	94.07	15.2×10^6	7.48×10^{-4}

[1] Location of the shear center was determined by numerical procedures, two values correspond to thin- and thick-flange sections, respectively.
[2] Polar moment of inertia is the total for all three stringers.
[3] Polar moment of inertia is the total for both plate girders.

The values of I_{xx} and I_{yy} listed in Section A-2 above yield the following equivalent mass densities for the various bridge cross-section geometries:

1. Cross section with thin-flange girders:
   $\mu_{eq} = 1.400 \times 10^{-3}$ lb-s^2/in^4,

2. Cross section with thick-flange girders:
   $\mu_{eq} = 1.339 \times 10^{-3}$ lb-s^2/in^4.

A. 5. Cross-Sectional Area

To make the equivalent mass density that was developed based on torsional considerations also appropriate for calculating the flexural response, the area of the beam element representing the bridge cross section, A_{eq}, must be adjusted such that

$$A_{eq} = \frac{\mu_s A_s + \mu_c A_c}{\mu_{eq}}, \tag{A-9}$$

where A_s is the area of steel forming the cross section and A_c is the corresponding area of concrete. Noting that A_c is 4541 in^2 and using the values for A_s, μ_s, μ_c, and μ_{eq} listed above, the following values are obtained for A_{eq}

1. Cross section with thin-flange girders:
   $A_{eq} = 845.2$ in^4,

2. Cross section with thick-flange girders:
   $A_{eq} = 954.1$ in^4.

The actual areas used in the beam model have been increased approximately 4% to account for the mass of the floor beams, which have not been explicitly modeled in this simple representation of the bridge. These areas will introduce slight errors (less than 2% for the thin-flange section) for the axial stiffness of the bridge, but the axial response is generally of limited interest; hence, this error is considered acceptable. At this point, all necessary parameters needed for an equivalent beam representation of the I-40 Bridge cross section have been defined.

APPENDIX B

CALCULATION OF SHEAR-CENTER LOCATION FOR THE I-40 BRIDGE

A detailed summary of the closed-form and numerical methods to locate the shear center of the I-40 Bridge approximation are summarized in this Appendix. The nomenclature for the various segments of the I-40 Bridge approximation is shown in Fig. B-1, and the shear stress resultants are shown in Fig. B-2. First, the closed-form solution for the shear-center location is determined following the steps listed in Section V. B. 2. The resultant shear forces in the various segments making up the approximation to the I-40 Bridge are

SEGMENT A-B: (See Fig. B-1)

$$Q_y = \bar{X}A = st_1\left(\frac{h}{2} - a + \frac{s}{2}\right), \qquad \text{(First moment of area)} \qquad \text{(B-1)}$$

$$\tau = \frac{V_x Q_y}{I_y t_1} = s\left(\frac{h}{2} - a + \frac{s}{2}\right)\frac{V_x}{I_y}, \qquad \text{(Shear stress)} \qquad \text{(B-2)}$$

$$\tau_{A=0}, \qquad \text{(B-3)}$$

$$\tau_B = \frac{a}{2}(h-a)\frac{V_x}{I_y}, \text{ and} \qquad \text{(B-4)}$$

$$F_1 = \int_o^a \tau t_1 ds = \frac{a^2 t_1}{12 I_y}(3h - 4a)V_x. \qquad \text{(Resultant force)} \qquad \text{(B-5)}$$

SEGMENT A'B: (See FIG. B-1)

$$Q_y = st_1\left(\frac{h}{2} + a - \frac{s}{2}\right), \qquad \text{(B-6)}$$

$$\tau = s\left(\frac{h}{2} + a - \frac{s}{2}\right)\frac{V_x}{I_y}, \qquad \text{(B-7)}$$

$$\tau_{A'} = 0, \qquad \text{(B-8)}$$

$$\tau_B = \frac{a}{2}(h+a)\frac{V_x}{I_y}\text{ , and} \tag{B-9}$$

$$F_2 = \int_o^a \tau t_1 ds = \frac{a^2 t_1}{12 I_y}(3h+4a)V_x\text{ .} \tag{B-10}$$

SEGMENT B-C:

Shear flow from segments AB and A'B add.

$$q_{BC} = q_{AB} + q_{A'B} = t_1\tau_{B_{AB}} + t_1\tau_{B_{A'B}} = t_2\tau_{B_{BC}}\text{.} \tag{B-11}$$

Solving for $\tau_{B_{BC}}$ and substituting previously determined results,

$$\tau_{B_{BC}} = \frac{t_1}{t_2}\frac{V_x}{I_y}ah\text{ ,} \tag{B-12}$$

$$Q_c = at_1h + \frac{bt_2h}{2}\text{ ,} \tag{B-13}$$

$$\tau_c = \frac{V_x Q_c}{I_y t_2} = \left[a\frac{t_1}{t_2}h + \frac{bh}{2}\right]\frac{V_x}{I_y}\text{ ,} \tag{B-14}$$

$$F_3 = \frac{1}{2}\left(\tau_{B_{BC}} + \tau_C\right)t_2 b\text{ , and} \tag{B-15}$$

$$F_3 = \frac{t_2 b V_x}{2I_y}\left[\frac{t_1}{t_2}ah + \frac{at_1h}{t_2} + \frac{bh}{2}\right]\text{.} \tag{B-16}$$

Resultant forces are shown in Fig. B-2, where symmetry has been invoked.

From force equilibrium,

$$V = F_6 + 2F_2 - 2F_1\text{ .} \tag{B-17}$$

Substituting Eqs. B-5 and B-10 into Eq. B-17 yields

$$F_6 = V\left[1-\frac{4a^3t_1}{3I_y}\right]. \tag{B-18}$$

Summing moments about the yet unknown position of the shear center (S.C., Fig. B-2), it is readily shown that

$$e = \frac{1}{F_6}\left[F_3h+2(F_1-F_2)(b+e)\right]. \tag{B-19}$$

Substituting Eqs. B-5, B-10, B-16, and B-18 into Eq. B-19, and noting that the moment of inertia about the axis of symmetry is

$$I_y = \frac{1}{12}t_3(h+2c\ )^3+\frac{bt_2h^2}{2}+\frac{4t_1}{3}\frac{a^3}{}+at_1h^2\ , \tag{B-20}$$

the shear-center location relative to the center of the transformed concrete slab is

$$e = \frac{1}{6I_y}\left[\ 3t_2bh^2\left\{2a\frac{t_1}{t_2}+\frac{b}{2}\right\}-8ba^3t_1\ \right]. \tag{B-21}$$

The geometry of the cross section can be simplified to that of a channel section if the following substitution are made into Eqs. B-20 and B-21:

$t_1 = 0$, $t_2 = t_f$, $t_3 = t_w$, $c = 0$, and $a = 0$.

Eq. B-21 then reduces to

$$e = \frac{3t_fb^2}{t_wh+6bt_f}. \tag{B-22}$$

This result is identical to the shear-center location of a channel given by Gere and Timoshenko (1990), and therefore, provides at least a partial check of Eq. B-21.

The following numerical values of the various parameters apply to the two I-40 Bridge cross sections (thick-flange, thin-flange):

$$\tau_1 = \begin{cases} 1.50 \text{ in.(thin-flange)} \\ 2.625 \text{ in.(thick-flange)} \end{cases},$$

$t_2 = 0.375$ in. ,

$t_3 = 1.08$ in. ,

$$a = \begin{cases} 10.5 \text{ in. (thin-flange)} \\ 12.0 \text{ in. (thick-flange)} \end{cases},$$

$h = 360$ in. ,

$b = 120$ in. , and

$c = 81.0$ in.

The corresponding shear-center locations, e, measured from the center of the transformed concrete slab as shown in Fig. B-2 are

thin-flange: $e = 23.63$ in., and

thick-flange: $e = 33.55$ in.

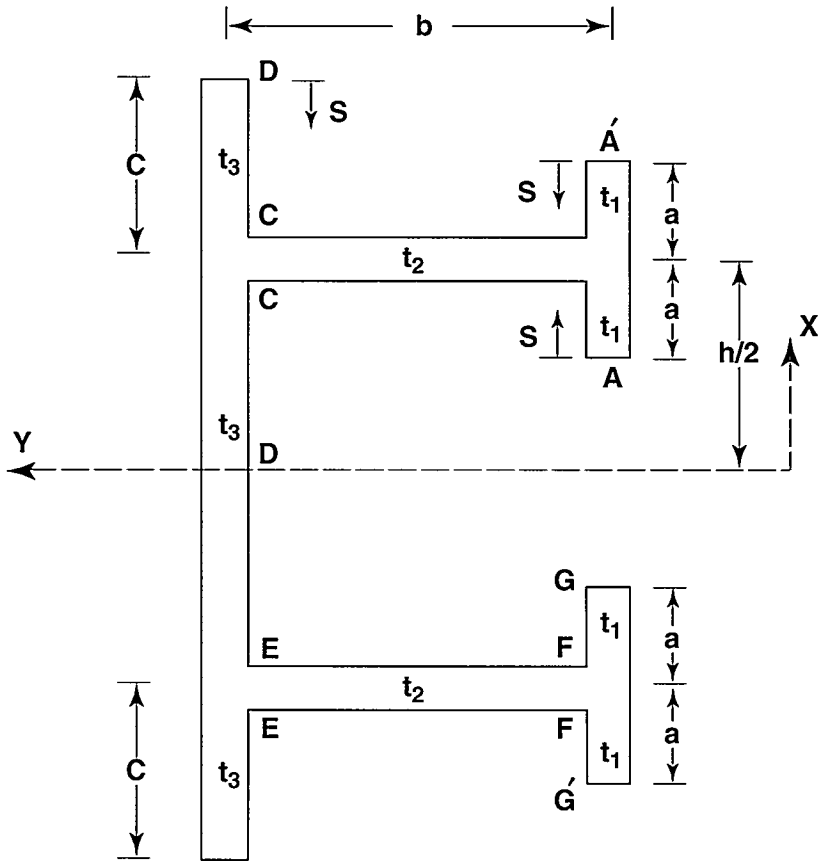

Fig. B-1. Nomenclature for shear center determination.

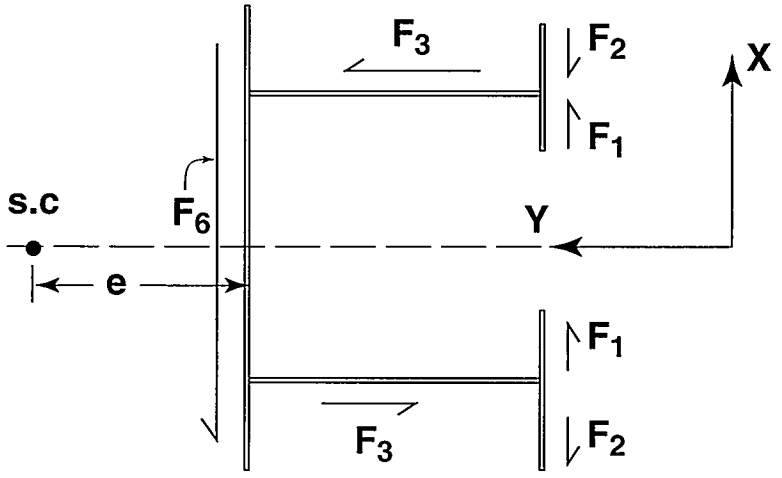

Fig. B-2. Shear stress resultants in the approximation of the I-40 Bridge cross section.

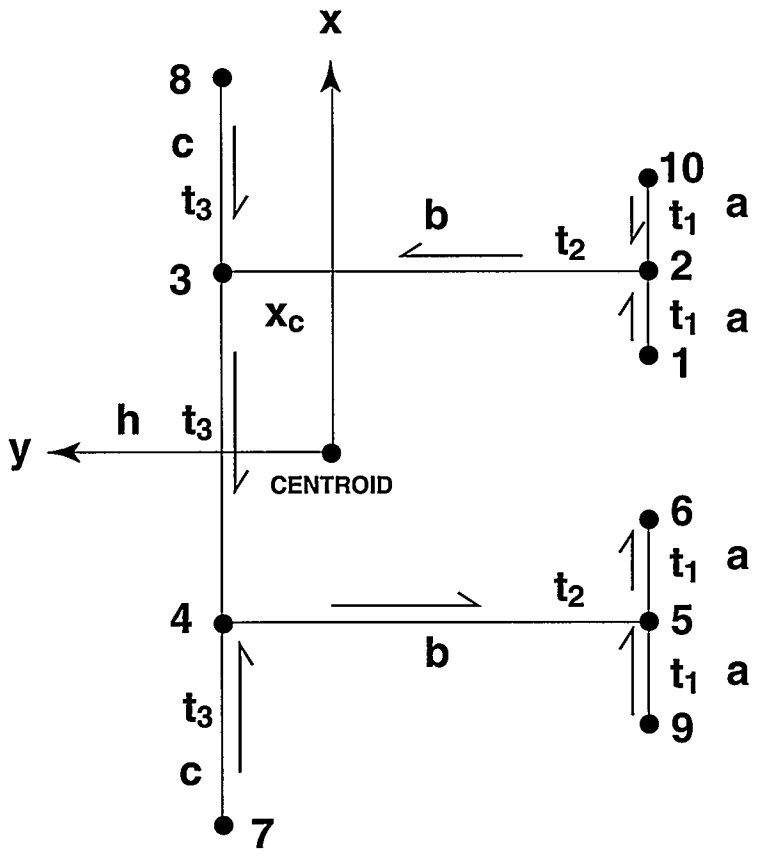

Fig. B-3. Shear flow directions modified for incorporation with Heins' numerical method.

Next, the shear center for the I-40 Bridge transformed cross section is located using the numerical method of Heins (1975). Determination of the shear centers for the thick flange and thin flange I-40 Bridge cross sections follows the procedures outlined in Section V. B. 3. Referring to Fig. B-3, the principal path coordinate, s, is assumed to start at point 1, proceeding along the path 1-2-3-4-5-6. Remaining branchings (10-2, 8-3, 7-4, and 9-5) are calculated separately starting from the free ends and proceeding toward the respective common branch points. Thus an additional path coordinate si is introduced at the free end of each of these branchings. The procedure is to calculate the unit warping constant, w, first along the principal path coordinate. Then the distribution along the branchings is calculated backwards from the known values at the junctions.

The directions of the "flow" for the numerical evaluation shown in Fig. B-3 do not in all cases agree with the shear flow shown in Fig. B-2. Numerical values for the geometric parameters of the I-40 Bridge shown in Fig. B-3 are

a = 10.5 in (thin-flange)
a = 12.0 in. (thick-flange)
t_1 = 1.50 in. (thin-flange)
t_1 = 2.625 in. (thick-flange)
t_2 = 0.375 in
t_3 = 1.08 in (transformed)
h = 360 in.
b = 120 in
c = 81.0 in.

The centroid locations, $\overline{Y}$, relative to the center of the transformed concrete slab for thick- and thin-flange simplified cross sections (stringers and top flange of plate girders neglected) are determined using Eq. A-1. Results for the two cross sections are

Thin-flange cross section: $\overline{Y}$ = 17.80 in.

Thick-flange cross section: $\overline{Y}$ = 26.31 in.

Positive values are actually measured in the negative Y direction shown in Figs. B-1 through B-3.

The Heins tabular procedure for the thin I-40 Bridge cross sections are shown in Tables B-1 and B-2 , for the thin and thick cross sections. Definitions for the column entries and calculations are identical to those described in Section V. B. 3. Note that again the values of the unit warping constant, w, in column 6 are calculated from point 1 to point 6, that is, downward, whereas values for points 7, 8, 9, and 10 are calculated upward in the table from known values. For example, ω_{10} is calculated from the known value ω_2 by subtracting ω_{10} (column 5) from ω_2. Further, the value $\rho_{10\text{-}2}$ is negative because the centroid is to the right as one proceeds along $L_{10\text{-}2}$ from point 10 to point 2.

Final results for the shear-center location are shown at the bottoms of the respective tables. In both cases, moments of inertia, I_y, measured about the centroidal y axis calculated numerically using Eq. 38 agree with conventional hand calculations. The shear-center locations, y_0, measured from the centroid are

Thin-flange section: y_0 = -41.43 in, and

Thick-flange section: y_0 = -59.84 in.

TABLE B-1
Spreadsheet for Numerical Calculation of the I-40 Bridge Thin-Flange Section Shear Center Location

SHEAR CENTER DETERMINATION FOR I-40 BRIDGE THIN CROSS SECTION USING HEINS' METHOD														
POINT	X	Lij	RHOij	Wij	Wi	Tij	Tij Lij	Wi Xi	Wj Xj	Wi Xj	Wj Xi	SUM 1	SUM 2	Iy
1	169.5				0									
1--2		10.5	102.2	1073.1		1.5	15.75	0	193158	0	181890.5	3042239	2864775	1443334
2	180				1073.1									
2--3		120	180	21600		0.375	45	193158	4081158	193158	4081158	1.92E+08	1.92E+08	4374000
3	180				22673.1									
3--4		360	17.8	6408		1.08	388.8	4081158	-5234598	-4081158	5234598	-4.5E+08	4.48E+08	12597120
4	-180				29081.1									
4--5		120	180	21600		0.375	45	-5234598	-9122598	-5234598	-9122598	-6.5E+08	-6.5E+08	4374000
5	-180				50681.1									
5--6		10.5	102.2	1073.1		1.5	15.75	-9122598	-8772337	-8590446	-9315756	-2.8E+08	-2.8E+08	1443334
6	-169.5				51754.2									
7	-261				30522.9									
7--4		81	-17.8	-1441.8		1.08	87.48	-7966477	-5234598	-5494122	-7590167	-1.2E+09	-1.1E+09	12903387
4	-180				29081.1									
8	261				21231.3									
8--3		81	17.8	1441.8		1.08	87.48	5541369	4081158	3821634	5917679	8.42E+08	8.52E+08	12903387
3	180				22673.1									
9	-190.5				49608									
9--5		10.5	102.2	1073.1		1.5	15.75	-9450324	-9122598	-8929440	-9654750	-2.9E+08	-2.9E+08	1621939
5	-180				50681.1									
10	190.5				2146.2									
10--2		10.5	-102.2	-1073.1		1.5	15.75	408851.1	193158	386316	204425.6	9481643	9304179	1621939
2	180				1073.1							-1.8E+09	-8.6E+08	53282441
					Iy=	17760814		Iwx=	-7.4E+08		Yo=	-41.4265		

TABLE B-2

Spreadsheet for Numerical Calculation of the I-40 Bridge Thick-Flange Section Shear Center Location

SHEAR CENTER DETERMINATION FOR I-40 BRIDGE THICK CROSS SECTION USING HEINS' METHOD														
POINT	X	Lij	RHOij	Wij	Wi	Tij	Tij Lij	Wi Xi	Wj Xj	Wi Xj	Wj Xi	SUM 1	SUM 2	Iy
1	168				0									
1--2		12	93.69	1124.28		2.625	31.5	0	202370.4	0	188879	6374668	5949690	2862216
2	180				1124.28									
2--3		120	180	21600		0.375	45	202370.4	4090370	202370.4	4090370	1.93E+08	1.93E+08	4374000
3	180				22724.28									
3--4		360	26.31	9471.6		1.08	388.8	4090370	-5795258	-4090370	5795258	-6.6E+08	6.63E+08	12597120
4	-180				32195.88									
4--5		120	180	21600		0.375	45	-5795258	-9683258	-5795258	-9683258	-7E+08	-7E+08	4374000
5	-180				53795.88									
5--6		12	93.69	1124.28		2.625	31.5	-9683258	-9226587	-9037708	-9885629	-6E+08	-6E+08	2862216
6	-168				54920.16									
7	-261				34326.99									
7--4		81	-26.31	-2131.11		1.08	87.48	-8959344	-5795258	-6178858	-8403125	-1.3E+09	-1.3E+09	12903387
4	-180				32195.88									
8	261				20593.17									
8--3		81	26.31	2131.11		1.08	87.48	5374817	4090370	3706771	5931037	8.28E+08	8.43E+08	12903387
3	180				22724.28									
9	-192				52671.6									
9--5		12	93.69	1124.28		2.625	31.5	-1E+07	-9683258	-9480888	-1E+07	-6.2E+08	-6.2E+08	3270456
5	-180				53795.88									
10	192				2248.56									
10--2		12	-93.69	-1124.28		2.625	31.5	431723.5	202370.4	404740.8	215861.8	19973958	19548981	3270456
2	180				1124.28							-2.8E+09	-1.5E+09	59417239
					Iy=	19805746		Iwx=	-1.2E+09		Yo=	-59.8418		

Negative values correspond to the positive Y direction shown in Figs. B-1 through B-3. Using the centroid locations given above, the shear-center locations measured from the center of the transformed slab are

Thin-flange section: $e = 23.66$ in, and

Thick-flange section: $e = 33.53$ in.

Here, positive values correspond to the positive Y direction shown in Figs. B-1 through B-3. These values correspond almost identically to the shear-center locations determined previously in this Appendix using the closed form 'strength of materials' approach .

Finally, Table B-3 summarizes the calculation of the shear-center location for the thin-flange section with the stringers included. The resulting shear-center location measured from the centroid is

Thin-flange section: $y_0 = -41.43$ in,

and measured from the center of the transformed slab the shear-center location is

Thin-flange section: $e = 23.63$ in.

The numerical procedure suggested by Heins provides a general and easily implemented method for calculating the shear-center location of an open section made up of thin rectangular members with different material properties.

TABLE B-3

Spreadsheet for Numerical Calculation of the I-40 Bridge Thin-Flange Section (Including Stringers)
Shear Center Location

SHEAR CENTER DETERMINATION FOR I-40 BRIDGE THIN CROSS SECTION USING HEINS' METHOD- STRINGERS ADDED														
POINT	X	Lij	RHOij	Wij	Wi	Tij	Tij Lij	Wi Xi	WjXj	Wi Xj	Wj Xi	SUM 1	SUM 2	Iy
1	169.5				0									
1--2		10.5	102.2	1073.1		1.5	15.75	0	193158	0	181890.5	3042239	2864775	1443334
2	180				1073.1									
2		120	180	21600		0.375	45	193158	4081158	193158	4081158	1.92E+08	1.92E+08	4374000
1--3	180				22673.1									
3		90	17.8	1602		1.08	97.2	4081158	2184759	2040579	4369518	6.09E+08	6.23E+08	5511240
3	90				24275.1									
1--4		90	17.8	1602		1.08	97.2	2184759	0	0	2328939	2.12E+08	2.26E+08	787320
4	0				25877.1									
4		90	17.8	1602		1.08	97.2	0	-2473119	-2328939	0	-2.4E+08	-2.3E+08	787320
1--5	-90				27479.1									
5		90	17.8	1602		1.08	97.2	-2473119	-5234598	-4946238	-2617299	-7.5E+08	-7.4E+08	5511240
5	-180				29081.1									
1--6		120	180	21600		0.375	45	-5234598	-9122598	-5234598	-9122598	-6.5E+08	-6.5E+08	4374000
6	-180				50681.1									
6		10.5	102.2	1073.1		1.5	15.75	-9122598	-8772337	-8590446	-9315756	-2.8E+08	-2.8E+08	1443334
1--7	-169.5				51754.2									
7														
7	-261				30522.9									
1--8		81	-17.8	-1441.8		1.08	87.48	-7966477	-5234598	-5494122	-7590167	-1.2E+09	-1.1E+09	12903387
8	-180				29081.1									
8														
1--9	261				21231.3									
9		81	17.8	1441.8		1.08	87.48	5541369	4081158	3821634	5917679	8.42E+08	8.52E+08	12903387
9	180				22673.1									
1--10														
10	-190.5				49608									
10		10.5	102.2	1073.1		1.5	15.75	-9450324	-9122598	-8929440	-9654750	-2.9E+08	-2.9E+08	1621939
1--11	-180				50681.1									
11														
11	190.5				2146.2									
1--12		10.5	-102.2	-1073.1		1.5	15.75	408851.1	193158	386316	204425.6	9481643	9304179	1621939
12	180				1073.1									
12														
1--13	90				22385.1									
13		21	90	1890		0.4	8.4	2014659	2184759	2014659	2184759	35275111	35275111	204120
13	90				24275.1									

TABLE B-3 (Continued)
Spreadsheet for Numerical Calculation of the I-40 Bridge Thin-Flange Section (Including Stringers)
Shear Center Location

SHEAR CENTER DETERMINATION FOR I-40 BRIDGE THIN CROSS SECTION USING HEINS' METHOD- STRINGERS ADDED														
POINT	X	Lij	RHOij	Wij	Wi	Tij	Tij Lij	Wi Xi	WjXj	Wi Xj	Wj Xi	SUM 1	SUM 2	Iy
1--14														
14	0				25877.1									
14		21	0			0.4	8.4	0	0	0	0	0	0	0
1--15	0				25877.1									
15														
15	-90				29369.1									
1--16		21	-90	-1890		0.4	8.4	-2643219	-2473119	-2643219	-2473119	-4.3E+07	-4.3E+07	204120
16	-90				27479.1									
16														
1--17	94.1				22398.22									
17		4.1	-3.2	-13.12		0.615	2.5215	2107673	2014659	2015840	2106438	10394459	10394323	64106.14
17	90				22385.1									
1--18														
18	85.9				22371.98									
18		4.1	3.2	13.12		0.615	2.5215	1921753	2014659	2013478	1922880	9925663	9925527	58523.54
1--19	90				22385.1									
19														
19	4.1				25890.22									
1--20		4.1	-3.2	-13.12		0.615	2.5215	106149.9	0	0	106096.1	267657	267521.3	42.38642
20	0				25877.1									
20														
1--21	-4.1				25863.98									
21		4.1	3.2	13.12		0.615	2.5215	-106042	0	0	-106096	-267386	-267521	42.38642
21	0				25877.1									
1--22														
22	-85.9				29382.22									
22		4.1	-3.2	-13.12		0.615	2.5215	-2523933	-2643219	-2644400	-2522806	-1.3E+07	-1.3E+07	58523.54
1--23	-90				29369.1									
23														
23	-94.1				29355.98									
1--24		4.1	3.2	13.12		0.615	2.5215	-2762398	-2643219	-2642038	-2763632	-1.4E+07	-1.4E+07	64106.14
24	-90				29369.1							-1.5E+09	-1.4E+09	53936025
				Iy=	17978675		Iwx=	-7.4E+08		Yo=	-41.315			

APPENDIX C:

CALCULATION OF THE WARPING CONSTANT AND SECTORIAL MOMENT FOR THE I-40 BRIDGE

Calculations of the warping constant and statical warping moment (or sectorial moment) are presented in Table C-1 for the thin I-40 Bridge cross section and in Table C-2 for the thick cross section. These calculations are based on the idealized cross section shown in Fig. 53. Results are indicated at the bottom of each table. In Table C-3 the stringers are added to the idealized cross section to examine their influence on the calculated warping constant and statical warping moment. Again, it is seen that the stringers have negligible effect on the value of the warping constant and sectorial moment. The shear-center location and identification of points and elements of the cross section are shown in Fig. C-1.

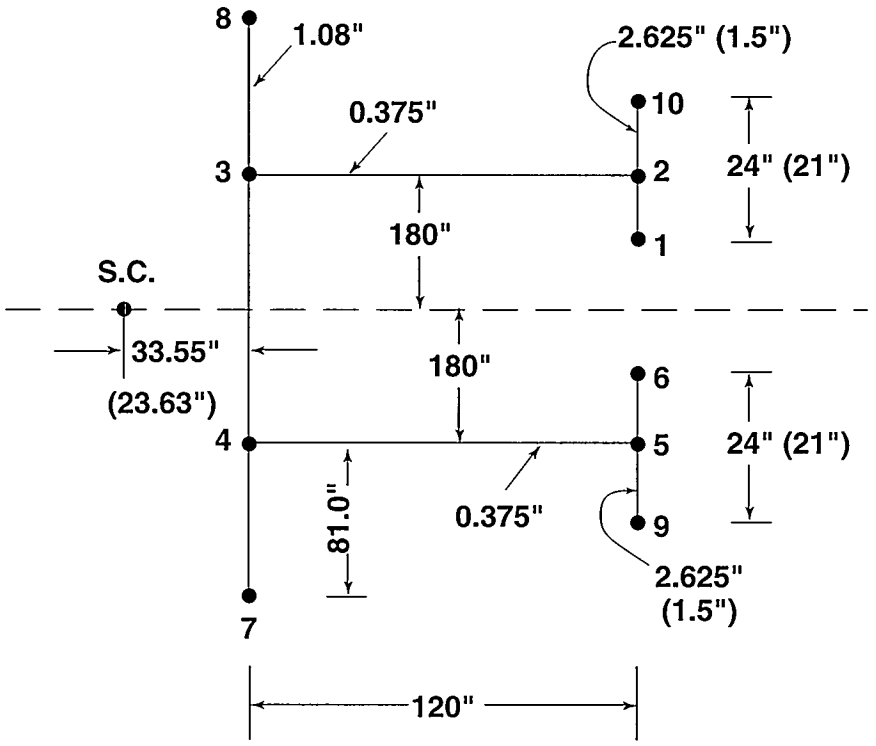

Fig. C-1. Nomenclature for warping constant and statical warping moment calculation.

TABLE C-1

Spreadsheet for Numerical Calculation of the I-40 Bridge Thin-Flange Section Torsional Properties

DETERMINATION OF WARPING CONSTANT AND SECTORIAL MOMENT FOR THIN-FLANGE SECTION										
POINT	RHO ZERO	Lij	RHO*Lij	W ZERO	Tij	Tij Lij	(Wi+Wj)TijLij	Wn	WARPING	STATICAL
1				0				18855.05		
1--2	143.628	10.5	1508.094		1.5	15.75	23752.4805		1.549E+10	570181.7
2				1508.094				17346.96		
2--3	180	120	21600		0.375	45	1107728.46		1.1035E+10	589226.4
3				23108.09				-4253.04		
3--4	-23.628	360	-8506.08		1.08	388.8	14661689.99		7032750185	-7.1E-10
4				14602.01				4253.04		
4--5	180	120	21600		0.375	45	2286181.26		1.1035E+10	-589226
5				36202.01				-17347		
5--6	143.628	10.5	1508.094		1.5	15.75	1164115.922		1.549E+10	-570182
6				37710.11				-18855.1		
7				12688.15				6166.908		
7--4	23.628	81	1913.868		1.08	87.48	2387343.197		7203733924	911537.1
4				14602.01				4253.04		
8				25021.96				-6166.91		
8--3	-23.628	81	-1913.87		1.08	87.48	4210417.299		7203733924	-911537
3				23108.09				-4253.04		
9				34693.92				-15838.9		
9--5	143.628	10.5	1508.094		1.5	15.75	1116610.961		1.3018E+10	-522677
5				36202.01				-17347		
10				3016.188				15838.87		
10--2	-143.628	10.5	-1508.09		1.5	15.75	71257.4415		1.3018E+10	522676.8
2				1508.094				17346.96		
						716.76	27029097.01		1.0053E+11	-1.3E-09
			WARPING CONSTANT=			3.35E+10				
		WARPING STATICAL (SECTORIAL) MOMENT=					-6.6939E-10			

TABLE C-2

Spreadsheet for Numerical Calculation of the I-40 Bridge Thick-Flange Section Torsional Properties

DETERMINATION OF WARPING CONSTANT AND SECTORIAL MOMENT FOR THICK-FLANGE SECTION										
POINT	RHO ZERO	Lij	RHO*Lij	W ZERO	Tij	Tij Lij	(Wi+Wj)TijLij	Wn	WARPING	STATICAL
1				0				17406.96		
1--2	153.53	12	1842.36		2.625	31.5	58034.34		2.571E+10	1038604
2				1842.36				15564.6		
2--3	180	120	21600		0.375	45	1137812.4		8313490777	428814
3				23442.36				-6035.4		
3--4	-33.53	360	-12070.8		1.08	388.8	13535652.1		1.4162E+10	-7.1E-10
4				11371.56				6035.4		
4--5	180	120	21600		0.375	45	1995440.4		8313490777	-428814
5				32971.56				-15564.6		
5--6	153.53	12	1842.36		2.625	31.5	2135242.62		2.571E+10	-1038604
6				34813.92				-17407		
7				8655.63				8751.33		
7--4	33.53	81	2715.93		1.08	87.48	1751978.581		1.4507E+10	1293543
4				11371.56				6035.4		
8				26158.29				-8751.33		
8--3	-33.53	81	-2715.93		1.08	87.48	4339064.862		1.4507E+10	-1293543
3				23442.36				-6035.4		
9				31129.2				-13722.2		
9--5	153.53	12	1842.36		2.625	31.5	2019173.94		2.029E+10	-922535
5				32971.56				-15564.6		
10				3684.72				13722.24		
10--2	-153.53	12	-1842.36		2.625	31.5	174103.02		2.029E+10	922535.5
2				1842.36				15564.6		
						779.76	27146502.26		1.518E+11	-1.4E-09
			WARPING CONSTANT =			5.06E+10				
		WARPING STATICAL (SECTORIAL) MOMENT =					-6.9849E-10			

TABLE C-3

Spreadsheet for Numerical Calculation of the I-40 Bridge Thin-Flange Section (Including Stringers) Torsional Properties

DETERMINATION OF WARPING CONSTANT AND SECTORIAL MOMENT FOR THIN-FLANGE SECTION (STRINGERS INCLUDED)										
POINT	RHO ZERO	Lij	RHO*Lij	W ZERO	Tij	Tij Lij	(Wi+Wj)TijLij	Wn	WARPING	STATICAL
1				0				18876.75		
1--2	143.5	10.5	1506.75		1.5	15.75	23731.3125		1.5529E+10	570886.3
2				1506.75				17370		
2--3	180	120	21600		0.375	45	1107607.5		1.1076E+10	591300
3				23106.75				-4230		
3--11	-23.5	90	-2115		1.08	97.2	4286374.2		3043582290	-616734
11				20991.75				-2115		
11--12	-23.5	90	-2115		1.08	97.2	3875218.2		434797470	-205578
12				18876.75				7.28E-12		
12--13	-23.5	90	-2115		1.08	97.2	3464062.2		434797470	205578
13				16761.75				2115		
13--4	-23.5	90	-2115		1.08	97.2	3052906.2		3043582290	616734
4				14646.75				4230		
4--5	180	120	21600		0.375	45	2290207.5		1.1076E+10	-591300
5				36246.75				-17370		
5--6	143.5	10.5	1506.75		1.5	15.75	1165503.938		1.5529E+10	-570886
6				37753.5				-18876.7		
7				12743.25				6133.5		
7--4	23.5	81	1903.5		1.08	87.48	2396077.2		7125895736	906599
4				14646.75				4230		
8				25010.25				-6133.5		
8--3	-23.5	81	-1903.5		1.08	87.48	4209275.16		7125895736	-906599
3				23106.75				-4230		

TABLE C-3 (Continued)

Spreadsheet for Numerical Calculation of the I-40 Bridge Thin-Flange Section (Including Stringers) Torsional Properties

DETERMINATION OF WARPING CONSTANT AND SECTORIAL MOMENT FOR THIN-FLANGE SECTION (STRINGERS INCLUDED)										
POINT	RHO ZERO	Lij	RHO*Lij	W ZERO	Tij	Tij Lij	(Wi+Wj)TijLij	Wn	WARPING	STATICAL
9				34740				-15863.2		
9--5	143.5	10.5	1506.75		1.5	15.75	1118041.313		1.3055E+10	-523424
5				36246.75				-17370		
10				3013.5				15863.25		
10--2	-143.5	10.5	-1506.75		1.5	15.75	71193.9375		1.3055E+10	523423.7
2				1506.75				17370		
20				19101.75				-225		
20--11	90	21	1890		0.4	8.4	336785.4		41997690	-19656
11				20991.75				-2115		
21				18876.75				7.28E-12		
21--12	0	21	0		0.4	8.4	317129.4		1.3341E-21	1.22E-10
12				18876.75				7.28E-12		
22				18651.75				225		
22--13	-90	21	-1890		0.4	8.4	297473.4		41997690	19656
13				16761.75				2115		
14				19284.2				-407.45		
14--20	-44.5	4.1	-182.45		0.615	2.5215	96790.17293		777420.691	-1594.72
20				19101.75				-225		
15				18919.3				-42.55		
15--20	44.5	4.1	182.45		0.615	2.5215	95870.07758		156356.33	-674.627
20				19101.75				-225		

TABLE C-3 (Continued)

Spreadsheet for Numerical Calculation of the I-40 Bridge Thin-Flange Section (Including Stringers) Torsional Properties

DETERMINATION OF WARPING CONSTANT AND SECTORIAL MOMENT FOR THIN-FLANGE SECTION (STRINGERS INCLUDED)										
POINT	RHO ZERO	Lij	RHO*Lij	W ZERO	Tij	Tij Lij	(Wi+Wj)TijLij	Wn	WARPING	STATICAL
16				19059.2				-182.45		
16--21	-44.5	4.1	-182.45		0.615	2.5215	95655.49793		83935.6983	-460.048
21				18876.75				7.28E-12		
17				18694.3				182.45		
17--21	44.5	4.1	182.45		0.615	2.5215	94735.40258		83935.6983	460.0477
21				18876.75				7.28E-12		
18				18834.2				42.55		
18--22	-44.5	4.1	-182.45		0.615	2.5215	94520.82293		156356.33	674.6273
22				18651.75				225		
19				18469.3				407.45		
19--22	44.5	4.1	182.45		0.615	2.5215	93600.72758		418608.09	1027.385
22				18651.75		757.089	28582759.56		1.0061E+11	-567.337
			WARPING CONSTANT=			3.35E+10				
		WARPING STATICAL (SECTORIAL) MOMENT=					-283.66875			

Distribution

Emin Aktan
University of Cincinnati
Infrastructure Institute
ML71
Cincinnati, OH 45221-0071

David Albright
Alliance for Transportation Research
1001 University Blvd., SE Suite 103
Albuquerque, NM 87106

J. Altes
Institute of Safety Research & Reactor Tech.
Research Center Juelich
5170 Juelich
Postbox 1913, Germany

Alejandro Asfura
EQE, Inc.
44 Montgomery St., Suite 3200
San Francisco, CA 94104

Bill Baker
Los Alamos National Laboratory
ESA-EA, MS P946
P.O. Box 1663
Los Alamos, NM 87545

William Barringer
Alliance for Transportation Research
1001 University Blvd., SE Suite 103
Albuquerque, NM 87106

James Beavers
Martin Marietta Energy Systems, Inc.
P.O. Box Y
Oak Ridge, Tennessee 37831

Mrinmay Biswas
Duke University
Dept. of Civil Engineering
Durham, NC 27706

Larry Blair
Los Alamos National Laboratory
PDET, MS D453
P.O. Box 1663
Los Alamos, NM 87545

Bob Burick
Granite Construction Co.
Heavy Construction Division
Box 50024
Watsonville, CA 95077-5024

Richard Burick
Los Alamos National Laboratory
DDESA, MS P945
P.O. Box 1663
Los Alamos, NM 87545

Steve Chase
Federal Highway Administration
6300 Georgetown Pike
McLean, VA 22101-2296

Franklin Cheng
University of Missouri, Rolla
Dept. of Civil Eng.
Rolla, MO 65401

Ken Chong
National Science Foundation
4201 Wilson Blvd., Rm. 545
Arlington, VA 22230

Tim Darling
Los Alamos National Laboratory
MST-10, MS K764
P.O. Box 1663
Los Alamos, NM 87545

Barry Davidson
Compusoft Engineering LTD.
P.O. Box 9493, Newmarket
Auckland, New Zealand

Thomas Duffey
P.O. Box 1239
Tijeras, NM 87059

Steve Eder
EQE, Inc.
44 Montgomery St., Suite 3200
San Francisco, CA 94104

Richard Fale
W. S. Atkins
160 Aztec West
Park Avenue
Almondsburg,
Bristol U.K. BS124TG

M. Ferner
Anlauf Ingenicur - Consulting GMBH
Posttach 101259
D-69002 Heidelberg,
Germany

Chris Gannon
Penguin Engineering Ltd.
P.O. Box 33093
Pentone, New Zealand

F. Gantenbein
C.E.A.-CE/Saclay - DMT/SEMT/EMS
91191 - GIF - SUR - YVETTE Cedex
France

Nicholas Haritos
Department of Civil and Environment Eng.
Univ. of Melbourne
Parkville Victoria,
Australia 3052

Phil Hashimoto
EQE Engineering, Inc.
Lakeshore Towers
18101 Von Karman Ave., Suite 400
Ivine, CA 92715

George James
Sandia National Laboratories
MS 0557
Albuquerque, NM 87185

J. Johnson
EQE, Inc.
44 Montgomery St., Suite 3200
San Francisco, CA 94104

Robert Kennedy
18971 Villa Terrace
Yorba Linda, CA 92686

Klaus Kerkhoff
Staatliche Materialprufungsanstalt
Universitat Stuttgart
D-70569 Stuttgart (Vailhingen)
Germany

Magdi Khalifa
University of Nebraska Lincoln
Civil Engineering Department
W348 Nebraska Hall
Lincoln, NE 68588-0531

Anne Kiremidjian
Stanford University
Department of Engineering
Terman Engineering Center 238
Stanford, CA 94305-4020

Richard Kohoutek
University of Wollongong
Department of Civil and Mining Engineering
Northfields Avenue
Wollongong 2522,
Australia

Christian Kot
Argonne National Laboratory
9700 South Cass Ave. RE/331
Argonne, IL 60439-4817

Michael Kuhn
Institute of National Surveying and Engineering
University of Technology
Guszhausstr .27-29 (E1272)
A-1040 Vienna, Asustria; Europe

Brett Lewis
APTEK, Inc.
1257 Lake Plaza Dr.
Colorado Springs, CO 80906

Shih-Chi Liu
National Science Foundation
4201 Wilson Blvd.
Arlington, VA 22230

Sami Masri
University of Souther California
Department of Civil Engineering
MC 2531
Los Angeles, CA 90089-2531

Randy Mayes
Sandia National Laboratories
MS0557
PO Box 5800
Albuquerque, NM 87185

Al Migliori
Los Alamos National Laboratory
MST-10, MS K764
P.O. Box 1663
Los Alamos, NM 87545

Jack Moehle
University of California
Department of Civil Engineering
775 Davis Hall
Berkeley, CA 94720

Denby Morrison
Shell E&P Technology Company
Ocean R&D, Bellarie Technology Center
P.O. Box 481
Houston, TX 77001

Peter Moss
Dept. of Civil Eng.
University of Canterbury
Private Bag 4800
Christchurch, New Zealand

Robert Murray
Lawrence Livermore National Laboratory
P.O. Box 808, L-197
Livermore, CA 94550

Roberto Osegueda
The University of Texas at El Paso
Department of Civil Engineering
El Paso, TX 79912

Gerard Pardoen
University of California-Irvine
101 ICEF-Civil Eng.
Irvine, CA 92717

Lee Peterson
Center for Aerospace Structures
University of Colorado, Boulder
Campus Box 429
Boulder, CO 80309-0429

Mick Peterson
Dept. of Mechanical Eng.
Colorado State University
1216 Parkwood Dr.
Fort Collins, CO 80528

Ron Polivka
EQE, Inc.
44 Montgomery St., Suite 3200
San Francisco, CA 94104

Don Rabern
Los Alamos National Laboratory
ESA-EA, MS P946
P.O. Box 1663
Los Alamos, NM 87545

John Reed
Jack Benjamin & Associates
Mountain Bay Plaza
444 Castro St. Suite 501
Mountain View, CA 94041

Jim Ricles
Lehigh University
Department of Civil Engineering
117 ATLSS Drive, H Building
Bethlehem, PA 18015-4729

John Ruminer
Los Alamos National Laboratory
DDESA, MS P945
P.O. Box 1663
Los Alamos, NM 87545

M. Saiidi
College of Engineering
Department of Civil Eng./258
Reno, NV 89557-0152

Mike Salmon
EQE Engineering, Inc.
Lakeshore Towers
18101 Von Karman Ave., Suite 400
Ivine, CA 92715

Paul Smith
Los Alamos National Laboratory
ESA-MT, MS C931
P.O. Box 1663
Los Alamos, NM 87545

Cecily Sobey
Earthquake Engineering Research, Center
Gift & Exchange Dept./University of
1306 Souh 46th Street
Richmond, CA 94804-4698

Mete Sozen
2113 Newmark Civil Engineering Lab.
208 North Romine Street
Urbana, IL 61801

John Stevenson
Stevenson & Associates
9217 Midwest Avenue
Cleveland, Ohio 44125

Norris Stubbs
Texas A&M University
Department of Civil Engineering
Mechanics & Materials Center
College Station, TX 77843-3136

Geoff Tomlinson
Univ. of Sheffield
Dept. of Mechanical Eng.
P.O. Box 600
Mappin St., Sheffield S1 4DU

Ming Wang
University of New Mexico
Department of Civil Engineering
209 Tapy Hall
Albuquerque, NM 87131

Lloyd Welker, Jr.
Ohio Department of Transportation
25 South Front Street
Columbus, Ohio 43216-0899

Ken White
Department of Civil, Agricultural, and Geological
Box 30001/Dept. 3CE
Las Cruces, NM 88003-0001

P. Winney
P&P Engineering
Consultant Engineers
P.O.Box 36
Billingshurst, West Sussex
RH14 OYG

Bill Young
W. P. Young Construction, Inc.
426 Lincoln Centre Drive
Foster City, CA 94404-1127

Dave Zimmerman
University of Houston
Department of Mechanical Engineering
Houston, TX 77204-4792